AIN SHAMS UNIVERSITY

FACULTY OF ENGINEERING

DESIGN AND PRODUCTION ENGINEERING

Investigation of Honeycomb Composite Structure for Wind Turbine Blades with Acoustic Emission Damage Assessment

A Thesis submitted in partial fulfilment of the requirements of the

PhD in Mechanical Engineering

By

Ahmed Hesham Abdulaziz Mohamed Albadr Hashim

M.Sc., Mechanical Engineering, Design and Production Engineering

Ain Shams University, 2016

Supervised by

Prof. Adel M. Elsabbagh

Prof. Karen M. Holford

Dr. Mohammed Hedaya

Cairo –2021

AIN SHAMS UNIVERSITY

FACULTY OF ENGINEERING

Investigation of Honeycomb Composite Structure for Wind Turbine Blades with Acoustics Emissions Damage Assessment

By

Ahmed Hesham Abdulaziz Mohamed Albadr Hashim

M.Sc., Mechanical Engineering, Design and Production Engineering Ain Shams University, 2016

EXAMINATION COMMITTEE

Prof. Mohamed Fahmy Mohamed Shehadeh …….
Dean of Engineering and Technology College, South Valley branch.

Prof. Tamer Mohamed Elnady …….

Professor -Faculty of Engineering-Ain Shams University

Prof. Adel M. Elsabbagh …….

Professor -Faculty of Engineering-Ain Shams University

Prof. Karen M. Holford …….

Professor of Mechanical Engineering - Cardiff University- Britain

Date: …. /……/…….

Statement

This thesis is submitted as a partial fulfillment of Doctor of Philosophy in Mechanical Engineering Engineering, Faculty of Engineering, Ain shams University.

The author carried out the work included in this thesis, and no part of it has been submitted for a degree or a qualification at any other scientific entity.

Student name

Ahmed Hesham Abdulaziz Mohamed

Signature

…….

Date:26 September 2021

Researcher Data

Name	: Ahmed Hesham Abdulaziz Mohamed
Date of birth	: 16th May, 1988
Place of birth	: Cairo
Academic Degree	: MSc in Mechanical Engineering
Field of specialization	: Design and Production Engineering
University issued the degree	: April, 2016
Date of issued degree	: 2016
Current Job	: Teacher Assistant in Design and Production Engineering Department

Dedications

I dedicate this work to

My parents and Family

Prof Ahmed M. Hussein (May Allah be pleased with him)

I believe this work never could be done without the sacrifices made by my wife Sama to keep me moving forward with the work.

Thesis Summary

For optimum aerodynamics in wind turbines, blade materials must have a low weight to bending stiffness ratio. Due to the cost savings compared to using carbon fibre composites alone, aluminium honeycomb will play a critical role in producing longer wind turbine blades with fibre glass as the outer skin in the future.

The thesis includes a study on the glass fibre aluminium honeycomb sandwich structures to be implemented in a wind turbine blade. The study takes staged approach starting by conducting a structural optimisation on the honeycomb sandwich structure to minimise the weight to bending stiffness ratio then studying acoustic emission wave propagation on such complex structure then testing the specimens under bending tests and finally building the whole wind turbine blade with the optimised honeycomb sandwich structure. The acoustic emission wave study is conducted on glass fibre plate then on sandwich specimens of limited honeycomb cells to find out the effects of the cell on the wave propagation from plate to plate and finally on full-scale sandwich panel. It is found that Lamb waves are developed in the glass fibre and the top plate of the honeycomb sandwich structure. In the bottom plate of the honeycomb sandwich structure, it is found that the honeycomb cells act as conduits of AE waves transmission from top to bottom plate. The waveform in the bottom plate is biased to the flexural mode of the Lamb wave with extremely diminished extensional mode.

The A_o mode and S_o mode wave velocities have been studied in directions from 0^o to 90^o with 15^o interval. It is found that A_o velocity does not change with the direction as it depends mainly on the out-of-plane stiffness. On the other hand, the S_o velocities change with direction with respect to the fibre direction. Moreover, the dispersion curves for the wave propagation have been analysed numerically and experimentally

and the insertion loss concept has been proposed in order to quantify the effects of the honeycomb cells on the wave propagation in the skin plates.

The AE source location studies on the sandwich panels are conducted using two famous techniques, the time of arrival method and the Delta-T mapping. The acoustic emission sources are generated on both plates of the sandwich panel while the sensors are solely bonded to one of them.

It is found that Delta-T mapping gives half average error of that of the time of arrival. Further, it is demonstrated the capability of the Delta-T mapping for source location on 2D and 3D.

Thereafter, the bending testing has been conducted on the sandwich specimen coupled with Delta-T Mapping to assess the damage in the specimen and the location. It is found that the acoustic emission testing is not only able to locate the damage on the specimen but also can describe the damage mechanism. The damage progression in the specimen under bending is characterised using both the scanning electron microscope then correlated to the acoustic emission signal frequencies and energy.

Finally, the honeycomb sandwich panel is then used in manufacturing of vertical axis wind turbine blade with aerofoil NACA8412 and the manufacturing considerations are demonstrated.

Acknowledgements

Alhamdolillah, all praises to ALLAH the Almighty for helping me throughout my PhD journey. I would like to express my great appreciation to Prof Karen Holford, Prof Adel Elsabbagh and Dr Mohamed Hedaya for their help and guidance.

I would like to express my gratitude to Dr John McCrory for all he has done with me. He helped me in writing the papers in a very professional way and taught me how to apply the critical thinking in the analysis of the acoustic emission signals. I really appreciate his efforts that helped me to enhance my academic practices.

Further, I would like to extend my thanks to Prof Otto Bernhardi in Karlsruhe University of Applied Sciences, Germany for his constructive suggestions during my work with CalculiX and Salome. Without Dr Matthew Pearson's help in Delta-T analysis, I could have a lot of problems.

I appreciate the help and support from Garry Shipley, Richard, Amanda, Ian and Harry during my testing works in the structural testing workshop. Garry was very generous in giving me his time for helping and technical discussion. Richard always said for humour ''what have I done to deserve all this! '' My friends Frederic Purcell, Yu Wang, Hossem Elnachmie, Stephen Ball, Stephen Griegg, Hayley, Alexander Safar, Carlos Gonzalez, Sam Hurrel, Pim, Alissia, James, Kiki, Anghel Corsecu, Ben Fisher, Paul, Cristina, Berkem Sondors, Emannuel, Matthew Allmark, Mohamed Talaat, Ahmed Barakat, and Weam Elsahar, I do not know words that can describe our lovely friendship that helped me to stay sane, so Diolch, Thank You, Merci, شكرا, Chi Chi, teşekkür, Gracias, Grazie, Mulțumesc, Efcharisto ☺

Really, I believe that nothing would be achieved without the continuous love and support of my wife Dr Sama. She supported me during a lot of hard times and always believes in me.

I would like to acknowledge the support giving to me by the Egyptian Cultural Bureau in London. I would like to appreciate the financial support through Newton-Mosharafa Joint Supervision PhD scholarship from the Egyptian Government and the British Council in UK as well.

Contents

List of Figures

List of Tables

List of Abbreviation

AE: Acoustic Emission.

AELE: Average Euclidean Location Error.

AIC: Akaike Information Criterion.

DTOA: Difference in Time of Arrival.

H-N: Hsu-Nielsen.

FE: Finite Element.

HSP: Honeycomb Sandwich Panel.

GFLP: Glass fibre laminated plate.

PTFE: Poly tetra fluoro ethylene

SHM: Structural Health Monitoring.

SNR: Signal to noise ratio.

SQP: Sequential Quadratic Programming.

2D/3D: Two Dimensions/Three Dimensions.

3PBT : Three-point bending test.

PDT: Peak Definition Time.

HDT: Hit Definition Time.

HLT: Hit Lockout Time.

List of Symbols

A_o: Flexural mode in Lamb Wave.

$\boldsymbol{A}$: Extension stiffness matrix.

$\boldsymbol{A_{dB}}$: AE wave amplitude in decibel.

A*: Amplitude of A_o or S_o in linear curve fitting equation.

$\boldsymbol{B}$: Extension-Bending coupling matrix.

$\boldsymbol{b}$: Breadth of sandwich panel.

$\boldsymbol{c}$: The interception of the trending equation with the Y- axis.

$\boldsymbol{D}$: Bending stiffness matrix.

$\boldsymbol{g}$: Gravity acceleration.

$\boldsymbol{l}$: Length of sandwich panel.

$\boldsymbol{E_1}$: Longitudinal Young's modulus.

$\boldsymbol{E_F}$: Young's modulus of the fibre.

$\boldsymbol{E_M}$: Young's modulus of the matrix.

$\boldsymbol{E_c}$: The honeycomb Young's modulus.

$\boldsymbol{\varepsilon}$: Strain matrix.

$\boldsymbol{k}$: The fibre misalignment factor, it varies from 0.9 to 1.

$\boldsymbol{N}$: Normal forces in the laminates.

$\boldsymbol{M}$: Moment in the laminates.

***M**:** Represents composite moduli, (e.g. E_2, G_{12},.etc).

$\boldsymbol{M_M}$: Represents matrix modulus (e.g. E_M, G_M,.etc).

$\boldsymbol{\alpha}$: Attenuation rate.

ξ: Empirical factor relies on manufacturing process.

η: A non-dimensional factor relies on $\boldsymbol{E_F}$ and $\boldsymbol{E_M}$**.**

$\overline{\boldsymbol{Q_{ij}}}$: Stiffness matrix of off-axis laminae, that is, those whose fibres are at an angle to the global horizontal laminate direction.

$\boldsymbol{\lambda}$: A factor relies on Poisson ratios in longitudinal and transverse directions.

$\boldsymbol{\lambda_c}$: A factor relies on Poisson's ratio of honeycomb material.

$\boldsymbol{W}$*: the weight.*

$\boldsymbol{v_x, v_y}$**:** Poisson's ratios in longitudinal and transverse directions of composite layer.

$\boldsymbol{v_s}$**:** Poisson ratio of honeycomb material.

$\boldsymbol{V_F}$ **:** Volume fraction of the fibre.

$\boldsymbol{V_M}$ **:** Volume fraction of the matrix.

$\boldsymbol{v}$: wave velocity.

$\boldsymbol{V}$**:** AE wave amplitude in volt.

$\boldsymbol{V_{Ref}}$**:** reference amplitude in volt and equals to 0.0001 V.

$\boldsymbol{\rho_{core}}$ **:** Honeycomb density.

$\boldsymbol{\rho_f}$ **:** Top/bottom face material density.

S1 and S2: First and Second AE Sensors.

S_o: Extensional mode in Lamb Wave.

$\boldsymbol{\Delta t_{n,observed}}$**:** Observed time difference.

$\boldsymbol{\Delta t_{n,\ calculated}}$**:** Calculated time difference.

$\boldsymbol{t_1}$: The arrival time at sensor 1.

$\boldsymbol{t_n}$: The arrival time of n^{th} sensor in the array.

$\boldsymbol{t_k}$**:** Laminate thickness

$\boldsymbol{x_n, y_n}$**:** X-Y positions of n^{th} AE sensor.

$\boldsymbol{x_s, y_s}$**:** X-Y positions of AE source.

$\boldsymbol{x_1, y_1}$**:** X-Y positions of first AE sensor.

$\boldsymbol{x}$**:** The distance of the AE source from the receiving sensor.

$\boldsymbol{\overline{z_k}}$ **:** The distance of each lamina in the laminate according to a datum.

Chapter 1: Introduction

Honeycomb Sandwich Panel (HSP) is made by using an adhesive to adhere the face sheets to a honeycomb core. It is commonly used as structural element in wind turbine blade due to its high bending stiffness to weight ratio. The aluminium honeycomb is manufactured by two common methods: the expansion method and the corrugation method. The expansion method entails stacking sheets of aluminium foil of the required thickness in order and applying an adhesive then the honeycomb structure block is formed. The parts that are adhered together form one set of parallel cell walls. Figure 1-1 shows the expansion manufacturing method.

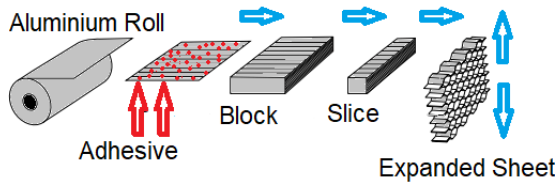

Figure 1- 1. Expansion method of manufacturing the honeycomb, reproduced from [1]

Corrugated sheet is produced by feeding a roll of aluminium foil via a corrugating roller as presented in Figure 1-2. The flat parts of this sheet are coated with adhesive, and sections of corrugated sheets are lined with the flats holding together until the adhesive cures. This is usually used for honeycomb cores that have smaller cell sizes than those generated by expansion process.

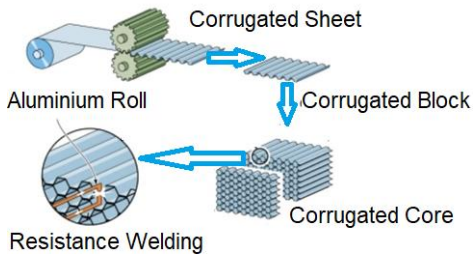

Figure 1- 2. Corrugation method of manufacturing the honeycomb, reference [1]**.**

The honeycomb sandwich panel is a composite structure that consists of a hexagonal cell honeycomb layer sandwiched between two stiff thin plates as shown in Figure 1-3.

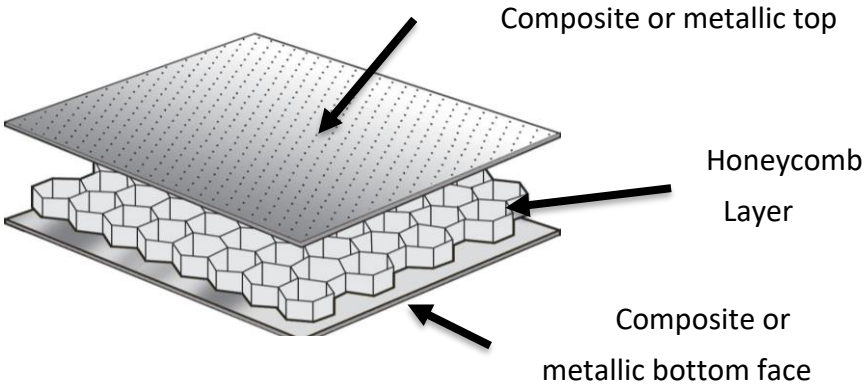

Figure 1- 3. The anatomy of an HSP.

HSP is implemented in wide range of industries such as automotive industry, aerostructures such as wind turbine blades and aircraft wings. It has good mechanical properties such as the high stiffness, light weight, high compressive stiffness and crashworthiness [2], [3]. Figure 1-4 shows the common materials of the wind turbine blades.

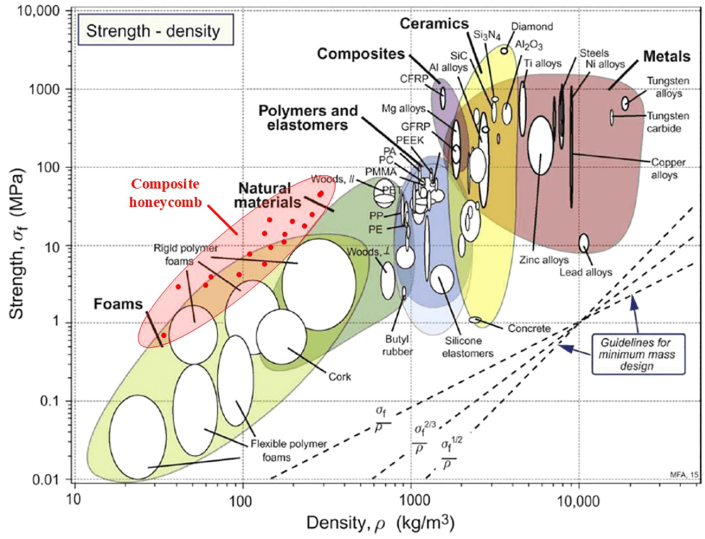

Figure 1- 4. Material chart for wind turbine blades [4]**.**

There are many different cores that can be utilised in the sandwich structures beside the honeycomb core as shown in Figure 1-5.

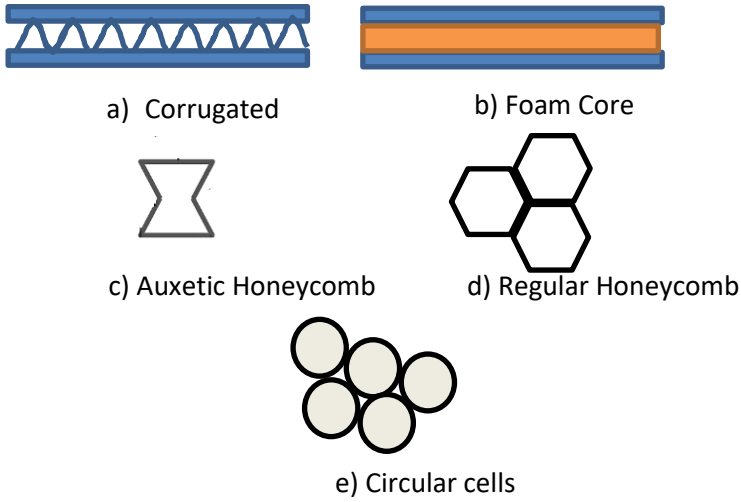

Figure 1- 5. Different core designs for the sandwich structures.

It is worth stating that stiffness and strength of a sandwich structure, mainly rely on core structure [5].

The corrugated core [6] is placed between two thin sheets and it provides high stiffness to weight ratio and stabilizes both sheets through resisting the vertical deformations and the shearing forces as well.

The foam sandwich panel is widely implemented in the wind turbine blades. Foam has demonstrated superior property of lightweight and energy absorption of impact forces [7].

The auxetic honeycomb cell has outstanding mechanical properties compared with the other structures as it has the odd feature of expanding under tension and contracting when compressed [8].

The hexagonal honeycomb is inexpensive and like the previous types, it has high stiffness to weight ratio and excellent crashworthiness properties [9].

The circular core is also available but the main disadvantage of it is the low space efficiency because the cylinders touch each other in points which increase the voids between them. These voids degrade the overall stiffness.

However, it is important to design the suitable dimensions for the panel. HSP may also be damaged by a variety of mechanisms, including top or bottom plate yielding or wrinkling, intra-cell dimpling, matrix cracking local indentation, plate-honeycomb debonding, and core shearing, due to their complex nature [10].

This chapter provides the reader with the literature in the fields of the HSP structural optimisation, overview on the acoustic emission field, acoustic emission wave propagation and source location on the HSP, and the damage assessment using acoustic emission technique for composite structures.

1.1. Honeycomb Optimisation

The issue of HSP optimisation is concerning to obtain an optimised structure that can sustain different loads and boundary conditions.

The physical and mechanical properties of the Honeycomb core materials are greatly impacted by the properties of the materials from which they are made. Several important features of honeycomb cores, on the other hand, are depending on the honeycomb geometry rather than the material properties and should be examined individually as they play a vital role in finding the better structural design [11].

In this regard, Hoa et al. [12], studied the structural optimisation for maximum strength-to-weight ratio for wood-based sandwich composites with paper honeycomb core. The three constraints equations are core buckling, surface indentation and face fracture. Thereafter, they carried

out three-point bending test to investigate the mechanical properties of the optimised structure.

Khan et al. [13], investigated the optimisation of honeycomb sandwich structure weight through the use of Sequential Quadratic Programming and Genetic Algorithm by constraining of specific parameters such as buckling stress, cost and geometry. The design variables are core height, face sheet thickness and cell thickness for an efficient design. They found that the method is robust in finding the optimum variables.

Santos et al. [14], studied the structural optimisation of steel rectangular HSP using the method of moving asymptotes. They wanted to minimise the weight with the failure modes as the constraints. Finally, they carried out finite element analysis to investigate the mechanical properties.

Galehdari et al. [15], have optimised honeycomb structural parameters using SQP and genetic algorithm for minimising the weight to absorbed energy ratio to increase the crashworthiness.

1.2. Acoustic Emission (AE)

1.2.1. Overview

Acoustic Emission (AE) is increasingly recognised as an important non-destructive testing (NDT) method and a valuable technique for structural health monitoring (SHM). “AE is the transient elastic energy that spread in the structure due to the rapid change in the material under test or operational forces” [16]. It is considered as a passive technique because there is no input inspection signal, just sensing the energy release within material [16], [17]. Figure 1-6 shows the AE test setup.

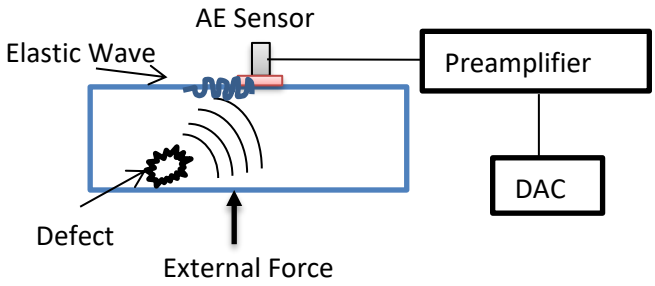

Figure 1- 6. AE source detection system.

The basic principles of AE testing are as following [18];

The structure is either in operation or under test load. The initiation of a defect releases elastic energy. Elastic energy induces a structural perturbation, which causes an elastic wave to propagate from the source to the AE sensor with a piezoelectric element.

The sequence of the AE testing starts as the mechanical perturbation is converted into a voltage difference by AE sensor then obtaining measurement data and plotting the AE signal and finally performing analysis and assessment of data. The AE frequency range of the signal is between 1 kHz to 1 MHz as presented in Figure 1-7 .

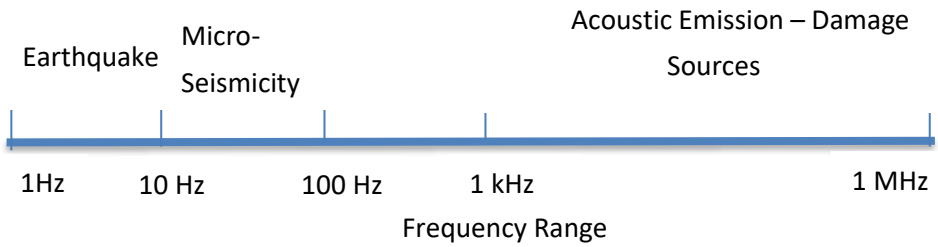

Figure 1- 7. Frequency Range for AE sources.

The AE is proven to be a reliable and useful technique for different areas of application. Material characterisation is a very common area of application for the AE where the defect detection, growth and localisation can be identified and investigated.

The AE technique can be used for structural health monitoring (SHM) such as wind turbines, railways, bridges, aircrafts, pipe leakage, pressure vessel testing, and machinery. Moreover, recently, AE has invaded new different fields such as medical and dental fields [19], [20].

Although vibration based SHM technique is implemented by many researchers for detecting the damage in wind turbine blades, AE based SHM overcomes a lot of technical limitations which are encountered by the vibration-based techniques. As examples, vibration techniques need the blade under operation, healthy vibration signal signature pattern to be a reference for the measured signal, and some information about the modal characteristics of the blade. Further, if the frequency change is greater than 5% can the damage in a structure be clearly measured. However, excitation of a high frequency from a structure is problematic since such vibration would necessitate higher energy, which is practically impossible [21].

Moreover, the vibration-based techniques are limited to defects like gear fault, rolling bearing fault, journal bearing fault, etc., in the wind turbine. In contrast, the AE based SHM on wind turbine is not only capable for finding the previous defects but also the blade internal defects such as delamination, fibre breakage, matrix cracking, and fibre pull out. Additionally, AE technique can localise the defect and hence, helping the maintenance engineers to fix it before catastrophic failure.

Most of AE sources exhibit a comparable waveform feature. The waveform is either continuous signal or burst (e.g. pulse or abrupt) as shown in Figure 1-8. Continuous signal appears as result of friction between pair, fluid pipe leakage and machine noise. Burst signal appears as a result of sudden emission source such as sudden delamination in the composites.

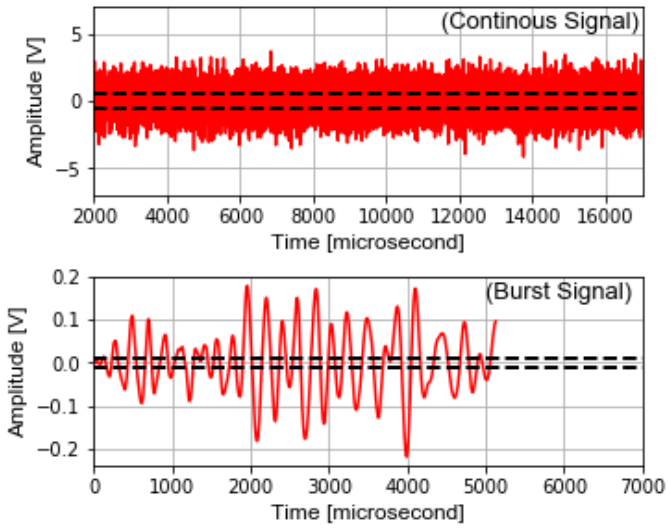

Figure 1- 8. AE typical continuous and burst signals.

Figure 1-9 presents the main features of the burst AE signal. Usually, AE features refer to amplitude, duration, rise time, decay and counts. Annex A provides the explanation of the basic features of a typical AE burst signal.

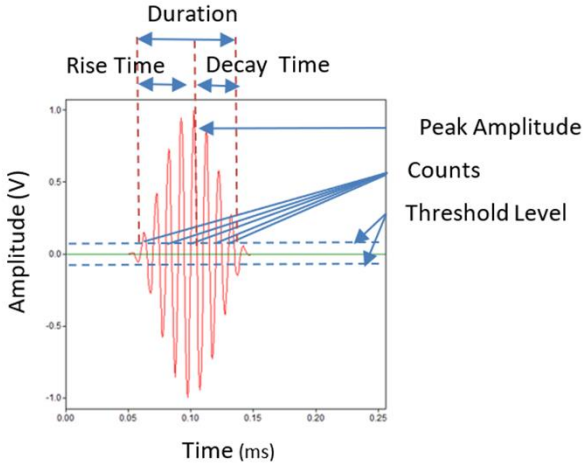

Figure 1- 9. Typical AE waveform features.

1.2.1.1 Time of Arrival

On the other hand, a major concern for reliable AE signal detection is pinpointing the time of arrival (TOA) of the signal accurately. Without accurate determination of TOA, the signal could be interpreted incorrectly and hence, obtaining misleading information. The TOA is commonly detected by using threshold crossing methods whether fixed or float. In the threshold crossing methods, the signal's TOA is detected when the amplitude exceeds the predefined threshold level. However, the threshold crossing is prone to greater error level [22] because;

- If the threshold level is too large, then the wrong peaks would be detected, and hence incorrect TOA is pinpointed.
- If the threshold level is too small, then the noise peaks would be detected, and hence incorrect TOA is pinpointed.
- Skill and correct understanding of the material under test are required to predefine suitable threshold level.

Figure 1-10 presents the different cases of the threshold crossings.

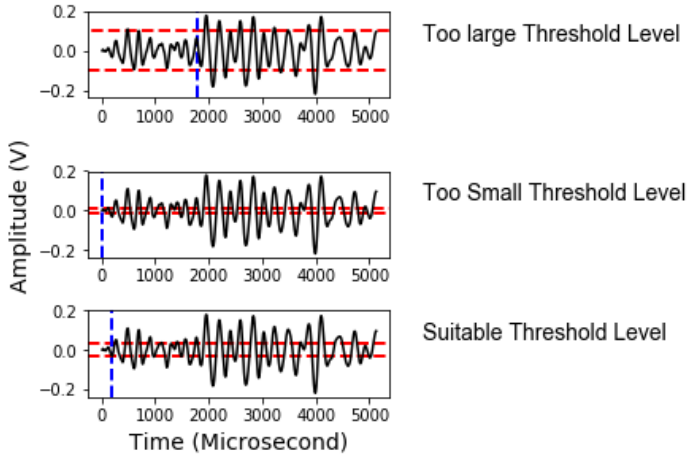

Figure 1- 10. Threshold level different cases.

To avoid manual interpretation, handpicking, or utilising a threshold crossing method, all of which can be prone to errors [22], the Akaike

Information Criterion (AIC) [23] method can be used to determine an accurate first TOA of AE signal [19], [20]. The AIC [21] compares the similarity between signal parts before and after point (*n*) until it reaches the minimum similarity value and hence the signal onset is effectively determined. Eq. (1.1) shows the AIC function.

$$AIC(n) = n\ log(var(y(1:n))) + (n_{sample} - n\ - 1)\ log(var\ (y\ (n+1:\ n_{sample}))) \qquad (1.1)$$

where; *y(1, n)* for data points starting from 1 to n and *y (n+1: n_{sample})* for data points n + 1 to n_{sample} are the two segments in the selected time window, and *(var)* stands for the statistical variance of the data.

Figure 1- 11 shows an example of the application of AIC function in red line and the blue dashed line represents the minimum similarity point. The orange dashed vertical line represents the signal's TOA picking by the commonly used threshold crossing method. It can be seen clearly the lack of sensitivity for TOA detection by the threshold crossing method. The minimum similarity point represents the TOA of the AE signal. Another similar way is the Bayseian Information Criterion (BIC) which can be used for TOA determination [24]. However, in this study, AIC is considered.

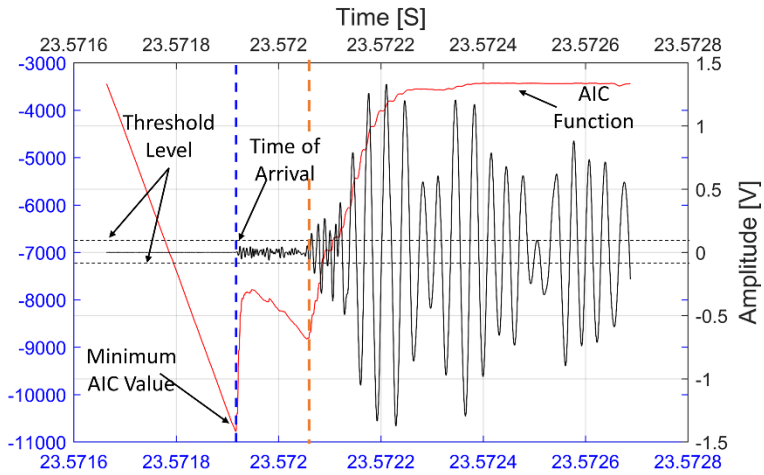

Figure 1- 11. AIC function on a burst AE signal.

Another consideration to identify correct TOA of a signal, is the selection of timing parameters, namely the Hit Definition Time (HDT), Peak Definition Time (PDT), and Hit Lockout Time (HLT) [27].

The HDT specifies the amount of time the acquisition system will wait to determine when a hit has ended. Too small HDT can cause a single signal to be recorded as multiple ones. Too large HDT can cause the detection of the signals and reflections treating them as one combined.

The PDT parameter represents the permissible time, after a signal is detected, to identify the peak value. If the PDT is too large, then false measurements of peak value are more probably to happen. If the PDT is too small, then the true peak may not be identified. The HLT parameter represents the needed time for which a hit is detected before a new hit can be detected. If HLT is too large, then the system may not record the coming AE signal and if it is put too small then the system may record reflections and late arriving component of the AE as hits causing incorrect interpretation of the information. Figure 1-12 demonstrates the timing parameters on the burst signal.

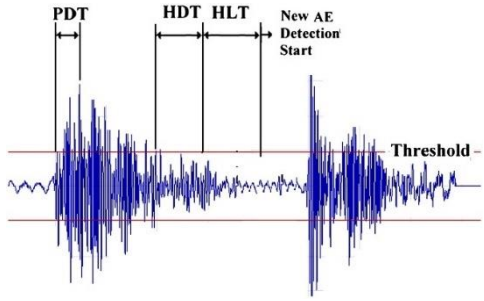

Figure 1- 12. Timing parameters on a burst AE signal, reference [28]**.**

1.2.1.2 AE Sensors

Since AE is associated with the elastic surface waves, usually the AE sensor is a piezoelectric type. Figure 1-13 presents a schematic drawing of a typical AE sensor. A typical AE sensor consists of a piezoelectric element with an electrode on each face. One electrode is grounded and

the other one is the electrical charge lead plate. On the top of the piezoelectric element, a damping material added to minimise the reflections and to limit the duration of vibration.

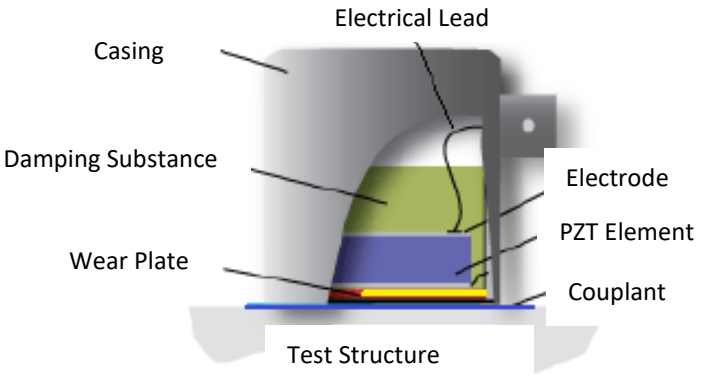

Figure 1- 13. A typical AE sensor, reproduced from source [29]**.**

However, it is worth mentioning that there are fibre optic AE sensors and MEMS-capacitive type. Table 1-1 presents a comparison between different types of the AE sensors.

Table 1- 1. Different types of the AE sensors.

AE Sensor	Advantages	Disadvantages
Piezoelectric	Robustness and sensitive	n/a
Fibre Optic	Long measurements	Unreliable at high frequency
MEMS-Capacitive	Variable design capabilities-high temperature applications	Low signal to noise ratio

Importantly, care must be taken while mounting the sensors because incorrect mounting yields wrong data. Therefore, the sensor must be correctly restrained to the surface using a clamping method if needed and the sensor must be acoustically coupled to the surface [30]. Table 1-2 presents different types of the sensor mounting methods with more emphasis on the area of usage.

Table 1- 2. Different types of the fixation of AE sensors.

Fixation Method	Schematic Representation	Description and Usage
Direct on specimen		• Use silicone or grease to fix sensor. • Put a mass over it until curing. • Widely used on tension specimens.
Aluminium hat method	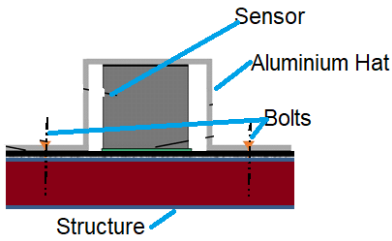	• Mounting pressure comes from bolts. • Used on concrete structures.
Two opposite magnets	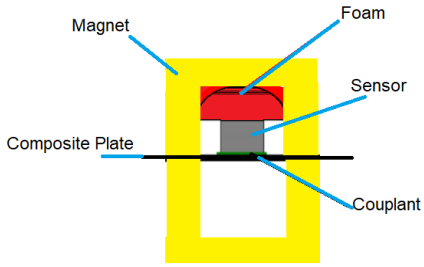	• Mounting pressure comes from opposite magnets. • Used on thin composite plates.
Clamp with spring	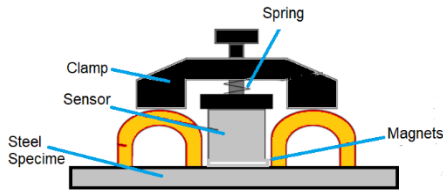	• Mounting pressure comes from compression spring. • Used on ferromagnetic specimens.
Cable and tab	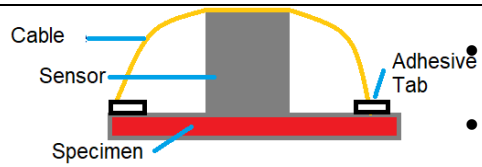	• Mounting pressure is from tension in cable. • Used on vessels.

1.2.2. Acoustical Wave in solids

There are two categories of AE waves in the materials. Mainly, the bulk waves and surface/ plate waves. The bulk waves, include longitudinal or pressure P-waves and shear S-waves. They arise in the material's internal structure as results of phase differences in case of concrete structures and dislocations. The surface and plate waves include Rayleigh, Love and Lamb wave.

It is worth mentioning that Internal P-waves, for example, can generate Rayleigh waves when they reach the material's surface. This is the difficulty of the AE application since one must be skilful and aware of different natures of the AE waves. Figure 1-14 presents different types of the waves.

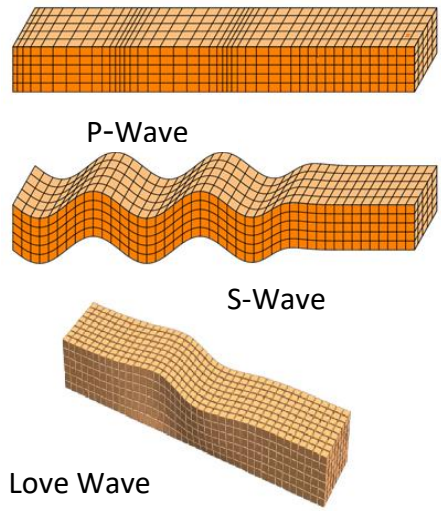

Figure 1- 14. AE waves on different structures.

In the next sections, the surface and plate waves will be elaborated on; because much of an wind turbine blade's skin is made up of thin panels and hence particularly relevant to this thesis.

1.2.2.1 Lamb Wave

In thin plates, usually Lamb wave is the dominant wave in the structure [31]. It consists of two basic modes, extensional (symmetric) and flexural (asymmetric) (i.e. A_o and S_o) [32]as shown in Figure 1-15.

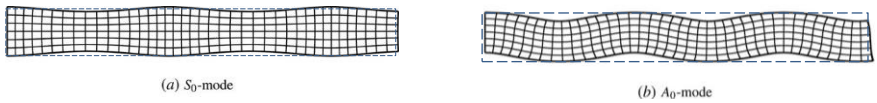

Figure 1- 15. Basic modes of Lamb wave (a) S_o and (b) A_o

Lamb's equations can be found in [32]. They show the existence of two families of sinusoidal wave modes in the thin plates. The physical boundary condition for the free surfaces of the plate.

Another unique characteristics of Lamb waves are the phase and group velocities. Phase velocity is the velocity of specific wave mode in the wave packet propagation whereas the group velocity is the rate at which the overall envelope shape of the wave's amplitudes propagates over space. Figure 1-16 presents the group and phase velocities.

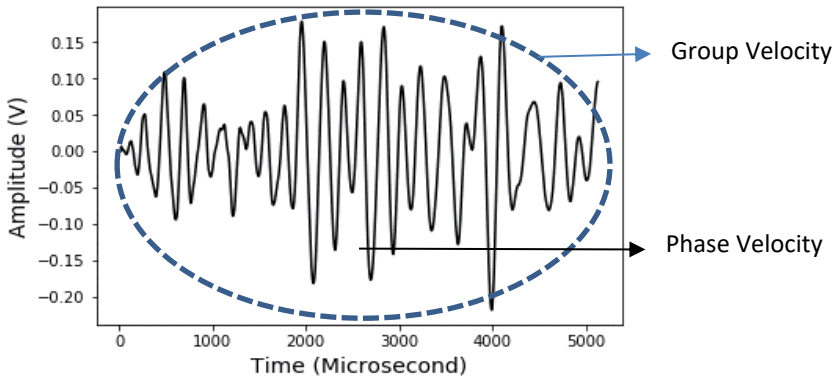

Figure 1- 16. Group and phase velocities.

A dispersion curve can be used to describe the relationship between frequency and velocity of the S_o and A_o Lamb wave modes, as shown in Figure 1-17.

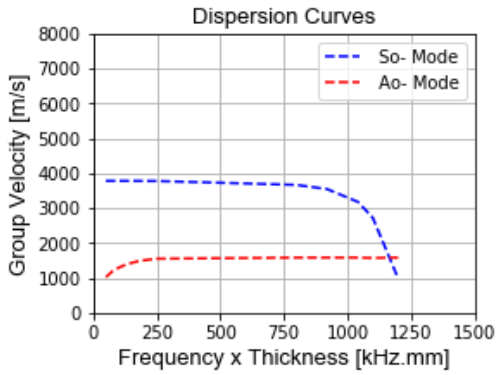

Figure 1- 17. Example of dispersion curves of A_o and S_o modes

1.2.2.2 Rayleigh Wave

The Rayleigh waves are found in the plates of one dimension that is much larger than the wavelength. Sometimes these waves are called as " bulk waves". The wave consists of two distinguished modes longitudinal (i.e. compression / pressure or P-wave) and transverse (i.e. shear or S-wave).

The solution of the characteristic wave equation shows that there is only one positive real root. It is important to note that the characteristic equation does not include a frequency component. Therefore, the Rayleigh wave is not dispersive (i.e. velocity is independent on frequency). Therefore, there is no dispersion curves for such wave.

1.2.3. Standard AE Testing

Correct sensor mounting is critical to the success of AE as a technique, as stated in section 1.2.1. Hsu-Neilson (H-N) approach is developed to generate an AE source by breaking the lead of a mechanical pencil at 30^o to the inspected surface [18], [33]. The free length of lead at tip is 3 mm (±0.5 mm) and the lead diameter is 0.5 mm. As the lead is pressed against the surface of the specimen causing strain concentration in itself, at the breakage moment, the lead's accumulated stress is released, resulting in a quick displacement of the surface and, as a result, the emission of an

acoustic wave. Figure 1-18 demonstrates a schematic drawing for the H-N source generation.

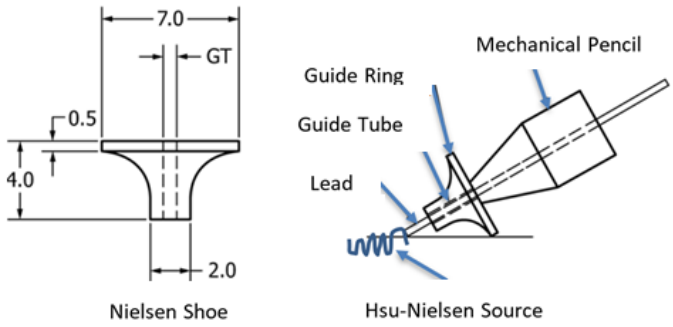

Figure 1- 18. : Generation of an H-N source, reproduced from [18]**.**

1.2.4. Acoustic Emission in HSP

As a result, as the plate structure becomes more complex, the elastic wave nature changes or distorts. The propagation of AE waves in honeycomb sandwich panel (HSP) has been studied before, but much less frequently than in other composite structures.

The emphasis of recent publications has been on determining and defining damage mechanisms in glass fibre composite structures[31], [34] while Hafizi et al. [35] investigated AE signal energy attenuation using Hsu-Nielsen (H-N) sources in a 400 x 400 x 2.9 mms glass fibre reinforced epoxy plate produced by hand layup method and staking order of $[0^o]_4$ laminates in directions 0^o, 45^o, 60^o, and 90^o with respect to the fibre direction. They found out that Lamb waves were developed in the plate and propagated at 30 kHz and 100 kHz for A_o and S_o, respectively.

Wu et al. [36], used the plate wave theory and Hsu-Nielsen (H-N) sources to investigate AE wave velocity in honeycomb sandwich structures with woven glass fibre plates numerically and experimentally. However, they concentrated only on the acoustic wave's arrival time, which is used to calculate the extensional mode's velocity, rather than

decomposing the signal into its two indicative modes (i.e. flexural and extensional modes).

Sikdar et al. [37], investigated AE wave propagation analytically and experimentally for the purpose of AE source positioning using a sandwich structure consisting of aramid honeycomb with two aluminium skins and applying the particle swarm optimisation strategy.

Baid et al. [38], investigated the dispersion properties of Lamb waves in a sandwich structure made up of a 12.7 mm standard aluminium honeycomb sandwiched between two woven carbon fibre plates.

They determined the dispersion curves using a global matrix method and experimentally tested their solutions with a pair of piezoelectric transducers (PZT) on the top plate. The flexural Ao mode velocities were the only ones that were studied.

Guo et al. [39], used a multilayer model to investigate Lamb wave characteristics in an aluminium honeycomb structure and discovered that the phase and group velocity in the Lamb wave dispersion curves are less influenced by the core properties at low frequencies, while attenuation increases at higher frequencies.

Despite its usefulness, none of the studies examined gave much thought to how AE propagates across the thickness of the sandwich panel, which is something that this study aims to discuss.

1.3. Acoustic Emission Source Location

1.3.1. Difference in Time of Arrival Method

Difference of time of arrival (DOTA) approach is widely used by different researchers and employed by AEwin® software which is one of the most popular and commercial AE system [40], [41]. In this technique, the triangulation method and the DTOAs of the AE signals are used to

determine the AE source location. Figure 1-19 presents the AE source location using DTOA and triangulation method.

Briefly, this method relies on the minimisation of objective function (X^2) presented by Eq. (1.2).

$$X^2 = \sum(\Delta t_{n,observed} - \Delta t_{n,calculated})^2 \quad (1.2)$$

where;

$\Delta t_{n,observed} = t_n - t_1$

$\Delta t_{n,\ calculated} = \sqrt{(x_n - x_s)^2 - (y_n - y_s)^2} - \sqrt{(x_1 - x_s)^2 - (y_1 - y_s)^2}/v$

t_1 is the arrival time at sensor 1,

t_n is the arrival time of n^{th} sensor in the array,

v is wave velocity,

x_n, y_n: X-Y positions of n^{th} sensor

x_s, y_s: X-Y positions of AE source

x_1, y_1: X-Y positions of first sensor

The DTOA source location considers that the wave path is constant, the wave velocity is the same everywhere on the structure and the structure thickness is uniform. These simplifying assumptions affect the accuracy of this method in irregular structures and composite materials where the fibre direction contributes to the wave propagation significantly. A detailed explanation of this method is in [42].

However, there are many limitations for of DTOA-based methods. Mainly, ignoring the effects of the anisotropic characteristics of the composite materials by assuming the material is homogeneous and the wave path is the same in all directions [43]. Therefore, the accuracy of location measurement on HSP using DTOA-based method becomes questionable [44]. In this thesis, the DTOA method is investigated for being used on the HSP.

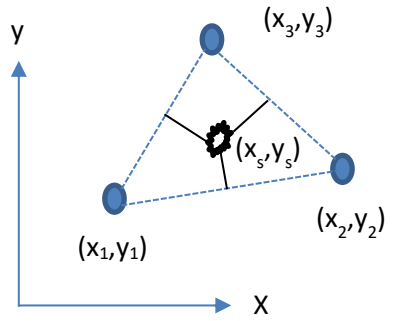

Figure 1- 19. AE source location using DTOA.

1.3.2. Delta T- Mapping

In order to avoid the assumptions of the DTOA method, a special technique called "Delta-T-Mapping" has been developed originally in Cardiff University [45]–[47]. This technique does not require any sort of information about the wave propagation path and wave propagation velocity. Briefly, this technique starts by obtaining training time data for a 2D grid followed by computing the difference in times of arrivals between each pair of sensors and hence constructing time maps. These maps are used to compare actual AE events data and locate them.

Delta-T Mapping instead relies on obtaining training data from the structure itself, using a 2D grid, and computing the DTOAs between each pair of sensors, hence constructing time maps between each pair of sensors. The arrival times of AE sources recorded from the structure can then be compared against these maps in order to calculate the source location. Delta-T Mapping is implemented by conducting the following steps:

- Specifying the area of interest that satisfies the requirement that the signals can be detected before being attenuated greatly.
- Drawing the grid system on the HSP with a resolution higher than that of the signal wavelength.

- Generating H-N sources at each node, five times for averaging.
- Computing the DTOA for each pair of sensors and hence Delta-T maps can be constructed.

The Delta-T Mapping is usually used upon the thin simple composite or metallic plates [40]. It has not been on the complex HSPs. Furthermore, it is usually used on 2D surfaces only.

Since the capability of Delta-T Mapping to locate defects in complex HSP structure has not yet been investigated. This will be investigated critically in this thesis to determine the capability of the Delta-T Mapping for being implemented on such surfaces.

1.4. Defect Location in HSP

Sikdar et al. [37], developed an algorithm for AE defect localisation on HSP consisting of carbon fibre plates with aluminium honeycomb. On the top plate, they bonded eight AE sensors with different configurations to localise three artificial defects. They investigated circular, rectangular and zigzag sensor arrays. The lowest error in defect location was 15 mm resulting from the zigzag configuration.

Leone et al. [48], investigated using AE for detecting damage initiation and progression in carbon fibre plates with honeycomb structure. They identified the damage location using the DTOA method.

The literature shows that the common way for AE source location is the DTOA-based methods.

1.5. Acoustic Emission Damage Assessment

Since the AE technique is so sensitive, recent research in non-destructive testing of composite sandwich panels has focused on using it to both detect and locate damage progression in sandwich structures under loading [17], [49]. The AE sources in the composite materials

include fibre pull out, fibre breakage, matrix cracking, delamination, and debonding between fibre and matrix [50].

Harizi et al. [51], studied the mechanical behaviour of carbon fibre reinforced thermoplastic sandwich composites with various core materials (i.e. Nomex, Polyetherimide, and aluminium) in three-point bending experiments using AE monitoring to determine the damage mechanism. The total absolute energy of the perceived AE hits was used to calculate the different specimens. They also used strain gauges to classify the failure modes using the AE amplitudes of the events in these regions. They concluded that the accumulated absolute energy has the potential to correlate damage evolution with AE perceived hits.

Pashmforoush et al. [52], used acoustic emission technique to classify the various harm types during a three-point bending test on glass fibre epoxy composite. They used clustering analysis to determine the harm mode based on frequency content. Matrix cracking with a frequency range of 90-195 kHz, fibre-matrix debonding with a frequency range of 210-335 kHz, and fibre rupture with a frequency range of 360-450 kHz were discovered to be the key harm mechanisms.

Panek et al. [53], conducted static four-point bending experiments on three different glass fibre-epoxy composite configurations (quasi-unidirectional $[0°]_n$, cross-ply $[90°,0°]_n$, and angle-ply $[45°]_n$, for example). They looked at the relationship between the AE harm mechanism and the peak frequencies and rise time peak amplitude ratio in these specimens. They discovered that fibre-matrix debonding had frequencies that were centred in the middle.

In a three-point bending test, Beheshtizadeh et al. [54], investigated the failure modes of glass fibre reinforced epoxy. They discovered that matrix cracking, debonding, and fibre breakage were the most common failure modes in this composite, and they then determined the frequency

ranges associated with each failure mode. The matrix cracking frequency range is 62.5 to 125 kHz, the fibre-matrix debonding frequency range is 125 to 187.5 kHz, and the fibre breakage frequency range is 187.5 to 250 kHz.

Under bending test, Kumar et al. [55], characterised the damage modes in glass fibre epoxy composites with layup series $[0^{o}/90^{o}/90^{o}/0^{o}]_{3s}$. They connected the harm mode to the frequency band by using cumulative AE counts, counts rate, and frequency spectrum. Matrix cracking appeared in the frequency band (70-150 kHz), fibre-matrix debonding in the frequency band (210-270 kHz), and fibre failure in the frequency band (70-150 kHz).

In this study, the frequency and cumulative energy analyses are considered in the damage assessment work.

1.6. Problem Statement

Several engineering applications require high stiffness to weight ratio materials. Since honeycomb composite structures have outstanding mechanical properties that have made them of high importance in wind turbine blade designs. The cellular structure of the honeycomb can be tuned to achieve optimum mechanical properties especially the stiffness and weight. Therefore, it is important to propose a honeycomb composite material design, testing and validation methodology to be utilised in wind turbine blades.

Despite its importance as a real-world monitoring consideration, across all literature studied, none quantified the propagation behaviour of AE through the thickness of the sandwich panel, from one surface to the other. Propagation of this nature would be present if AE transducers are affixed to the inside skin of an aerofoil HSP structure, such as a wind turbine blade, yet damage could occur on the outer skin.

Figure 1-20 shows example of aerostructure where the AE sensors are mounted from inside as it is impractical to mount the sensors on the outer skin. That is why, it is important to understand the AE propagation in the complex sandwich structures on the plate scale and through the honeycomb cell scale.

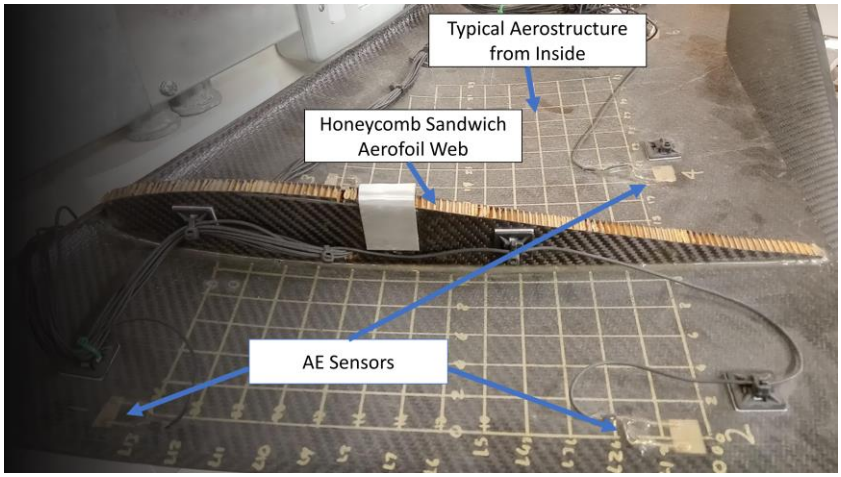

Figure 1- 20. AE sensors inside an aerostructure reproduced from [56]**.**

1.7. Aims and Objectives

This thesis aims instead to improve the honeycomb selection methodology and testing, defect localisation techniques and analysis methods required for the implementation of Acoustics Emissions in studying the defects in honeycomb sandwich structures which few works have dealt with. Emphasis is given to the honeycomb sandwich structure optimisation, elastic wave propagation and defects localisations techniques for such complex structures.

The key objectives of this study are:

- Proposing a honeycomb composite structure optimisation platform to increase the bending stiffness to weight ratio.
- Presenting a numerical study of the optimised honeycomb composite structure by using open-source finite element coding.

- Studying the elastic wave propagation in glass fibre plate. This provides a comprehensive study on wave nature, modes, velocities, wavelet transformations and attenuations.
- Studying the elastic wave propagation on limited number of cells between two glass fibre plates. This is to understand the effect of the unit cell on the elastic wave propagation in the glass fibre plates.
- Studying the elastic wave propagation in HSP structures. This provides a comprehensive study on wave nature, modes, velocities, wavelet transformations and attenuations.
- Analysing the effects of honeycomb sandwich structure on elastic wave propagation in the fibre glass plates and proposing a suitable measure for such effects.
- Investigation of the ability of AE to localise artificial AE sources on HSP structures;
    - Using DTOA method.
    - Using Delta-T Mapping method.
- Design automatic algorithm using MATLAB for AE wave characterisation (i.e. wave modes, amplitudes, frequencies and velocities).
- Coupon testing of honeycomb composite structure under three-point bending with acoustic emission monitoring for assessing the damage.
- Damage assessment in the HSP after the three-point bending test using;
    - AE Frequency Analysis.
    - AE Cumulative Energy Analysis.
    - Scanning Electron Microscope.

1.8. Novelty Statement

Some of the work contained in this thesis has been published through three journal papers and two specialised-international conference papers.

- Ahmed H Abdulaziz, John McCrory, Karen Holford, Mohamed Hedaya, Adel Elsabbagh, ***''Effects of Honeycomb Core on Acoustic Emission Wave Propagation in Glass Fibre Composite Plates''***, Proceedings of 58th Annual Conference of British Institute of Non-Destructive Testing, Telford, UK, (September 2019).
- Ahmed H Abdulaziz, Mohamed Hedaya, John McCrory, Karen Holford, Adel Elsabbagh, ***''Parametric Study of Honeycomb Composite Structure Using Open Source Finite Element Software''***, Proceedings of 27th UK Association of Computational Mechanics, London, (April 2019).
- Ahmed H Abdulaziz, Mohamed Hedaya, Adel Elsabbagh, Karen Holford, John McCrory, "***Acoustic Emission Source Location in Composite-Honeycomb Sandwich Structures***", International Journal of Renewable Energy Research, vol.(11), No.(2),pp. 851-860, (June 2021).
- Ahmed H Abdulaziz, Mohamed Hedaya, Adel Elsabbagh, Karen Holford, John McCrory, "***Acoustic Emission Wave Propagation in Glass Fibre Aluminium Honeycomb Sandwich Structures***", Journal of Composite Structures, vol. (277), (December 2021).
- Ahmed H Abdulaziz, John McCrory, Karen Holford, Adel Elsabbagh, Mohamed Hedaya," ***Experimental Three-Point Bending Test of Glass Fibre Aluminium Honeycomb Sandwich Panel with Acoustic Emission Damage Assessment***", Accepted, Journal Insight of British Institute of Non-destructive Testing.

1.9. Thesis Organisation

The thesis consists of seven chapters as follow:

- **Chapter 1:** presents overview of the thesis and a critical literature review on the structural optimisation , AE wave propagation and defect localisation techniques and, problem and novelty statements.
- **Chapter 2:** presents the modelling of honeycomb composite structure using sequential quadratic programming and open-source FE code.
- **Chapter 3:** presents the specimen manufacturing, ultrasonic testing, and AE wave propagation characteristics in honeycomb composite structures.
- **Chapter 4:** presents a study on the AE localisation techniques to find out the most proper defect localisation strategy to be implemented during the coupon mechanical testing.
- **Chapter 5:** presents the coupon bending testing of the optimised honeycomb composite structure with AE monitoring and damage assessment.
- **Chapter 6:** presents the vertical axis wind turbine manufacturing
- **Chapter 7:** presents the conclusions and future work.

Figure 1-21 shows a block diagram that is summerising the research methodology.

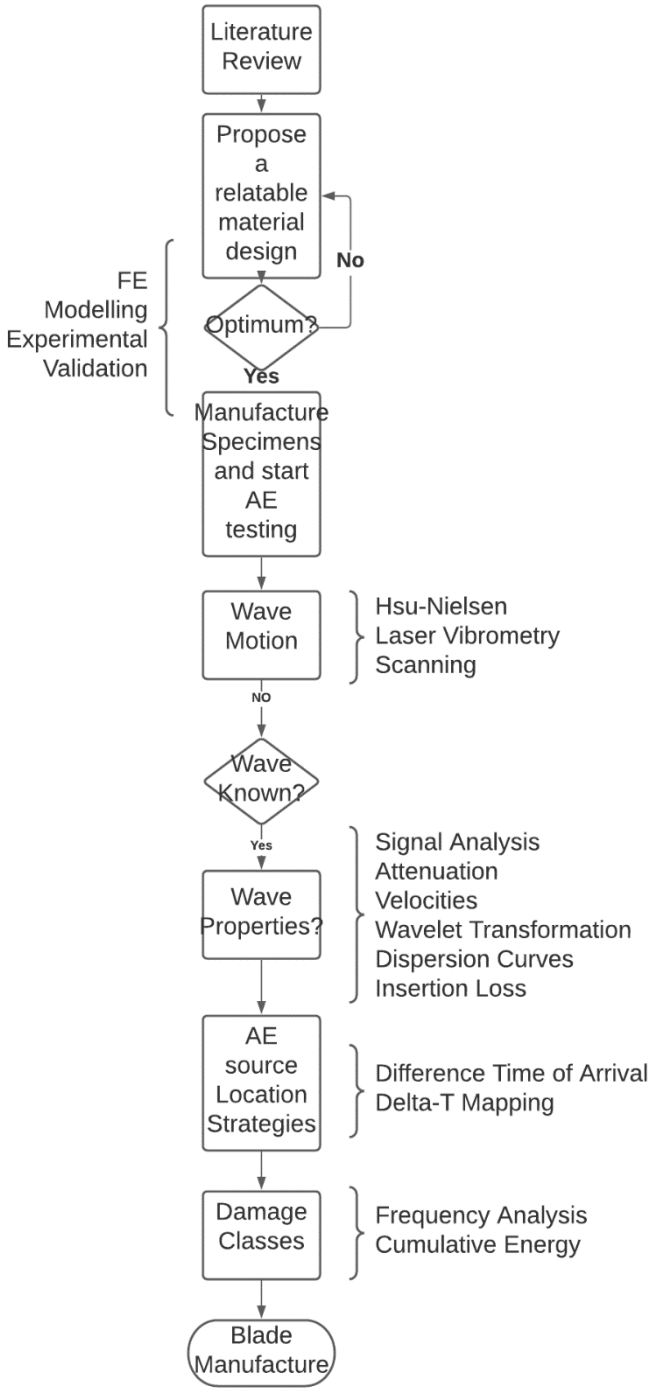

Figure 1- 21. Thesis work flowchart.

Chapter 2: HSP Structural Modelling

2.1. Introduction

In this chapter, the structural optimisation for minimum weight to bending stiffness ratio and the numerical/experimental verification are presented. This is a pre-testing in order to get insight into the material before manufacturing it. The panel consists of aluminium honeycomb sandwiched between two orthotropic fibre glass plates. The fibre glass composite with aluminium honeycomb is usually implemented in the manufacturing of wind turbine blades because of the following advantages:

- High strength/stiffness to weight ratio.
- Can tailor strength/stiffness in load direction.
- Less corrosion.
- Lower weight compared to alloys.
- Inherent damping to vibrations.

2.2. Glass Fibre Laminated Plate Design

Due to their excellent material properties, glass fibre reinforced polymers are extremely useful for the applications that require low weight with high in-plane and out-of-plane stiffness [57]. Matrix selection is a critical parameter since it functions as a shield against harsh conditions and protects the fibre surface from mechanical and chemical effects. It also aids in spreading the load acting on the composite uniformly through all of the fibre reinforced in it [58]. Epoxy resin is used as a matrix for the glass fibre reinforcements. It is worth mentioning that the fibre glass is inexpensive reinforcement and widely implemented in the wind turbine blades [59], [60]. Therefore, in this study the fibre glass reinforcement is considered.

2.2.1. Halpin-Tsai Approach

The Halpin–Tsai model is a mathematical model that considers the geometry and orientation of the fibre, as well as the elastic properties of the fibre and matrix, to predict the elasticity of composite material [61]. Eq. (2.1) presents the calculation of the longitudinal Young's modulus.

$$E_1 = k(V_F E_F + V_M E_M) \tag{2.1}$$

where;

E_1: Longitudinal Young's modulus.

k : is the fibre misalignment factor, it varies from 0.9 to 1.

E_F: Young's modulus of the fibre.

E_M: Young's modulus of the matrix.

V_F : Volume fraction of the fibre.

V_M : Volume fraction of the matrix.

Eq. (2.2) is the equation used for determination of transverse and normal Young's moduli, and shear moduli in different directions.

$$\frac{M*}{M_M} = \frac{(1 + \xi\,\eta V_F)}{1 - \eta\,V_F} \tag{2.2}$$

where;

$M*$: represents composite moduli, (e.g. E_2, G_{12},.etc).

M_M: represents matrix modulus (e.g. E_M, G_M,.etc).

ξ: empirical factor

η: a non-dimensional factor equals to $\frac{\left(\frac{E_F}{E_M}\right)-1}{\left(\frac{E_F}{E_M}\right)+\xi}$

2.2.2. Laminates Characterisation

Composite laminates are usually defined in terms of their response to mechanical and sometimes thermal loading, which is usually linked to a description of the coupling action. It is often express the well-known ABD relation from classical lamination theory [62]:

1. In-plane load equation is presented by Eq. (2.3):

$$N = A\varepsilon^{O} + B\varepsilon^{1} \tag{2.3}$$

2. Bending moment equation is presented by Eq. (2.4):

$$M = B\varepsilon^{O} + D\varepsilon^{1} \tag{2.4}$$

where;

N: Normal forces

A: Extension stiffness matrix

ε: Strain matrix

B: Extension-Bending coupling matrix

M: Moment

D: Bending stiffness matrix

The coupling behaviour, which is based on the form of the elements in each of the extensional [A], coupling [B], and bending [D] stiffness matrices, as presented in Eq. (2.5) to Eq. (2.7).

$$[A_{ij}] = \sum_{k=1}^{n} [\overline{Q_{ij}}]_k t_k \tag{2.5}$$

$$[B_{ij}] = \sum_{k=1}^{n} [\overline{Q_{ij}}]_k t_k \overline{z_k} \tag{2.6}$$

$$[D_{ij}] = \sum_{k=1}^{n} [\overline{Q_{ij}}]_k t_k (t_k \overline{z_k^2} + \frac{t_k}{12}) \tag{2.7}$$

where;

$\overline{Q_{ij}}$: The off-axis laminae, that is, those whose fibres are at an angle to the global horizontal laminate direction.

t_k: Laminate thickness

$\overline{z_k}$: the distance of each lamina in the laminate with respect to the datum as shown in Figure 2-1

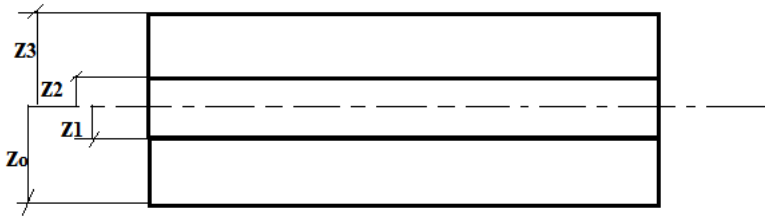

Figure 2- 1. the distance of each lamina in the laminate from the global horizontal datum.

Eq. (2.8) and Eq. (2.9) show the extended forms of the in-plane equation and the bending moment equation.

$$\begin{bmatrix} N_x \\ N_y \\ N_{xy} \end{bmatrix} = \begin{bmatrix} A_{11} & A_{12} & A_{16} \\ A_{21} & A_{22} & A_{26} \\ A_{61} & A_{62} & A_{66} \end{bmatrix} \begin{bmatrix} \varepsilon^0{}_x \\ \varepsilon^0{}_y \\ \gamma^0{}_{xy} \end{bmatrix} + \begin{bmatrix} B_{11} & B_{12} & B_{16} \\ B_{21} & B_{22} & B_{26} \\ B_{61} & B_{62} & B_{66} \end{bmatrix} \begin{bmatrix} \varepsilon^1{}_x \\ \varepsilon^1{}_y \\ \gamma^1{}_{xy} \end{bmatrix} \quad (2.8)$$

$$\begin{bmatrix} M_x \\ M_y \\ M_{xy} \end{bmatrix} = \begin{bmatrix} B_{11} & B_{12} & B_{16} \\ B_{21} & B_{22} & B_{26} \\ B_{61} & B_{62} & B_{66} \end{bmatrix} \begin{bmatrix} \varepsilon^0{}_x \\ \varepsilon^0{}_y \\ \gamma^0{}_{xy} \end{bmatrix} + \begin{bmatrix} D_{11} & D_{12} & D_{16} \\ D_{21} & D_{22} & D_{26} \\ D_{61} & D_{62} & D_{66} \end{bmatrix} \begin{bmatrix} \varepsilon^1{}_x \\ \varepsilon^1{}_y \\ \gamma^1{}_{xy} \end{bmatrix} \quad (2.9)$$

To remove the different types (e.g. bending, axial, twisting, etc.) of the couplings some elements of the stiffness matrices must be put to zero. Table 2-1 shows how to eliminate the different types of the coupling.

Table 2- 1. Elimination of the different types of coupling [62].

Case	Coupling	Decoupling	Elimination of coupling conditions
a) In-plane action and out-of-plane action	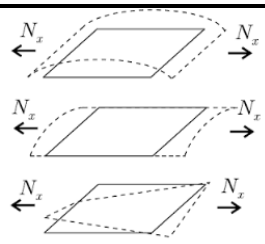	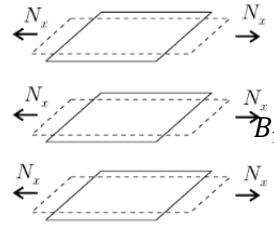	B_{11}= B_{12}=B_{66}=0
b) Normal action and shear action			A_{16}=A_{61} = A_{62}=A_{61}= 0
c) Normal action and twisting action	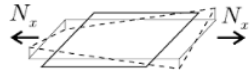	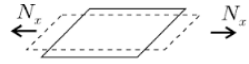	B_{16}= B_{26}=B_{61}= B_{62} = 0
d) bending action and twisting action	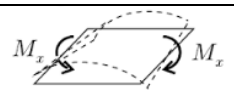	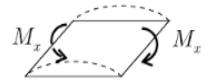	D_{61}= D_{62}= D_{26}=D_{62} = 0
e) All types of coupling	B_{11}=B_{12}=B_{66}= 0 A_{16}=A_{61} =A_{62}=A_{61}= 0 B_{16}=B_{26}=B_{61}=B_{62} = 0 D_{61}=D_{62}= D_{26}=D_{62} = 0		

In this study, the symmetric cross-ply design is adopted in order to simplify the laminate characteristics, eliminate the coupling between the normal and shear forces, and also between the bending and twisting moments. The symmetric design eliminates extension-coupling matrix [B].

The proposed laminate staking sequence is [0°/90°/0°/90°/0°] layup meaning that the in-plane/bending deformations are decoupled. The fibre glass composite micromechanics properties are computed using the Halpin-Tsai empirical approach as aforementioned.

2.3. Honeycomb optimisation

After the laminate characterisation, the Sequential Quadratic Programming (SQP) is considered to minimise the weight to bending stiffness ratio. Nonlinear constrained convex objective functions with linear/nonlinear equalities and inequalities are handled by this function.

The common failure modes of sandwich structures may happen due to severe shear force, intercellular buckling, core crushing, and punching shear [63]. The sandwich panel dimensions width, b, and length, *l,* are 0.2m× 0.2m respectively, and the honeycomb top and bottom faces are fibre glass with thickness, t_f, honeycomb height, *h,* and with wall thickness, t_c. The sandwich panel is treated as a shell structure considering the length/width are significantly larger than the height.

The top/bottom faces consist of five laminates with a combined thickness of t_f mm. Moreover, the research methodology workflow is presented in Figure 2-2.

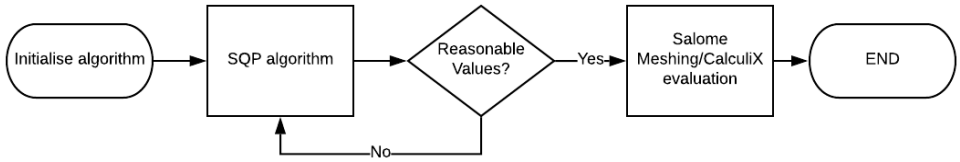

Figure 2- 2. Block diagram of the research methodology.

According to Bitzer [64] the equivalent bending stiffness of honeycomb sandwich panel D_{eq} can be computed using Eq. (2.10).

$$D_{eq} = \frac{tE_1h^2}{2\lambda} + \frac{E_1t^3}{6\lambda} + \frac{E_ct_c^3}{12\lambda_c} \tag{2.10}$$

where;

E_1 is longitudinal Young's modulus of faces

E_c is the honeycomb Young's modulus,

λ is equal to (1-$\upsilon_x \upsilon_y$) and υ_x, υ_y are Poisson's ratio in longitudinal and transverse directions of composite layer

λ_c is equal to (1-υ_s) and υ_s is Poisson's ratio of aluminum.

The weight is calculated using Eq. (2.11)

$$W = (g * b * l * (2 * \rho_f * t_f + \rho_{core} * h)) \quad (2.11)$$

where,

W: *the weight*

g : gravity acceleration,

b : breadth,

l : length and

ρ_{core} : honeycomb density

ρ_f : top/bottom face material density.

The "*Fmincon"* function in MATLAB ustilises sequential quadratic programming SQP algorithm to obtain the optimum minimum value. Therefore, the objective function is to minimise weight to bending stiffness which is formulated as in Eq. (2.12)

$$Minimise\ f(X) = \frac{Weight, W}{bending\ stiffness, D_{eq}} \quad (2.12)$$

The nonlinear constraints of the design are displacement δ and intercellular buckling P. The displacement at the panel centre should not exceed *span/100* under concentrated force 5000 N. The displacement of the panel at the centre can be computed by Eq. (2.13) [65], and the intercellular buckling load must be less than critical value as computed in Eq. (2.14).

$$\delta = 0.00406\frac{pa^4}{D_{eq}} \leq (span/100) \tag{2.13}$$

$$P < (P_c = KE_c(t_c)^3/((1-v_s^2) * s)) \tag{2.14}$$

where P is the concentrated force at panel's centre, *k* is 5.75, E_c is the honeycomb Young's modulus, The upper/lower limits of the design variables are tabulated in Table 2-2. SQP function tolerance is 10^{-6}.

Table 2- 2. Optimisation design variables with upper/lower bounds.

Design Variable	$x_{(1)}$	$x_{(2)}$	$x_{(3)}$
Geometric Parameter	t_f	h	t_c
Lower bound	0.0015	0.001	0.0001
Upper bound	0.002	0.010	0.001

As a side note, the positive definite Hessian matrix is a measure of function convexity over the domain [66]. Therefore, the eigenvalues of the Hessian have been computed and, they are positive. After computations, a local minimum that satisfies the nonlinear constrains has been detected. The iterations stopped as the objective function is non-decreasing in the feasible region. The buckling load factor (BLF) has been computed and it is larger than 1 which indicates safety of the honeycomb cell wall under buckling. The optimum values are tabulated in Table 2-3.

Table 2- 3. Honeycomb optimum values.

t_f (m)	H(m)	t_c(m)	W (N)	D_{eq}(N.m^2)	W/ D_{eq} (m^{-2})	*Intercellular Critical Buckling (N)*	*Buckling Load Factor*
0.002	0.01	0.0003	3.316	5.88e+03	5.6295e-04	1599.4	1.6

Figure 2-3 demonstrates the design of the honeycomb sandwich panel with two skin of glass fibre laminated plates (GFLPs) and the honeycomb layer.

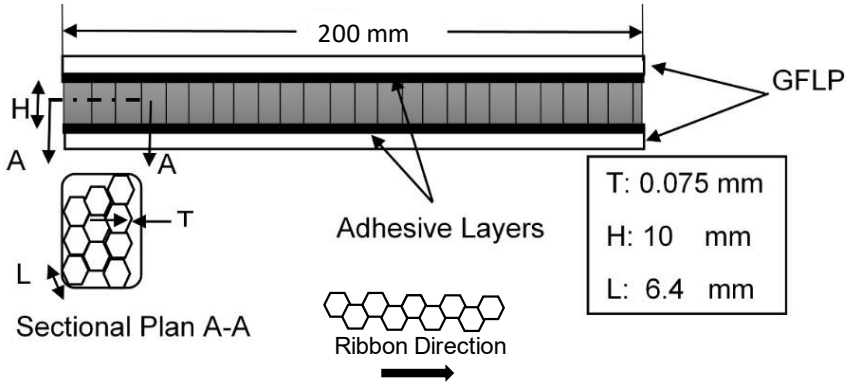

Figure 2- 3. HSP design and basic dimensions.

2.4. Numerical modelling

2.4.1. CalculiX FE Program

It becomes very common to use open-source finite element (FE) analysis packages because of the desire for a cost-effective way to run enormous amounts of data and analyses. Many laboratories and research groups are developing open-source FE to solve the finite element problems. Examples are, CalculiX, Code_Aster, Elmer and NGSolve.

CalculiX is a programme for solving problems using the finite element approach. CalculiX allows creating, calculating, and post-processing of Finite Element Models [67]. The solver can work with both linear and non-linear problems. There are options for static, dynamic, and thermal solutions [68], [69]. However, there is a need for meshing programmes before using CalculiX. The open-source mesh generation programmes include, Free Cad, GMSH, Salome and Open Foam. The basic advantages of CalculiX over the other open-source programmes are;

- Writing the analyses in a coding environment which makes them easier and quick,
- Error control in the analyses because everything is done through coding,
- And compatibility with Abaqus which helps in importing special elements, if needed.

CalculiX consists of two modules, namely, CalculiX Crunchix CCX which contains the equations and CalculiX Graphics CGX. CGX provides the user with many capabilities, mainly the pre/post – processing.

The steps of using CalculiX are demonstrated by Figure 2-4.

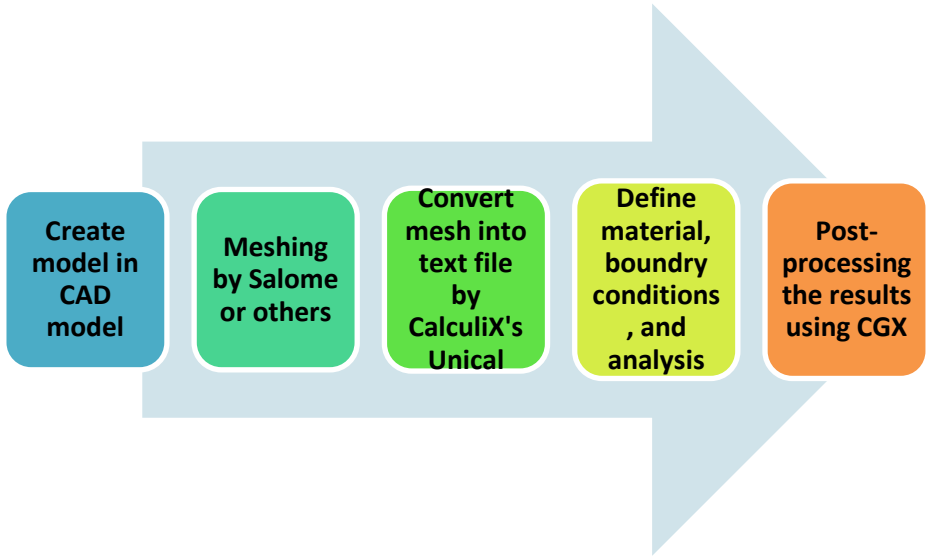

Figure 2- 4. Steps of using CalculiX Programme.

2.4.2. Model Description

To evaluate the optimisation results, a honeycomb composite panel of zero thickness is processed in Salome Platform and meshed with “S6” and “S8R” shell elements using Netgen 1D-2D option with maximum length 3 mm and minimum length 1.5 mm.

S8R element is a four-sided shell element that can be used for shell and composite materials [68]. Figure 2-5 shows the S8R element.

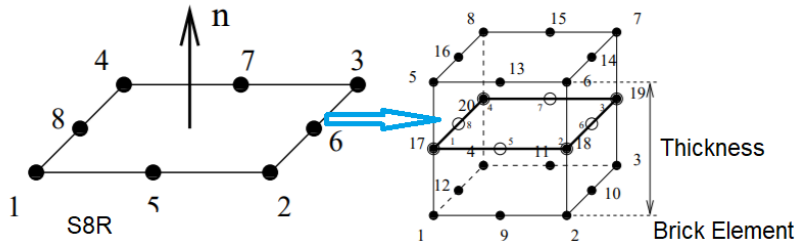

Figure 2- 5. Expansion of S8R shell element into 20 nodes brick element [68]**.**

In CalculiX, quadratic shell components are enlarged automatically into 20-node brick elements. Three additional nodes are created for each shell node. For a S8R element, a C3D20R element is generated using these nodes to give the thickness as the CAD model of the HSP is zero-thickness surface model. The generated C3D20R element is of the thickness of the HSP faces. Further, for better accuracy in solution, second order approximation for the meshing process is followed. However, care must be taken in meshing process as unlike commercial softwares, node-to-node connectivity is not assured for multiple surfaces automatically. Therefore, the sandwich panel must be partitioned into multiple shells and edges to assure the nodal connectivity. Therefore, there is a need for the 6 nodes shell elements (i.e. S6) to solve these problems and to ensure the uniformity and node-to-node connectivity. Figure 2-6 demonstrates the S6 characteristics.

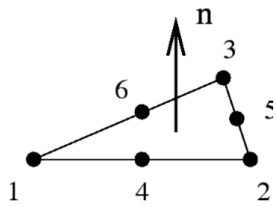

Figure 2- 6. S6 shell element [68]**.**

Yet, after partitioning it, the honeycomb core and top/bottom faces must be grouped and the two edges as well at the bottom face to form the elemental and nodal groups which will be used later for materials definitions and boundary conditions in CalculiX code later. The model descriptions are tabulated in Table 2-4. Figure 2-7 presents the HSP numerical model after meshing it in Salome.

Table 2- 4. Model description.

Length (mm)	200
Breadth (mm)	200
Glass Fibre Layer Thickness (mm)	2.5
Honeycomb Layer height (mm)	10
Number of S8R elements	18,309
Number of S6 elements	2,863

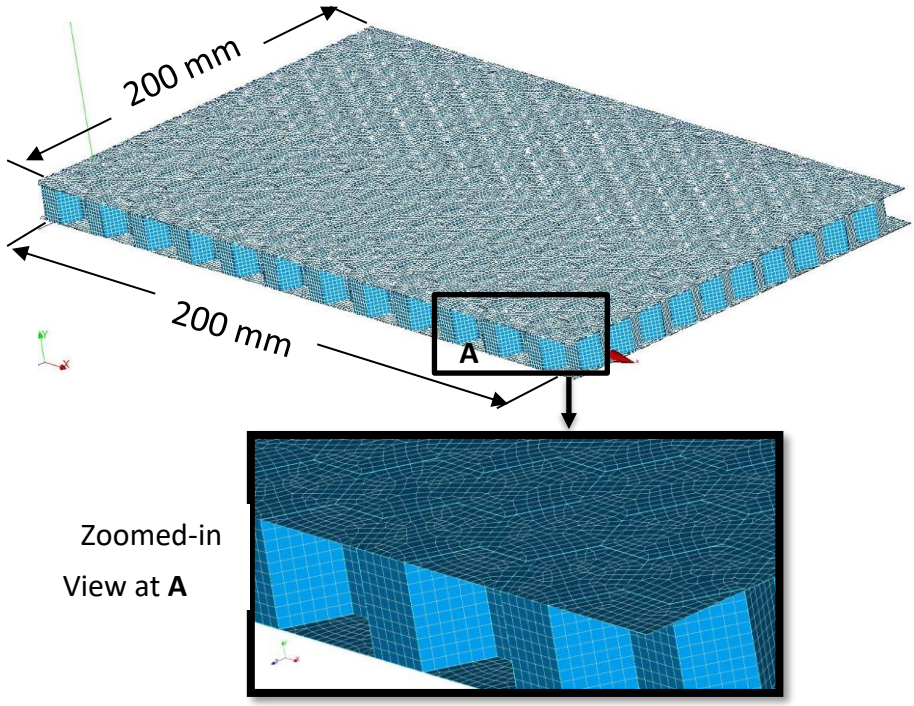

Figure 2- 7. Meshed honeycomb model.

The material of the model of the GFLP is characterised as orthotropic material while the Al-honeycomb layer is defined with the Young's modulus of the isotropic aluminium because the layer is modelled exactly. The general mechanical properties of both materials are tabulated in Table 2-5.

Table 2- 5. Material properties of the numerical model.

Layer	E_1 (GPa)	E_2 (GPa)	E_3 (GPa)	G_{12} (GPa)	υ_{12}	υ_{13}	ρ kg/m^3	V_f %	V_m %
GFLP-Skin	37.5	13	13	4.8	0.26	0.26	1875	55	45
Al Honeycomb	68	-	-	-	0.28	-	2700	-	-

2.5. Static Analysis

In order to inspect the structural behaviour of the developed HSP, the experimental and numerical three point bending test are carried out. The model is fixed as simply supported plate to conduct three point ending test as in ASTM standard [70], free-free-fixed-fixed ends. Figure 2-8 demonstrates the schematic drawing of the three-point bending test.

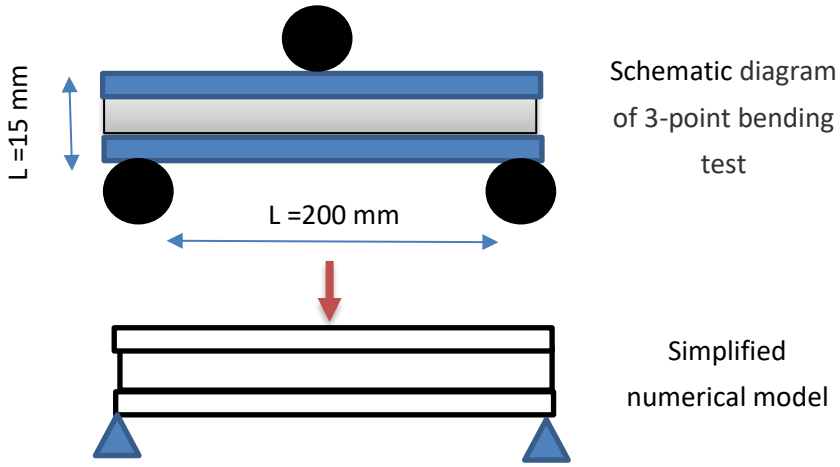

Figure 2- 8. schematic diagram of the static analysis.

Figure 2-9 shows the experimental three point bending test. The specimen size is 200×165×15 mms and the testing machine is from Servocon, Ltd., with maximum capacity of 100 KN. The manufacturing and ultrasound inspection of the specimen is provided in detail in Section 3.2.

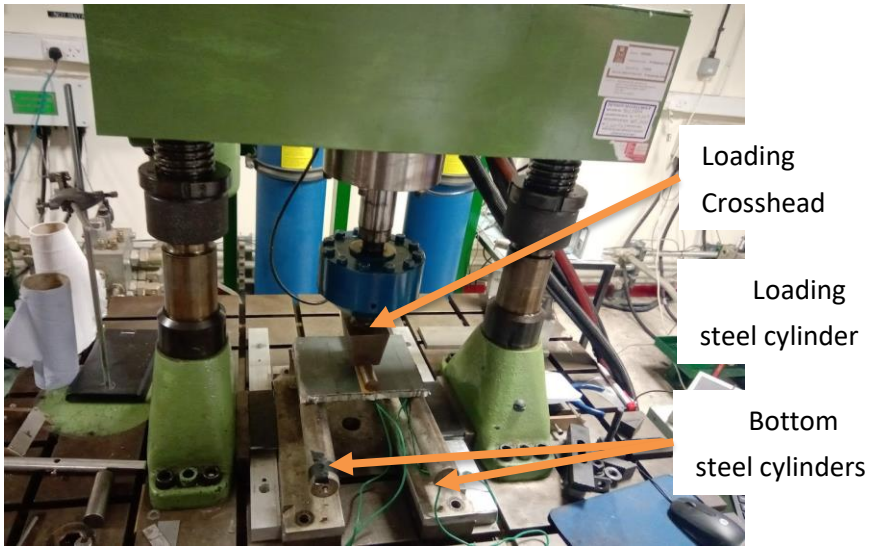

Figure 2- 9. Experimental three point bending test.

In the FE analysis, the fixed displacement is applied at centre and the reaction is recorded in order to reduce the modelling order and simplify the problem. Figure 2-10 presents the FE result of static test.

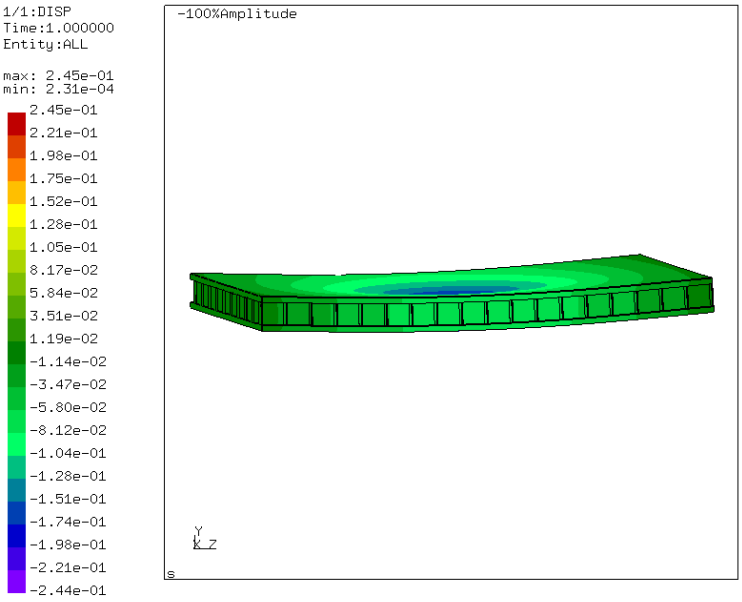

Figure 2- 10. FE result of the three-point bending test.

Figure 2-11 presents the FE and experimental results. The elastic range is in agreement for both FE and experimental results. It is worth mentioning that the deviation of the FE and experimental results is basically attributed to the reduced order simplification of the model.

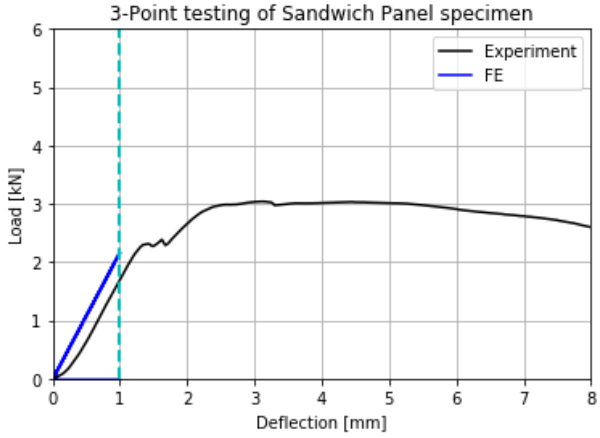

Figure 2- 11. Experiment and FE results of the three-point bending test.

2.6. Modal Analysis

The modal analysis has been conducted on the same numerical model but after removing the loading point. The first three mode shapes are appeared at 865, 991, and 2295 Hz as shown in Table 2- 6. The first two modes are in line with the results of Kumar et al. [71], as they used comparable aluminium honeycomb of 6 mm size and 7.98 mm height. However, the specimen size is less by 40 mm than the investigated model in this thesis and the faces are from aluminium.

Table 2- 6. The first three mode shapes of the HSP.

Mode number	Frequency (Hz)	Mode Shape
1	865	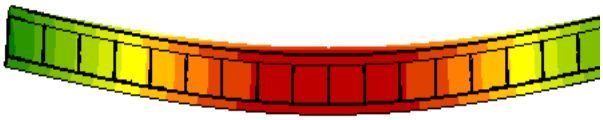
2	991	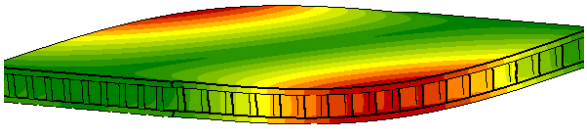
3	2295	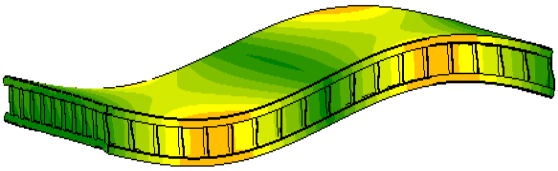

2.7. Summary

This chapter discussed the HSP modelling and parametric optimisation. The designed material is used in the next chapters for farther investigations.

The following points are the main output of this chapter:

- The ratio of weight to bending stiffness is minimised considering the intercellular buckling and lateral displacement as the main constraints' functions.
- The sequential quadratic programming is robust technique for providing the minimum values for the geometric properties of the optimum design.
- The HSP is simply supported to stick to the standards and because usually the HSP element is simply supported by two shear webs in the wind turbine blades.
- The optimum geometric parameters are the faces thickness, core height and core thickness. After the optimisation, numerical model is processed and meshed with S8R/S6 shell elements in Salome platform.
- The open-source finite element solver CalculiX is robust in calculating the numerical results for the three-point bending and modal testing.
- The S8R/S6 shell elements are linear and they did not track the non-linearity of the load-displacement curves.
- The modal analysis is carried out in order to characterise the natural frequencies and mode shapes.

Chapter 3: Wave Propagation Study

3.1. Introduction

This chapter investigates the following issues:

- Glass fibre laminated plate manufacturing and inspection using the ultrasonic phased array technique to assess the manufacturing quality.
- Nature of the directional acoustical wave propagation in the glass fibre plate and its basic features such as modes, wave velocity, frequency and attenuation characteristics.
- The mechanism of acoustical wave propagation in the sandwich structures consisting of limited number of the honeycomb cells. To quantify the effects of honeycomb cell on the AE wave propagation in the faces.
- The acoustical wave propagation in the honeycomb sandwich panel in top and bottom plates while the AE sensors are mounted on the top plate only.
- Acoustical wave characterisation on top plate of the honeycomb sandwich panel and the bottom plate.

These investigations have been carried out using Hsu-Nielsen technique and the laser vibrometry scanning in the different directions on the glass fibre plate since the alignment of the fibre contributes to the acoustical wave propagation.

3.2. Plate Preparation

3.2.1. Plate Manufacturing

The unidirectional glass fibre roll is purchased from Cristex, Ltd. The roll width is 1.2 m and the areal weight is 591 g/m^2. The weft weight percentage is approximately 7%. Overall weight of the roll is 50 kg. The

specimen used for this investigation consisted of honeycomb aluminum core sandwiched between two unidirectional fibre glass composite faces.

The glass fibre top and bottom plates consisted of five laminates each [0° /90°/0° /90°/0°] and total thickness is 2.5 mm per plate. The resin used is epoxy infusion IN2 from Easy Composites, Ltd. The characteristics of the resin are tabulated in Table 3-1.

Table 3-1. The properties of IN2 epoxy infusion resin.

Flexibility	Rigid
Max Service Temp	73°C
Hardness	86 (Hard)
Tensile Strength MPa	63.5 - 73.5
Flexural Strength MPa	112 – 124
Flexural Modulus GPa	3150 – 3550
Elongation at Break%	6.0 - 8.0
T_{glass} Onset (DMA) °C	92 – 98
Viscosity mPa.s	325

A slow hardener is used and the epoxy to hardener ratio is 100:30 and in order to prevent bubbles during the epoxy-hardener mixing, the mix is put inside a vacuum degassing chamber. The vacuum degassing chamber takes out the bubbles and hence, clean the mix from the potential voids. Figure 3-1 shows the degassing equipment. The degassing step took 15 minutes until no further bubbles received at the resin surface.

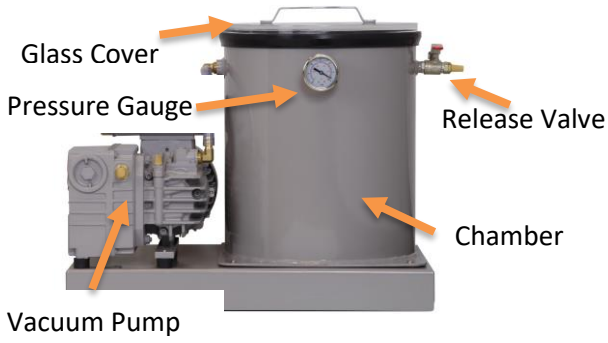

Figure 3- 1. The epoxy degassing chamber.

Furthermore, the amount of epoxy is divided per five vessels in order to reduce the degassing time and hence, starting infusion during the pot lifetime. Thereafter, the glass fibre laminated plate (GFLP) is manufactured by vacuum assisted resin infusion technique. Six spiral wound plastic tubes are placed equidistant on a nylon peel ply as shown in Figure 3-2. The tubes are pre-tensioned to provide evenly distributed resin within the laminates.

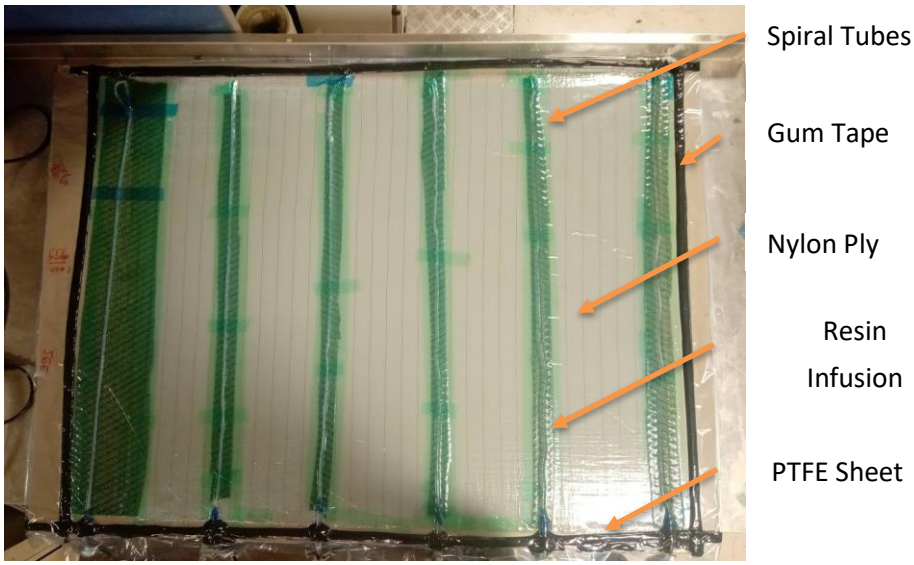

Figure 3- 2. Glass fibre laminated plate process design.

The vacuum pressure is achieved at -985 mbar, however, there was big leakage and by examination, it is found that thin threads of the ends of the glass fibre plate are between the gum tape and the vacuum bagging. These threads are the reason behind the leakage. To overcome this issue, using a lighter, the threads are burnt, and the laminates are free of them. A PTFE layer is placed over the base metallic plate to avoid leakage via the roughness of the metallic plate. Furthermore, the vacuum bagging is turned over the surface of the base metallic plate which upon it the glass fibre laminates are put. Figure 3-3 shows the vacuum bagging turning over the metallic edge to enhance process quality.

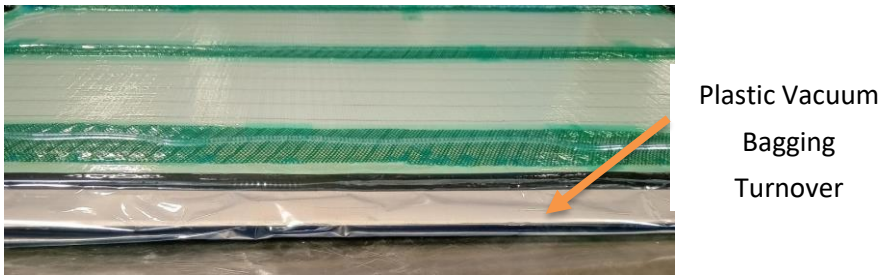

Figure 3- 3. Vacuum bagging is turned over the edge of the plate.

Furthermore, vacuum pressure drop test is carried out to inspect leakage and ensure the gum tape sealing quality. The vacuum pressure is -1010 mbar inside the plate after the epoxy resin infusion. Then, the plate is left for curing in room temperature for 24 hours. The plate's length and breadth are trimmed to 820 × 820 mm with tolerance (±5 mm) by using band saw machine with a diamond saw. Figure 3-4 presents the manufacturing process of the composite plate.

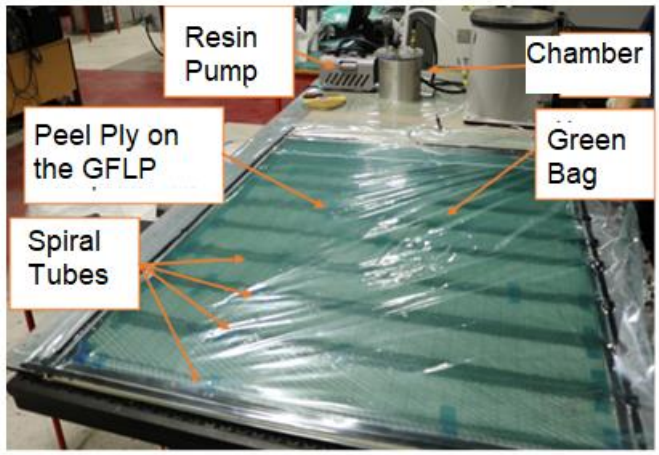

Figure 3- 4. Glass fibre manufacturing by vacuum resin infusion process.

3.2.2. Ultrasonic inspection

Ultrasonic testing (UT) is the process of using sound waves of frequencies beyond the human audible range to interact with the material

properties and hence, detecting flaws through the scattering and reflections [73].

However, sound wave propagation in inhomogeneous composite structures is quite complex because the random scattering and attenuation of the waves affect the probability of flaw detection.

Figure 3-5 shows the phased array ultrasound inspection system from Olympus, Ltd., and the water is used as a couplant between the ultrasound probe and the GFLP surface in order to reduce effect of the friction.

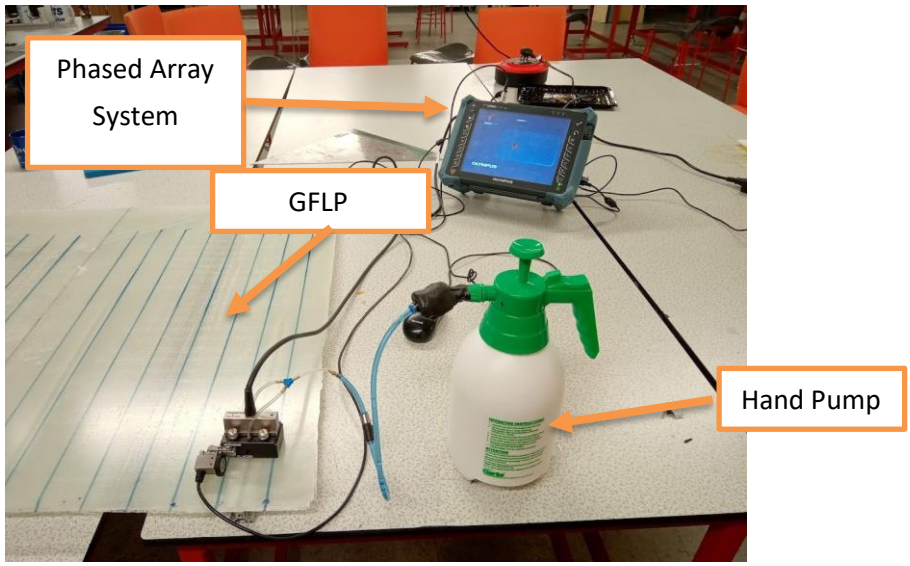

Figure 3- 5. GFLP inspection using phased array ultrasound.

The common displays of the UT signal is referred to A-SCAN, C-SCAN, and S-SCAN.

- A-SCAN is the presentation of the received UT pulse amplitude in 2D graph where the Y-axis is usually represents the amplitude amount and X-axis represents the travelling time.
- C-SCAN is the image produced from the UT dataset to show the changes within the thickness of the object.
- S-SCAN shows the sectorial scanning which is mainly associated to the phased array technique for UT.

Figure 3-6 presents the different UT displays for a defective carbon fibre specimen.

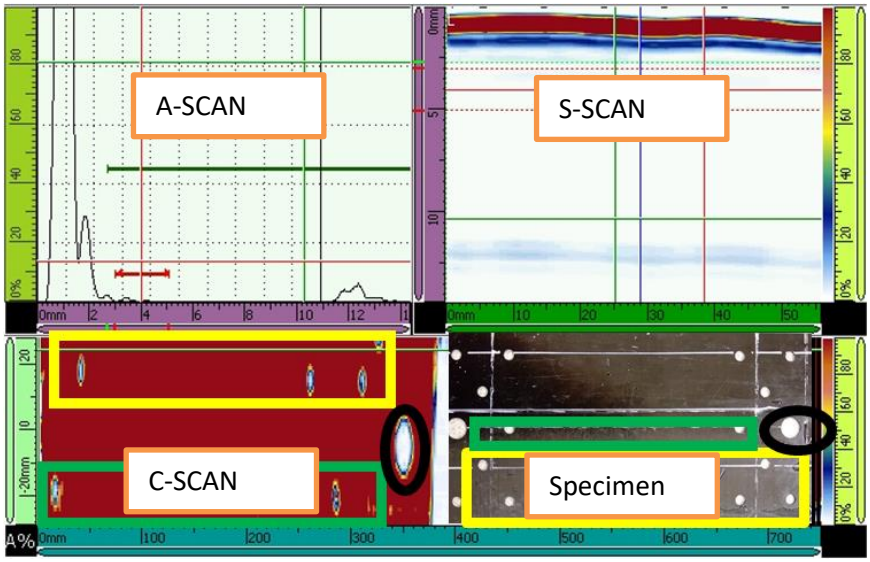

Figure 3- 6. UT data different displays.

Afterwards, the specimen is inspected using ultrasonic phased array to find out manufacturing defects before using it. The first specimen is defective due to the high suction pressure and poor infusion regions.

The high vacuum pressure compressed down the spiral tubes on the glass fibre plate. Figure 3-7 shows the ultrasonic scanning image.

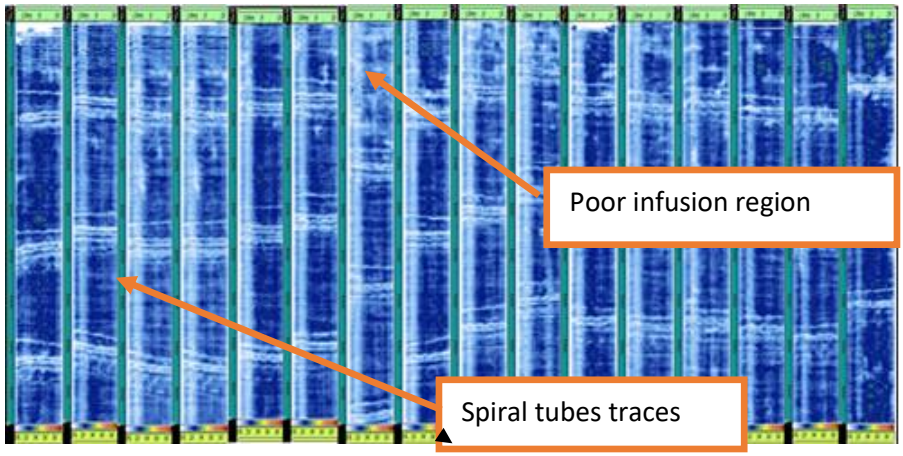

Figure 3- 7. Phased array- C- scanning of glass fibre plate.

These problems have been avoided in other specimens by using proper suction pressure of -1002 mbar and avoiding high suction pressures. Further, double mesh has been placed under each spiral tube to act as a cushion while infusion. To avoid the bad infusion region, each spiral tube is pre-tensioned in order that the epoxy could flow evenly and smoothly.

3.3. HSP Manufacturing

The HSP is comprised a hexagonal cell honeycomb (Easy Composite, Ltd.) 10 mm tall with 6.4 mm cell size, wall thickness 0.075 mm of 3003 series aluminium alloy, bonded to the two GFLPs using the Permabond ET-538 and cured under compression for 24 hours. Figure 3-8 presents the geometric features of the panel.

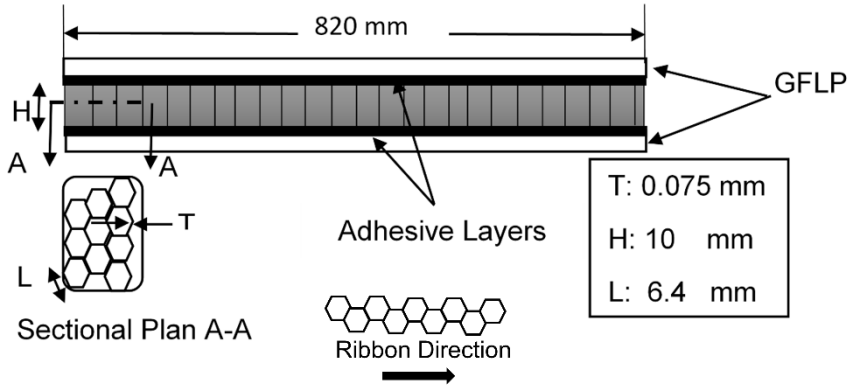

Figure 3- 8. Aluminium honeycomb sandwich structure.

3.4. H-N Method

3.4.1. Glass Fibre Laminated Plate

The glass fibre laminated plate is simply supported on two rigid aluminum supports. It is important to make sure that all surfaces of the panel are not in direct contact with the testing table surface to prevent any interruption to the acoustical wave propagation. Figure 3-9 presents a schematic drawing of the AE test apparatus. Two wide band differential AE sensors (WD sensor from Mistras, Ltd,.) are used; one (S_1) is fixed on

the centre using silicon and another (S_2) is placed 100 mm apart from the central sensor using grease as the acoustic couplant. The WD sensor has a wide range of operating frequencies, with operating range of 100 kHz to 1000 KHz. However, it is also sensitive to the lower frequencies than 100 KHz. More information can be found in Annex B. The sensors are attached to pre-amplifiers and the gain is selected to be 40 dB. After that, the output BNC cables from the pre-amplifiers are fixed to a Mistras Ltd AEWin based PCI-2, eight-channels acquisition system. The sampling frequency is 5 MHz and maximum frequency of the signal band is 1 MHz which satisfied Shannon's theorem.

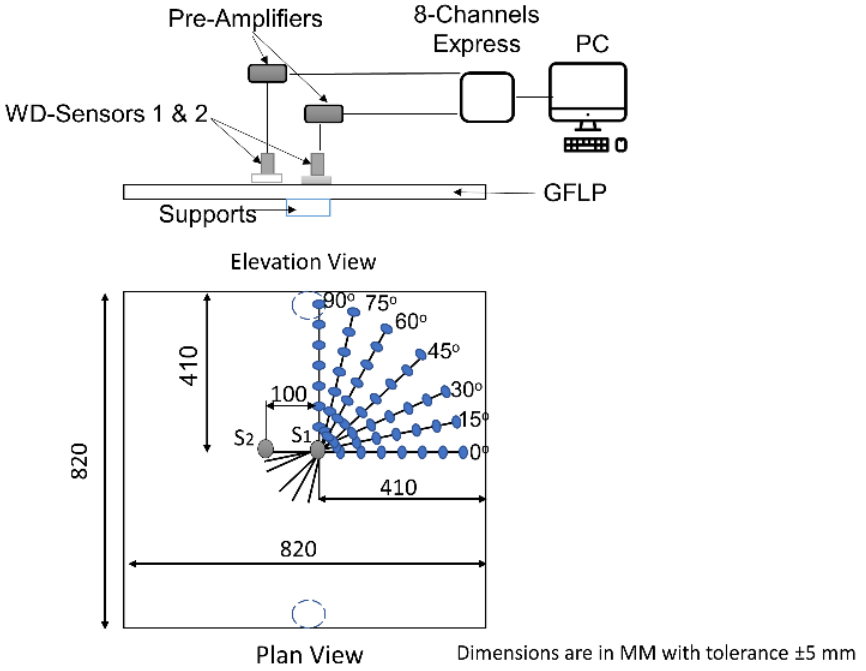

Figure 3- 9. Schematic drawing of test apparatus.

Furthermore, on the top right-hand quarter of the fibre glass laminated plate, angular lines are drawn to cover the area from 0° to 90° with interval 15° with tolerance range [±1°].

For each direction, artificial AE sources are generated at distances of 50, 100, 150, 200, 250, and 300 mm from the central sensor; in order to

improve the reliability of the result, five events are generated at each distance so that an average could be obtained. The experimental setup is presented in Figure 3-10.

It is worth mentioning that this plate is designed with such large surface area to obtain a guided AE wave with relatively low reflections.

The timing parameters HLT, PDT, and HDT are 300, 100, and 200 µs respectively and the threshold level is 40 dB.

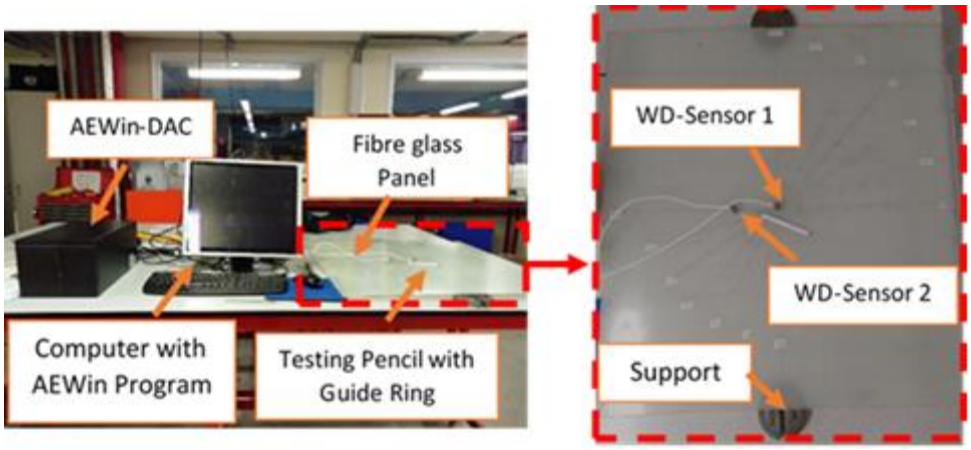

Figure 3- 10. Experimental test setup.

3.4.2. Limited Cells Specimens

Before studying the wave propagation in the honeycomb sandwich structure, a propagation study is carried out on the bespoke HSP specimens. The size of each GFLP is 200 × 75 × 2.5 mm. A WD sensor is bonded to the top plate using silicone at 180 mm in length and 32.5 mm in breadth as clear in Figure 3-11.

The two plates are first connected by a single honeycomb cell, using Permabond ET-538 epoxy, at distance 150 mm from the WD sensor. Five H-N events are generated on the bottom plate just under the cell to take the average energy of the transmitted AE.

AE timing parameters are 100, 200, and 400 μs for the PDT, HDT and HLT, respectively. The preamplifier is set to a gain 40 dB with a frequency range from 20 kHz to 1200 kHz. The threshold level is 40 dB and the sampling rate is 5 MHz.

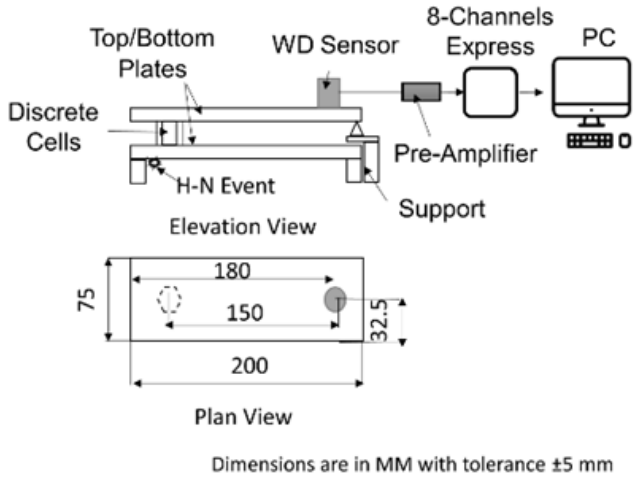

Figure 3- 11. AE wave propagation test setup for bespoke HSPs.

Upon generating an H-N source on one GFLP and recording AE with a sensor on the opposing GFLP, it is discovered that AE energy did transmit through the honeycomb cells and able to excite the other plate with a Lamb wave. Figure 3-12 gives examples of AE hit recordings from the top GFLP when H-N sources are generated on the bottom GFLP for several samples, each with different numbers of cells. It appears that the unit honeycomb cell edges act as a new source of AE in the top plate that excites out-of-plane motion on that plate.

Subsequently, Lamb waves form within the top plate from this source, because of the plate geometry, stiffness and the guided wave effect. It can be seen that the amplitude of the Lamb wave modes recorded increase in line with the number of discrete as a result of the increase in energy transfer from the bottom plate through the honeycomb cells. It can be seen that the S_o mode appears with relatively low amplitudes but

definitely higher than the noise amplitude level as shown in Figures 3-12(a, b, and c) that present the overall waveform, the S_o mode region in the waveform and corresponding FFT of one cell, 2 cells and 5 cells cases. However, as the number of discrete cells increases, it becomes harder to distinguish Lamb wave S_o mode on the top plate as shown in Figure 3-12(d). As a result of increasing the honeycomb cells, the out-of-plane excitation on the top plate causes interruption for a clearly distinguished Lamb wave modes formation. Further, the continuous energy pulses from each cell boost the out-of-plane motion on top plate that's why A_o mode is clearly distinguished by its shape in the waveform and frequency as shown in Figure 3-12 (d).

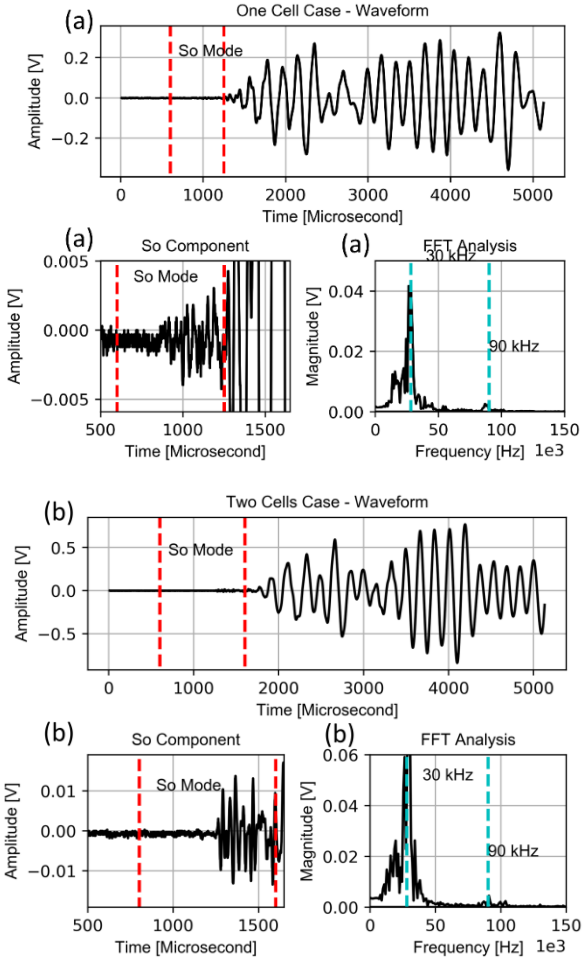

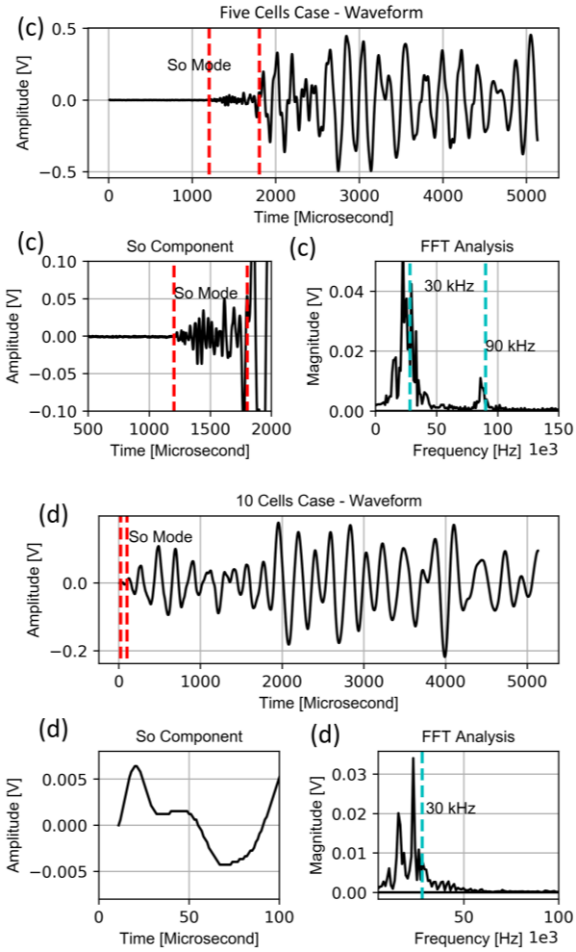

Figure 3- 12. Waveforms, FFT analysis and zoomed-in S_o region in (a) one cell case, (b) two cells case, (c) five cells case and (d) ten cells case.

When considering a small number of cells, the amplitude of Lamb waves in the top plate increases in line with the number of cells because of the increase in energy transfer from the bottom plate; the relationship between the number of cells and the energy of the AE hit recorded is given in Figure 3-13. Curiously, as number of cells is increased further, energy of the AE hit received by the sensor on top plate diminishes; it is hypothesised that this is because, once honeycomb cells span the entire surface area of the panel, it is possible for energy transmitted to top

surface to be absorbed back into honeycomb cells which lie ahead of it on its propagation path.

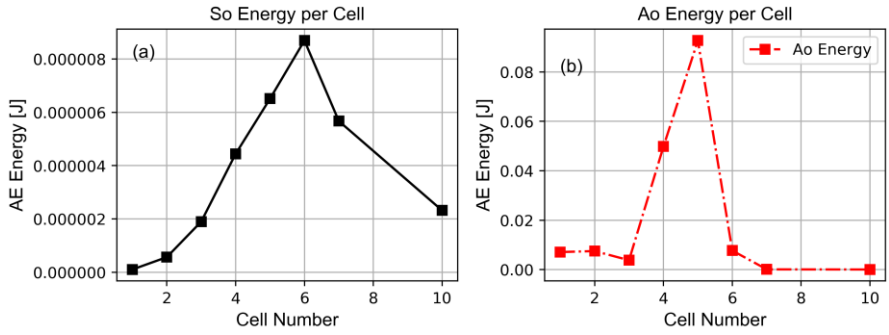

Figure 3- 13. AE energy levels for different bespoke HSPs, (a) S_o and (b) A_o.

3.4.3. HSP

The propagation study on the large HSP is conducted following a similar procedure to that is used on the GFLP, with the addition of one WD sensor bonded onto the bottom GFLP of the HSP as shown in Figure 3-14.

AE recording parameters are 100, 200, and 300 µs for the PDT, HDT and HLT, respectively. The preamplifier gain is 40 dB with a frequency range from 20 kHz to 1200 kHz. The threshold level is 40 dB and sample rate 5 MHz.

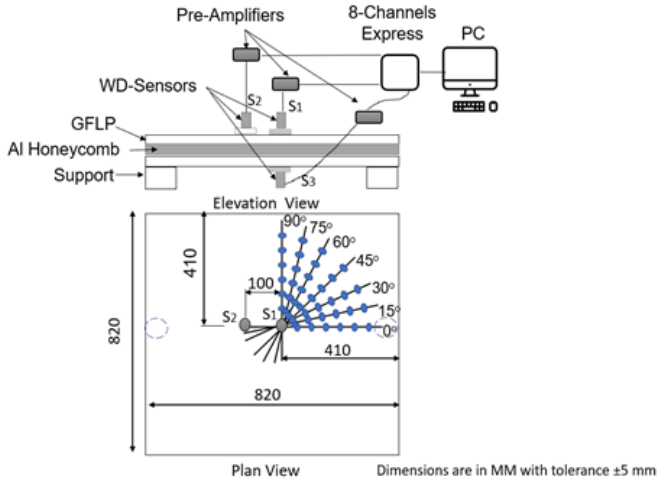

Figure 3- 14. AE propagation study test apparatus for HSP.

3.5. H-N Method Results

3.5.1. Attenuation Characteristics

AE wave propagation is affected not only by the material elastic properties but also by the geometry of the structure (e.g. holes, stiffeners, fibre alignment etc.) and the type of surrounding media (e.g. water, air, etc.). Therefore, wave attenuation study is worthwhile to ensure that AE sensors can be positioned appropriately on large honeycomb sandwich structures such as wind turbine blades.

The artificial AE sources are generated in different angles from 0^o to 90^o with interval 15^o on the glass fibre laminated plate, top skin, and the bottom skin of the sandwich panel.

The Lamb wave is found to be propagating in the free GFLP as expected, and in the top plate of the HSP. However, the waveform detected by S_3 does not take the Lamb wave form.

A_o peak amplitude is detected and calculated using a MATLAB script, for both the free GFLP and the top plate of the HSP. The S_o mode is calculated by windowing it then computing the maximum amplitude.

Figure 3-15 presents the waveform of in the 45^o direction on the free GFLP, top and bottom plates of the HSP with the dominant frequencies. The dominant frequencies for all directions for the propagating Lamb waves are averaged at 30 KHz and 90 KHz for A_o and S_o modes respectively.

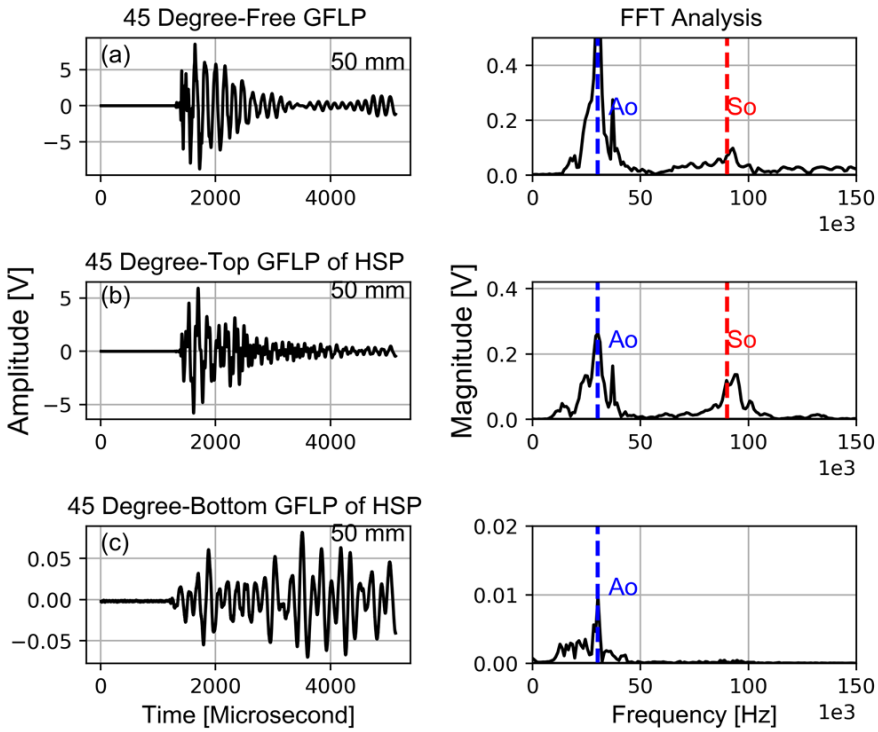

Figure 3- 15. AE waveforms in the 45o direction on a) free GFLP, b) top plate of HSP and c) bottom plate of HSP.

Eq. (3.1) presents the calculation of the decibel value for the amplitudes of the AE waveforms.

$$A_{dB} = 20 \times \log \frac{V}{V_{Ref}} \tag{3.1}$$

where;

A_{dB}: AE wave amplitude in decibel.

V: -AE wave amplitude in volt.

V_{Ref}: reference amplitude in volt and equals to 0.0001 V.

Figure 3-16 presents the attenuation behaviour of the A_o and S_o modes for the 0°, 45°, and 90° directions and the attenuation rate for the free GFLP and HSP. The gradient of the best fit lines presented in Figure 3-16 give the overall attenuation of the signal with distance without

removing geometric spreading effects. It is worth mentioning that since the amplitudes are in dB the trend line equation which used in the calculations is presented by Eq. (3.2).

$$A * = -\alpha x + c \tag{3.2}$$

where;

$A *$: Amplitude of A_o or S_o.

α: Attenuation rate dB/m.

x: The distance of the AE source from the receiving sensor.

c: The interception of the trending equation with the Y- axis.

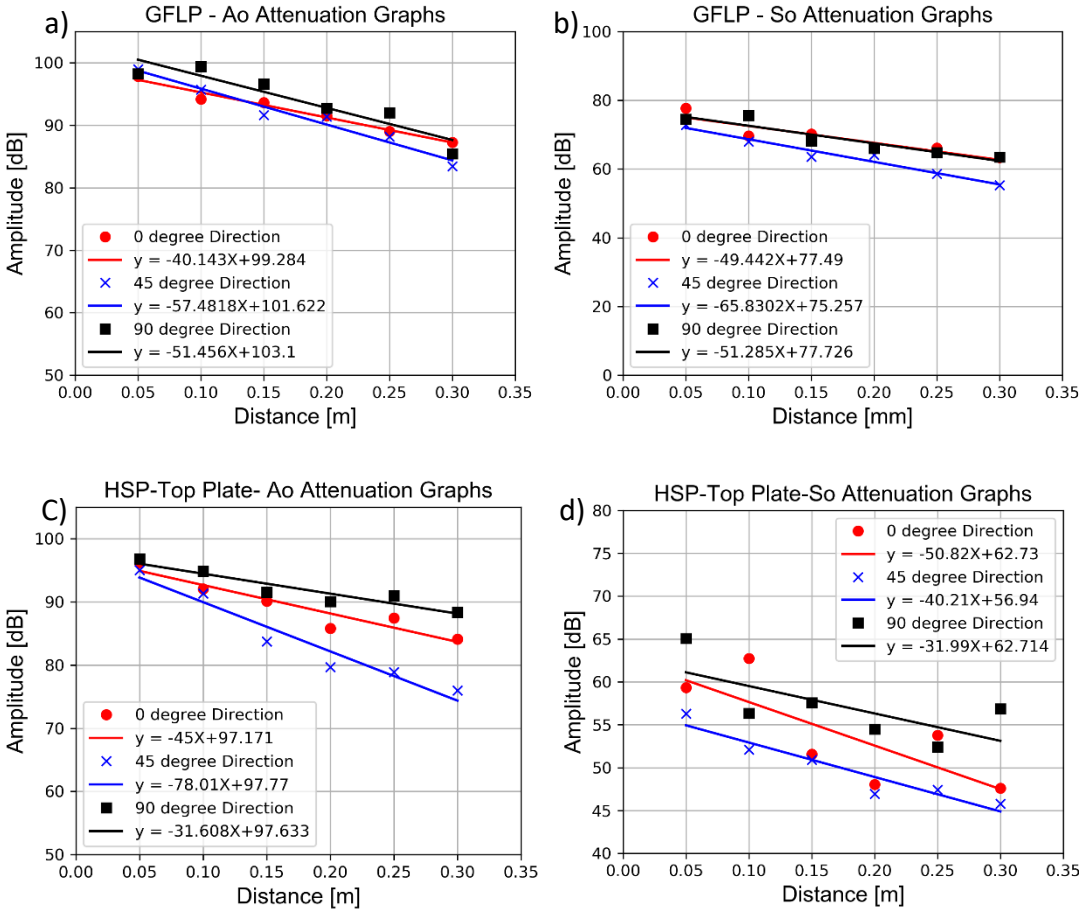

Figure 3- 16. Attenuation characteristics of the A_o and S_o modes for different cases.

On the other hand, the S_o mode of the AE wave recorded from the bottom, receiving surface of the HSP, is undiscernible above the noise, its amplitude could not be reliably identified, thus only the maximum A_o peak of the bottom surface is considered as shown in Figure 3-17.

The travelling AE wave from top surface to bottom one causes continuous out-of-plane pulsing and this increases the peaks of the waveforms in the bottom plate.

The high frequencies attenuation is significantly increased due to the honeycomb introduction which is in line with the study of Guo et al., [39].

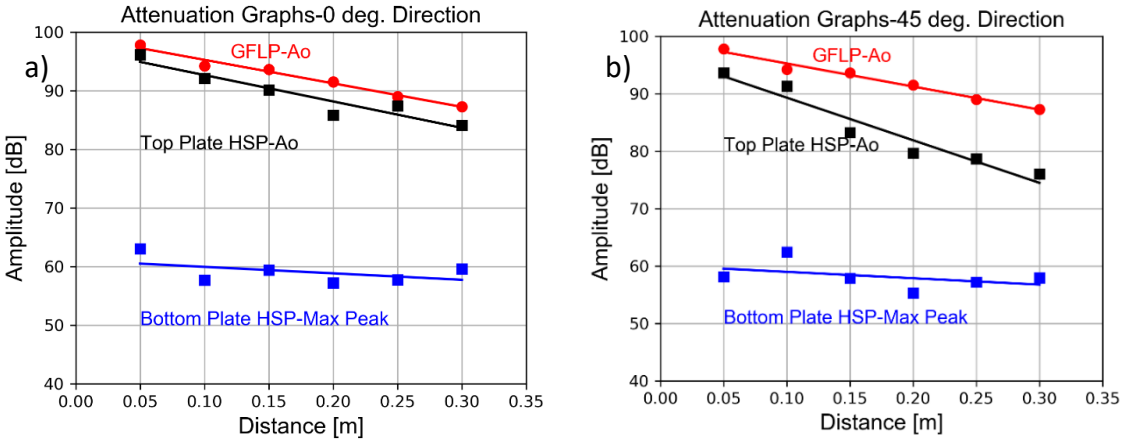

Figure 3- 17. Attenuation characteristics of the A_o comparison for free GFLP, top plate of HSP and bottom plate at a) 0° and b) 45°.

AE wave attenuation is dramatically increased after bonding the honeycomb layer, as energy scatters or leaks into the cells, conforming with the findings of Song et al. [72]. Figure 3-18 shows the energy of AE hits recorded at different distances in the GFLP, and the top and bottom plates of the HSP. As expected, there is a large loss in energy of the received signal when the propagation path includes transmission through the honeycomb calls to the opposing side of the HSP.

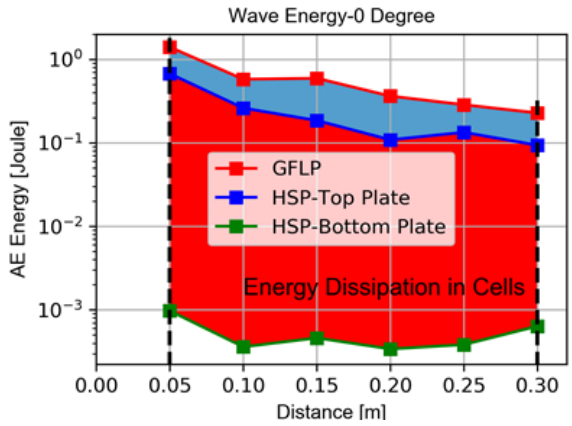

Figure 3- 18. Energy dissipation between GFLP, top and bottom plates of the HSP

Looking more specifically the signal amplitudes, Figure 3-19 compares waveforms recorded from the GFLP (i.e. peak 6.584 V), and top plate (i.e. peak 3.781 V) and bottom plate of the HSP (i.e. peak 0.0796 V); all from events generated along the 0° direction at 100 mm from the sensors. As expected, the amplitude of the hit from the GFLP alone is the greatest, followed by that from the top plate of the HSP (the plate where AE source is generated on), followed by that from the bottom, receiving plate of HSP.

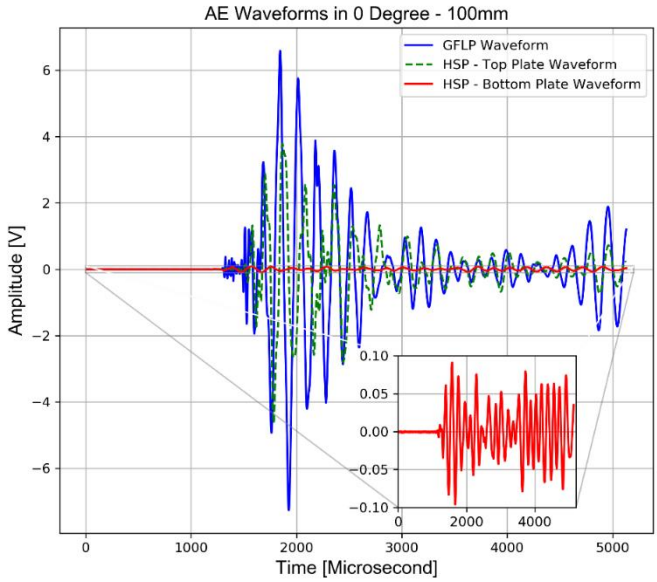

Figure 3- 19. AE waveforms in 0° direction at 100 mm from S_1 and S_3 for free GFLP, top plate and bottom plate of HSP.

Since there is a change in the AE signal amplitude after the addition of the honeycomb layer, the concept of ***'insertion loss'*** is proposed to describe the effect. In telecommunication, the insertion loss is defined as the signal power loss after inserting a component or network in the transmission line [73]. Eq. (3.3) presents the insertion loss equation.

$$\text{Insertion loss} = 20 \times \log \frac{V_{\text{before adding honeycomb}}}{V_{\text{after adding honeycomb}}} \qquad (3.3)$$

where;

$V_{\text{before adding honeycomb}}$:signal amplitude before inserting the honeycomb,

$V_{\text{after adding honeycomb}}$: signal amplitude after inserting the honeycomb.

By analogy, AE propagating in a composite plate will be affected after inserting the honeycomb and bonding it to the second composite plate to form the HSP; the insertion loss could be used to describe the severity of the change. Following this line of thinking and maintaining the form of Eq. (3.3), would be considered as the peak voltage of the AE hit recorded from the GFLP alone, and the becomes the peak voltage of a hit recorded from the top panel of the HSP. Figure 3-20 shows the approximate modelling of the AE wave propagation paths in the HSP.

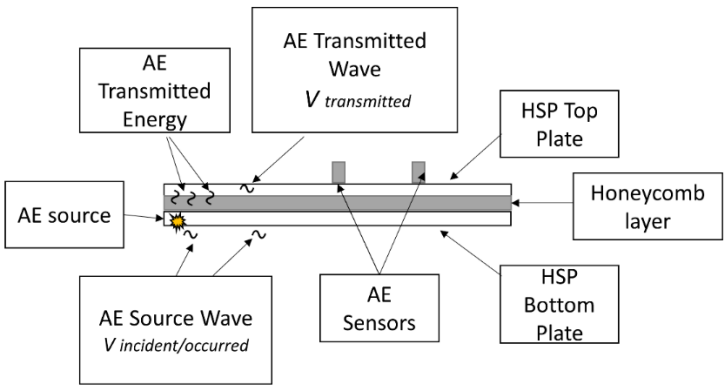

Figure 3- 20. Approximate model AE wave propagation paths.

By applying this process to the waveforms, comparing AE from the GFLP alone and the top GFLP of the HSP, the insertion loss is 4.8 dB. The same approach can be used to compare AE from the top GFLP of the HSP, where the source is generated, and the bottom GFLP of the HSP, which received transmitted energy, resulting in an insertion loss of 33.5 dB.

Therefore, the peak amplitude of a wave propagating 100 mm will drop 4.8 dB due to bonding the honeycomb and second GFLP to the top GFLP; and the peak amplitude of a wave propagating 100 mm and transmitting from one side of the HSP to another will drop by 33.5 dB.

The attenuation rates for A_o and S_o in various angles, are plotted as in Figure 3-21. Overall, the attenuation rate of S_o in the free GFLP is higher than that in the top plate despite the amplitude reduction, this could be attributed to the effects of the change in the in-plane stiffness and the ribbon effects on the path of that mode. Since the A_o is a flexural mode, the attenuation rate become higher because of the high out-of-plane stiffness of the HSP. In the bottom plate, the waveform is kept injecting from top plate via the honeycomb cells and that behaviour cause the continuous increase in the received peaks. That is why the attenuation rate is almost independent of the angle of the fibre glass.

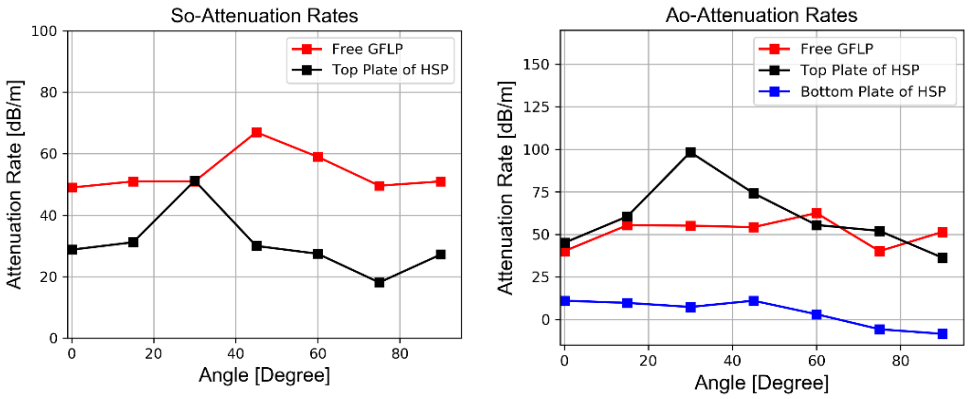

Figure 3- 21. Attenuation Rates- Different Cases.

3.5.2. Velocity Measurements

In order to calculate the velocities of the two modes, it is necessary to know their arrival time at each sensor. The Akaike Information Criterion (AIC) picker is used to determine an accurate first arrival time of both Lamb wave modes. Figure 3-22 shows the whole signals processing sequence to determine the A_o group velocity. It should be noted that to utilise the AIC function to identify the onset of the A_o mode, the signal is first passed through a low pass Butterworth filter with a normalized cut off frequency at 45 kHz, to eliminate the S_o mode energy.

White Gaussian Noise (WGN) is then added to this filtered signal to mimic the unfiltered AE signal [74] and allow the AIC function to calculate the arrival time of A_o mode much accurate. Additive white Gaussian noise (AWGN) is a basic noise model used in information theory to mimic the effect of many random processes that occur in nature. Shortly, AWGN procedure begins by measuring the power of the signal (e.g. vector z) using Eq. (3.4) for a defined signal to noise ratio (SNR in dB)

$$E_s = \frac{1}{l}\sum_{i=0}^{l-1}|z[i]|^2 \tag{3.4}$$

where E_s is the signal power, and l is the length of vector (z). Afterwards, the WGN can be added using Eq. (3.5) considering SNR as linear value.

$$WGN = \sqrt{\frac{E_s}{SNR_{linear}}} \times Random\ Number \tag{3.5}$$

In the end, the generated noise vector WGN is added to the AE signal. Figure 3-23 shows two examples of waveforms with the AIC picker. These waveforms are detected by sensors S_1 and S_2.

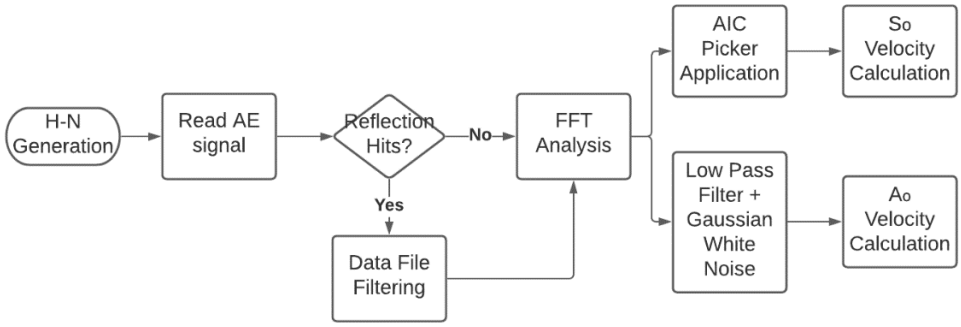

Figure 3- 22. Signal processing sequence.

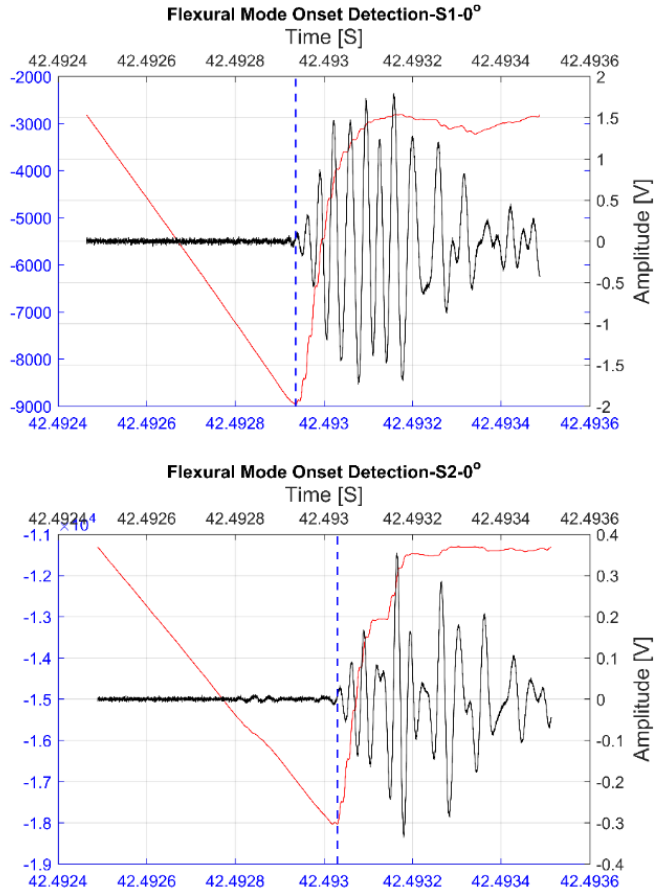

Figure 3- 23. The time of arrival difference determination for S_o mode in 0° to calculate group velocity.

With accurate arrival times known, the velocities of each mode are calculated for each direction tested, for both the GFLP and the HSP, by dividing the difference in the time of arrival of the signal at by the distance

between them, see Figure 3-9 for reference; the results of this process can be seen in Figure 3-24.

The maximum group velocities of the S_o mode in the GFLP are found to be 4028 (± 9.64) m/s and 4005 (± 15.76) m/s in 0° and 90° directions respectively. The minimum group velocity is 3472 (± 10.35) m/s in the 45° direction. This trend is expected as the S_o mode propagates with radial in-plane motion [75] thus its velocity is proportional to the in-plane stiffness, as shown Figure 3-24a.

Conversely, the velocity of the A_o mode is independent of the fibre orientation as it propagates with out-of-plane motion, thus its velocity is linked to the out-of-plane stiffness [23]. The average A_o velocity in the GFLP is found to be 1323 (± 58) m/s. The velocity results for the HSP, in Figure 3-24b, show that the addition of the sandwich structure had a notable effect on the velocity of the S_o mode. The maximum S_o velocities in the HSP are 3927.22 (±8.28) m/s and 3892.76 (±15.42) m/s in the 15° and 75° directions, respectively, with the velocity gradually diminishing either side of these directions.

It could be hypothesised that, in the HSP, the S_o velocity depends less on the fibre direction of the GFLP and more on the ribbon direction of the honeycomb core. The honeycomb core has increased stiffness along its ribbon direction, and the 60° separation in the directions of the maximum S_o velocities match the 60° angle between one ribbon direction and the next in a hexagonal honeycomb cell core, suggesting that the cells could act as a waveguide for S_o mode. On the other hand, the S_o velocities in 0° and 90° drop to 3637.36 (±33.97) m/s and 3752.15 (±9.02) m/s respectively, which can be attributed to energy scattering into the honeycomb cells [72].

The A_o velocity remains largely unchanged in the top plate of the HSP when compared to the GFLP alone, with an average of 1290 (±86.5) m/s.

This is striking as the purpose of the honeycomb layer is to increase the out-of-plane stiffness of the whole panel, though insight could be gained here by considering the scale at which the stiffness change occurs, i.e. macro vs micro.

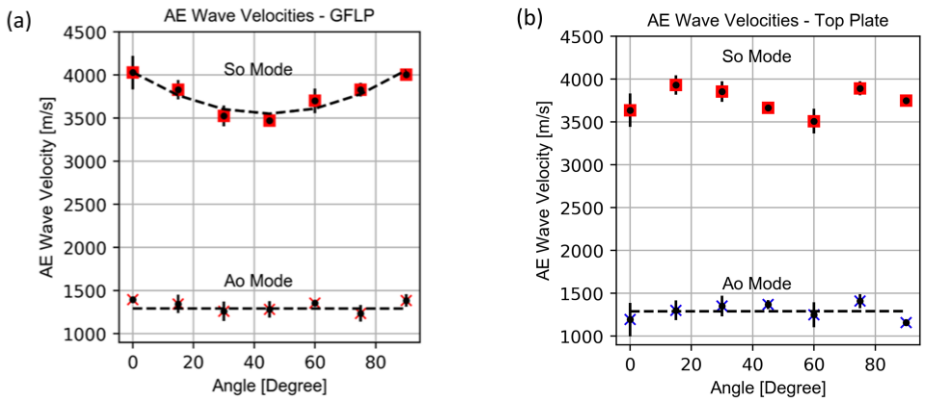

Figure 3- 24. Lamb wave group velocities on (a) GFLP and (b) Top plate of HSP.

Furthermore, the dispersion curve per each direction is calculated theoretically and the experimental apparent group velocity is compared to the theoretical one. The theoretical dispersions curves are calculated using LAMSS-COMPOSITE software [76]. The LAMSS-COMPOSITE is open-source programme in the form of graphic user interface in MATLAB environment which helps in retrieving and displaying the dispersion curves associated with the Lamb waves in the thin plates.

However, it is worth mentioning that the fibre glass model in LAMSS-COMPOSITE software is woven, however, its stiffness matrix is comparable to the used GFLP properties. Further, the group velocities of the waves for woven glass fibre plate are close to our unidirectional GFLP as in Wu's study [36]. It has already been established that the propagating frequency of the S_o mode centred at 90 kHz; given the GFLP thickness of 2.5 mm, this results in a frequency-thickness of 225 kHz.mm.

Figure 3-25 shows that for the 0^o direction, at frequency-thickness 225 kHz.mm, the theoretical S_o mode velocity is 3775 m/s; this is in-line with the velocity of the S_o frequency found experimentally in the corresponding direction, with an error of 3.8%. As for the A_o mode, it has

been established that the propagating frequency is centred at approximately 30 kHz, resulting in a frequency-thickness of 75 kHz.mm. The dispersion curve shows the A_o velocity to be 1185m/s in the 0^o direction, for a frequency-thickness of 75 kHz.mm.

This is comparable to the A_o velocity determined experimentally at that direction, with error 8%. This comparison has demonstrated that the experimental findings for the propagation properties of the S_o and A_o modes in the GFLP and top plate of HSP are in line with theoretical expectations.

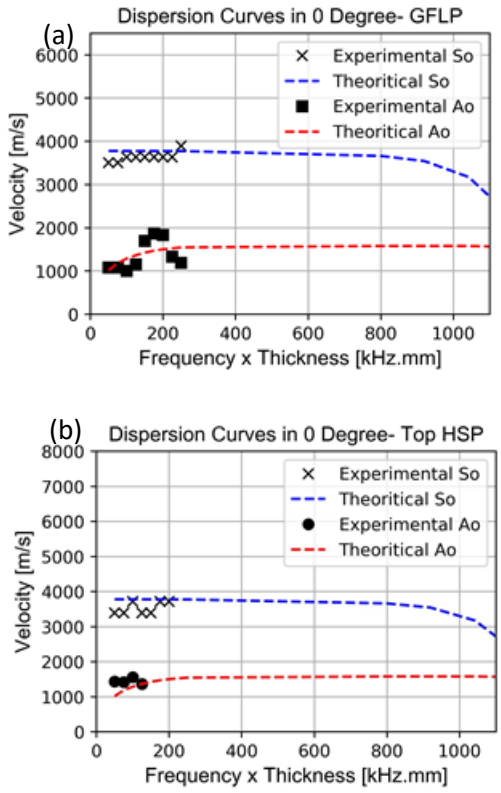

Figure 3- 25. Theoretical dispersion curves on 0^o direction (a) GFLP and (b) Top HSP

3.5.3. Wavelet Transformation

As a result of fast Fourier transform (FFT)'s inability to provide a time-dependence of the signal frequency spectrum, the wavelet transform

(WT) has been performed on the AE signals in 0^{o} direction at 50 mm. Wavelet transform is using short waveform segments as a basis function to determine the frequency spectrum in the time domain.

This offers many details on the characteristics of the AE signal. Figure 3-26 to Figure 3-28 present the wavelet transformation for AE wave in the GFLP, top plate of the HSP and bottom plate of the HSP. The wavelet transformation has been calculated using AGU-Vallen Wavelet freeware. The wavelet type is Gabor transformation.

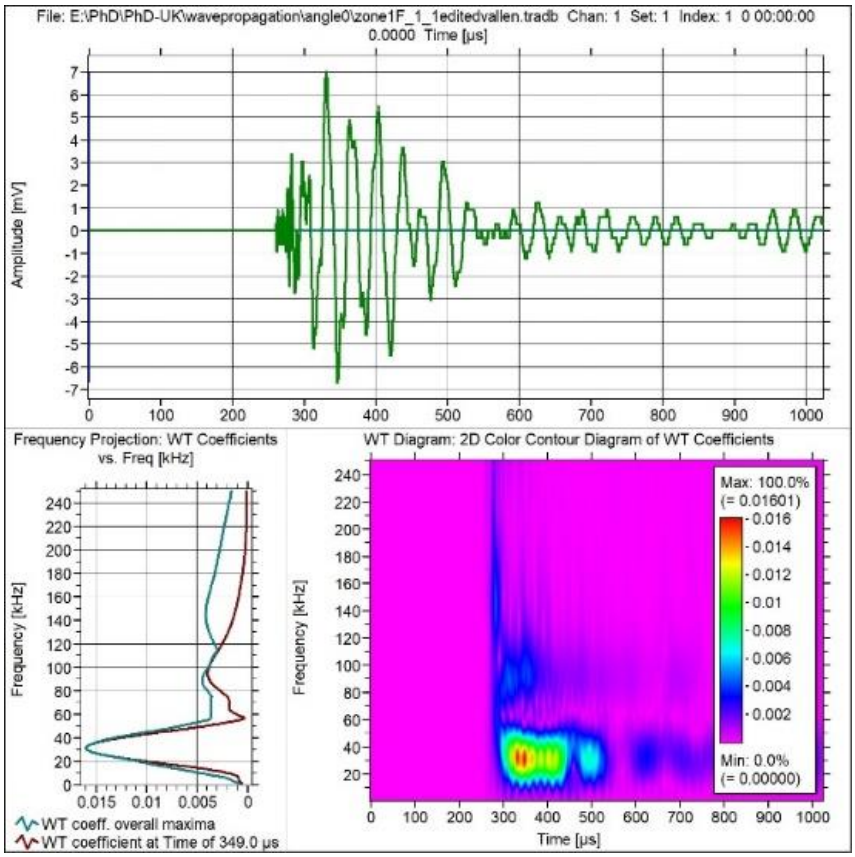

Figure 3- 26. Wavelet transformation in free glass fibre plate.

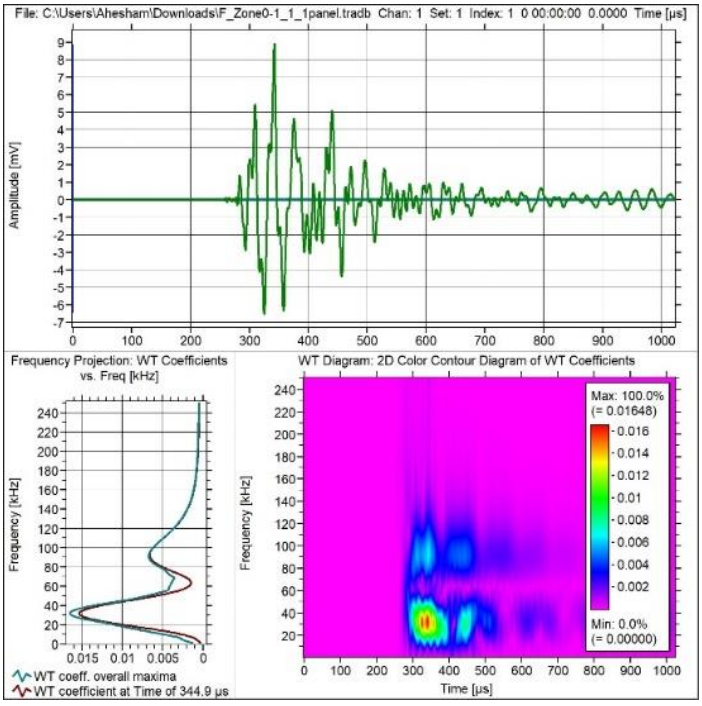

Figure 3- 27. Wavelet transformation in top plate of the HSP.

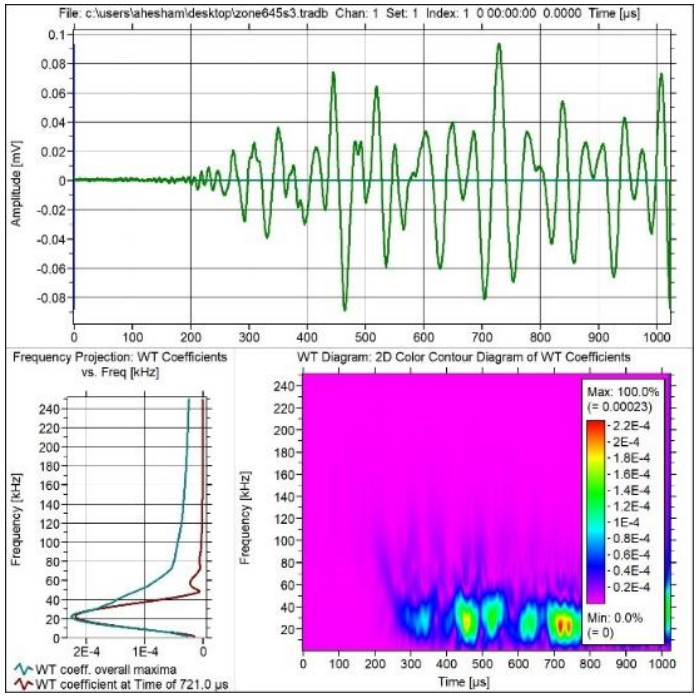

Figure 3- 28. Wavelet transformation in bottom plate of the HSP.

The wavelet transformations show that frequencies between 30 kHz to 130 kHz are active in both. The average low frequency wave component of 30 kHz and high frequency component at 90 kHz are dominant in free GFLP and top plate of the HSP. This shows that a Lamb wave could found in both GFLP and the top plate of the HSP. The waveform in the bottom plate is biased to the A_o frequency with continuously pulsing from top plate H-N sources which interrupt the Lamb wave propagation and cause the S_o mode significant attenuation.

3.6. Laser Vibrometer Method

A Broadband PZT (AGU Vallen-VS-900-M) with a non-integrated pre-amplifier and 100 – 900 kHz response range is placed in the centre of the GFLP. A 5-cycle sinusoidal burst from a function generator (WaveStation 2012) with peak-to-peak voltage 3 V_{pp} and amplified by ×100 by amplifier (Model 7500 amplifier-Krohn-Hite, Ltd) and is input as a reference signal to the PZT at different frequencies (50-350) KHz to find out the critical frequency at which the S_o and A_o separation can be achieved. A 3D-LVS (Polytec-PSV-500) is used for scanning the velocity field, as shown in Figure 3-29. Sampling frequency is 2560 kHz, satisfying the Nyquist–Shannon sampling theorem to obtain a good reconstruction of the signals. The number of scanning points is in each direction, with 1200 times for averaging taken at each point and averaged to improve the signal-to-noise ratio.

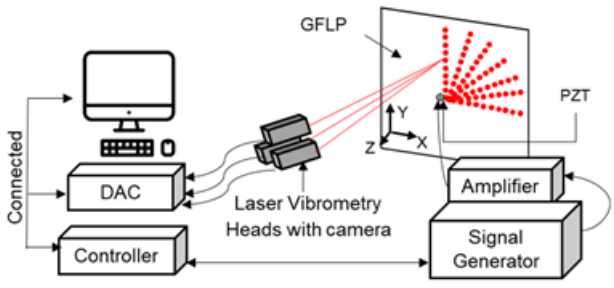

Figure 3- 29. Schematic drawing of Laser vibrometry scanning of GFLP.

The Scanning Laser Vibrometry setup used for the HSP is similar to that used for the GFLP, but as the honeycomb core increased the in-plane and out-of-plane stiffness, the PZT (AGU Vallen-VS-900-M) is replaced with (MGL -R6- transducer) with a lower frequency range (35-100) kHz.

This is attached to the front surface of the panel to study wave propagation at 80 KHz as the critical frequency and the back surface at 40 kHz to analyse the waveforms on the front plate resulting from the energy transmitted from back plate to front plate through the honeycomb cells. The number of scanning points in each direction is 175, with 1500 measurements taken at each point and averaged to improve the signal-to-noise ratio.

In order to analyse the wave propagation in the glass fibre laminated plate and the honeycomb sandwich panel in more details, a Polytec PSV-500-3D-M scanning laser vibrometer is used. Figure 3-30 shows the Polytec PSV-500-3D-M system.

Figure 3- 30. PSV-500-3D-M system.

The scanning laser vibrometer PSV-500-3D-M system measures the velocity field of the scanned point using three laser heads and the HD

camera is used for more spatial resolution. The conceptual design of the laser vibrometry scanning system is shown in Figure 3-31.

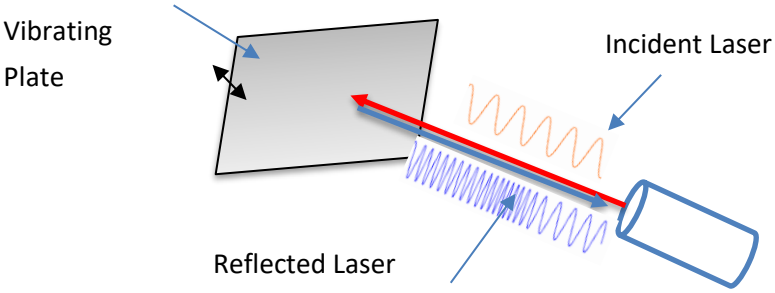

Figure 3- 31. Conceptual drawing of the laser vibrometry method.

To increase the accuracy of the reflected signal, the area of interest should be covered with glass beads fixed by adhesion spray. Due to the vibratory motion of the plate under examination, the velocity is derived from the change in phase of the reflected light. Figure 3-32 presents the function generator and amplifier.

Figure 3- 32. Function generator above the amplifier.

3.6.1. GFLP

The waveforms presented in Figure 3-33 to Figure 3-35 show Lamb wave behaviour with average frequency components 93.19 kHz for S_o mode and 32.04 kHz for A_o mode in the 0º, 45º, and 90º. Since the laser vibrometry gives the amplitudes in velocity unit, the waveforms are integrated to obtain the displacement amplitude in meter.

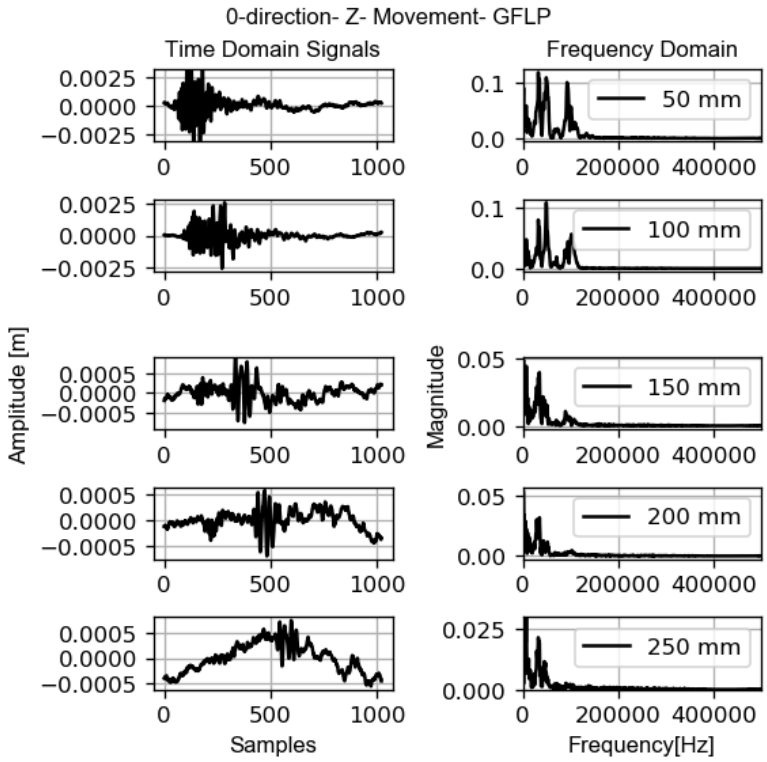

Figure 3- 33. Waveforms in time and frequency domains on 0o direction at 50, 100, 150, 200 and 250 mm.

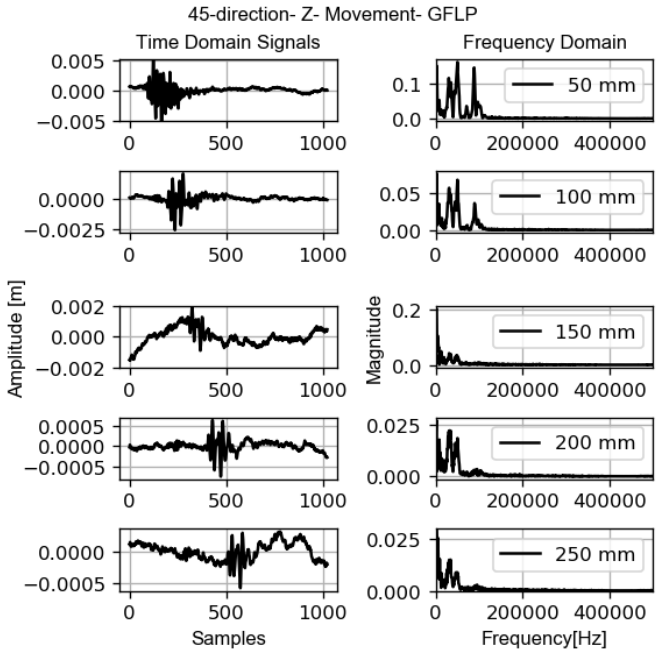

Figure 3- 34. Waveforms in time and frequency domains on 45° direction at 50, 100, 150, 200 and 250 mm.

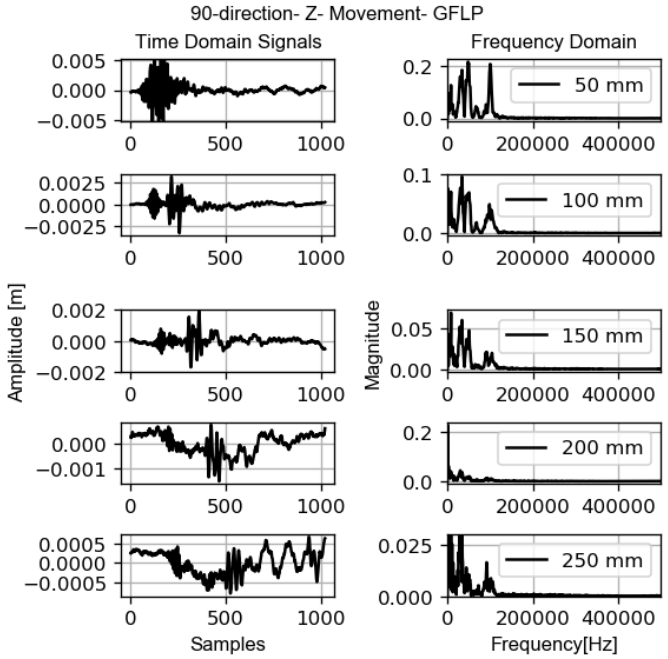

Figure 3- 35. Waveforms in time and frequency domains on 90° direction at 50, 100, 150, 200 and 250 mm.

Figure 3-36 demonstrates the Lamb wave field on the GFLP after processing the results in the Polytech software.

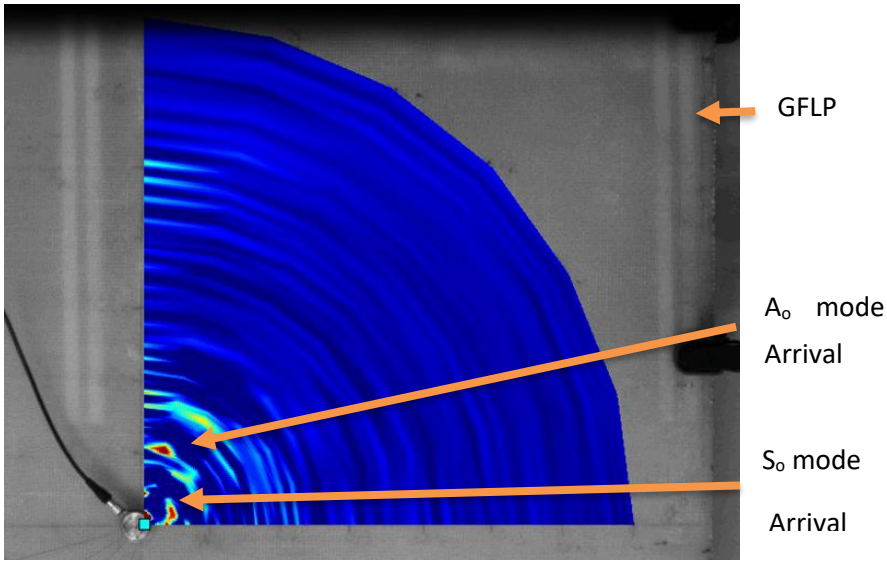

Figure 3- 36. Lamb wave field scanning by the LVS.

3.6.2. Sandwich Panel

On the HSP, out-of-plane velocity scanning on the front plate containing the PZT showed average dominant frequency at 25 kHz.

Figure 3-37 presents the waveforms on the front plate with the exciting transducer on the front plate. The flexural component of the Lamb wave on the front plate can be seen with frequency at 25 kHz. The in-plane motions (e.g. scanning velocity in x and y directions) are investigated to detect whether low amplitude S_o exists or not. However, S_o is not detected and extremely diminished. Unfortunately, due to the experimental setup, the transducer in the back side of the HSP is not able to inject sufficient energy into the HSP for AE to be recorded by the vibrometer on the reverse side. This is in contrast to the results in Section 3.4, showing that the energy of the H-N source exceeded that of the piezo actuator used in the vibrometer study. This raises further concerns about

ability of AE to monitor through thickness damage in HSP structures, as the attenuation is so great that smaller signals which could be indicative of damage may not be detected by sensors if they are on the opposing plate, even for very small propagation distances.

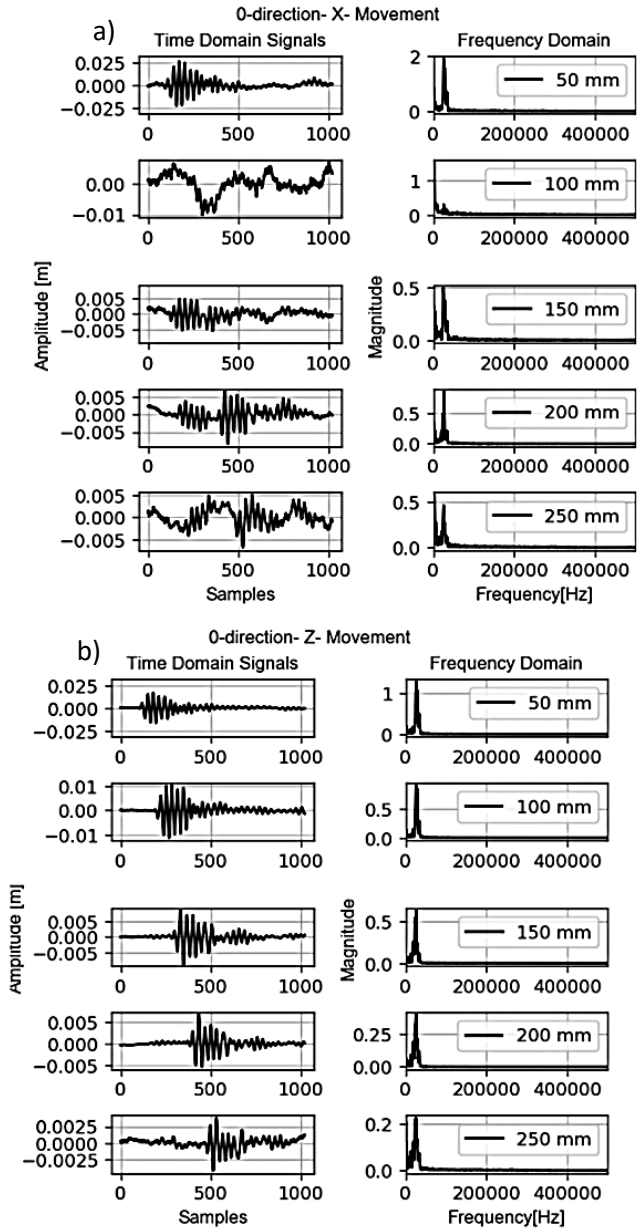

Figure 3- 37. Scanning results in different distances at direction 0° on top plate in a) X-direction and Z-direction where PZT transducer is on front plate.

Figure 3-38 presents the setup for exciting Lamb wave through energy transmission from the back PZT transducer.

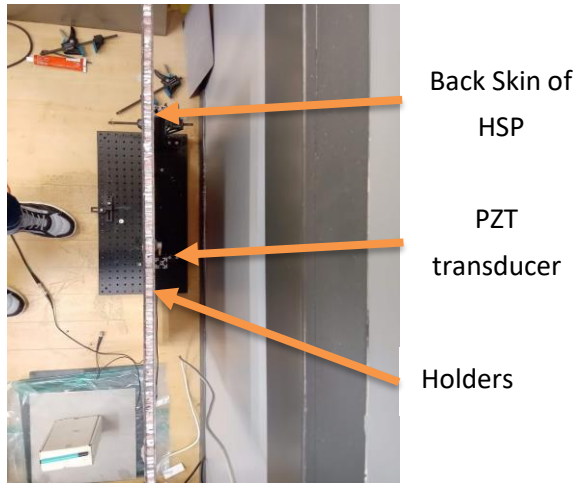

Figure 3- 38. Lamb wave generation by transducer on the back surface of HSP.

As demonstrated in Figure 3-39, it is found that the PZT transducer is not capable for exciting the Lamb waves by energy transmission from back surface to the front one.

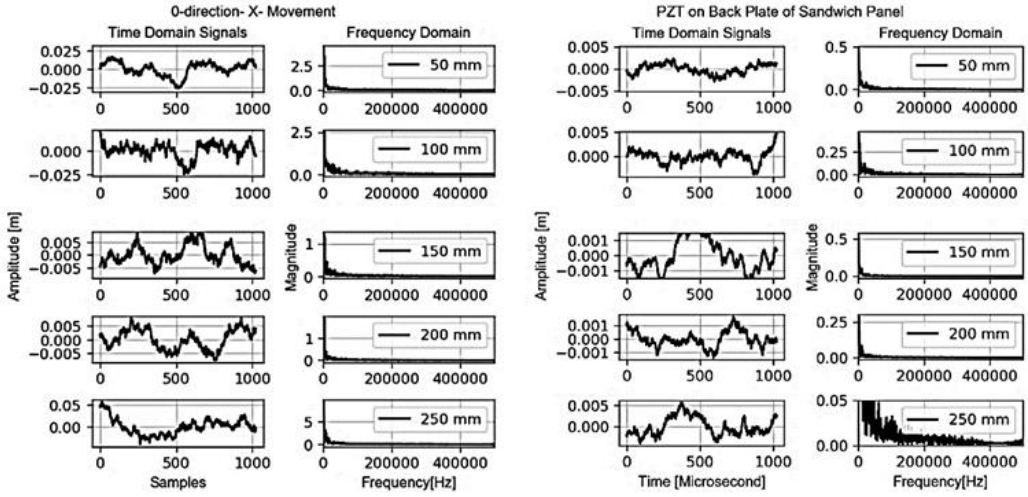

Figure 3- 39. Scanning results in different distances at direction 0° where PZT transducer is on back plate.

3.7. Frequency Response Modelling

The finite element model developed in Chapter 2 is investigated under harmonic analysis in CalculiX. For excitation of frequency range from 500 Hz to 26 KHz, the displacements of two opposite nodes (e.g. node on top surface of HSP and another one opposite to it on bottom surface) are examined and compared to each. Figure 3-40 presents line diagram of both nodes' displacements.

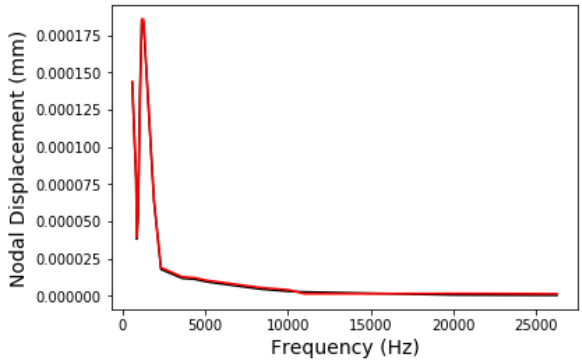

Figure 3- 40. A comparison between two opposite nodes on the HSP numerical model.

Figure 3-41(a-b) demonstrate the difficulty of obtaining Lamb waves through this model. The displacements of both nodes do not experience different values resulted from the honeycomb layer existence. The whole HSP acts as a unified body and both skins do not suffer from different wave propagation. Furthermore, the reason behind this behaviour is that CalculiX considers structural dynamics physics only which are invalid in this case. It is worth mentioning that the implementation of Lamb wave physics in the finite element method is beyond the scope of this PhD study. The objective of investigating the frequency response analysis is to take the model to the edge to see where it stands.

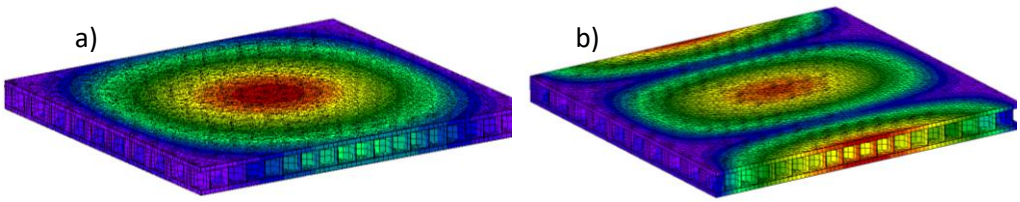

Figure 3- 41. Frequency response analysis of the HSP at a) 865 Hz and b)11,000Hz.

3.8. Summary

- The honeycomb cells are found to act as a conduit for AE energy, allowing signals to be recorded by a sensor on the surface opposite to that on which the H-N source is generated.
- AE propagates as Lamb waves in the GFLP and in the top and bottom surfaces of the HSP, despite the addition of the honeycomb layer. Further, in each of those three surfaces, the dominant frequencies for the S_o and A_o modes are 90 KHz and 30 KHz respectively.
- The velocity of the Lamb waves in the GFLP followed the conventional behaviour, with maximum S_o velocities of 4028 m/s and 4005 m/s occurring in the fibre directions, a minimum S_o velocity of 3472 m/s at 45^o to the fibre direction, and an average A_o velocity of 1323 m/s, independent of fibre direction. Interestingly, despite the addition of the honeycomb layer, which increases the out-of-plane stiffness of the HSP compared to the GFLP on a macro scale, the A_o velocity in the top surface of the HSP is found to be close to that in the GFLP, with an average value of 1290 m/s, also with no directional dependency.
- The S_o velocity in the top surface of the HSP, on the other hand, displays starkly different trends than those seen in the GFLP, with maximum velocities of 3927 m/s and 3893 m/s occurring in the 15^o and 75^o directions.
- The concept of the insertion loss is proposed to describe the loss of signal amplitude due to the addition of the honeycomb layer. For the 0^o direction the insertion loss of the S_o and A_o modes is found to be approximately constant with distance, with average losses of 18 dB and 3 dB, respectively.

- The A_o attenuation in the top surface of the HSP is similar to that in the GFLP in most directions.
- The S_o attenuation in the top plate of the HSP is lower than in the GFLP, likely owing to the interaction between the ribbon direction and the fibre direction.
- The AE transmits to the opposing surface of the HSP providing somewhat striking results. Firstly, in the specimens with a bespoke number of cells, it is found that the energy transmitted increased with the number of cells, but only up to a point; after the cells covered a large enough surface area of the HSP, the energy began to diminish, potentially due to energy being transmitting from the receiving surface back to the original surface.
- Whilst the propagation mechanism for AE in the receiving surface of the HSP is found to be Lamb waves, the S_o mode amplitude is severely diminished, barely visible above the noise.
- The LVS results confirm the travelling frequencies of the S_o and A_o wave modes in the GFLP and to surface of the HSP, however, it is not possible to supply sufficient energy into the HSP for signals to be recorded from the opposing surface, thus highlighting the challenges that could be faced when monitoring structures for damage using AE sensors bonded to one side of an HSP.

Chapter 4: AE Source Location study

4.1. Introduction

This chapter investigates different strategies to locate the artificial acoustical sources (e.g. H-N sources) on both plates of the HSP using AE method. The H-N sources are generated on both plates of the HSP while keeping the AE sensors affixed on one plate only. Traditional AE source location in commercial software includes using triangulation method with knowing difference in time of arrival (DTOA) of the AE signals and the AE wave velocity in the structure under investigation. Delta-T Mapping technique is also used to locate the H-N sources on both plates of panel.

4.2. AE Source Location

4.2.1. Specimen Preparation

The HSP consists of two GFLPs and a hexagonal honeycomb core bonded between them. The overall size of the HSP is 820 × 820 × 15 mms. The area of interest is the area where the H-N sources are generated upon. It is formed by placing the sensors whatsoever their number and hence, the area between these sensors becomes the area of interest. However, because of the attenuation characteristics of the HSP materials, the area of interest cannot be the full size of the HSP (i.e. 820 × 820 mms). Therefore, the area of interest has been designed by placing four sensors to form four asymmetric corners of a rectangular shape with approximate size 320 × 320 mms. The maximum diagonal distance between a pair of sensors (e.g. S_1 and S_3) is 510 mm to capture the AE signal before being severely attenuated. The sensors' locations in (X, Y) plane are as following; S_1 (230, 230), S_2 (560, 245), S_3 (585, 595), and S_4 (220, 580) in mm as shown in Figure 4-1. The locations of the sixteen artificial AE defects are marked on the front and back plates of the HSP using white corrector pen to assure

repeatability and reproducibility. Note that after reversing the HSP, the sensor positions change according to the measurement origin.

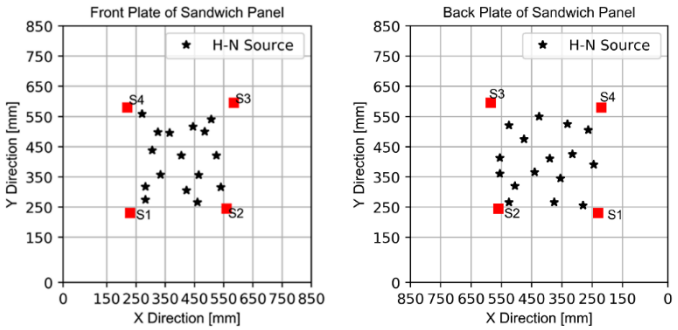

Figure 4- 1. Sensors and artificial defects' locations on front and back plates.

Table 4-1 provides the X-Y locations of the marked locations for front and back plates.

Table 4-1. The locations of the artificial H-N sources.

Source ID	X_{front}	Y_{front}	X_{back}	Y_{back}
1	28.2	27.45	24.5	39.0
2	28.2	31.7	26.3	50.5
3	27.1	55.8	28.0	25.5
4	30.5	43.8	31.5	42.5
5	32.5	49.8	33.2	52.5
6	33.4	35.7	35.5	34.5
7	36.5	49.5	37.5	26.5
8	40.5	42	39.0	41.0
9	42.3	30.5	42.5	55.0
10	44.5	51.6	44.0	36.5
11	46	26.5	47.5	47.5
12	46.5	35.6	50.5	32.0
13	48.5	50	52.5	52.0
14	50.7	54	52.5	26.5
15	52.5	42	55.5	41.3
16	54	31.5	55.5	36

4.2.2. AE Delta-T Mapping Method

Delta-T mapping setup is shown in figure 4-2 and experimental setup shown in Figure 4-3 and Figure 4-4. The implemented Delta-T mapping methodology includes the following necessary steps:

1. Specifying the area of interest that satisfy the following requirement:
    - The events' signals can be detected before being attenuated greatly; therefore, the largest area of interest before large attenuations to happen is 300×300 mm.
2. Drawing the grid system on the HSP with resolution 20 × 20 mm which yields 16×16 lines and 256 nodes.
    - This resolution is higher than signal wavelength.
3. Locating the four WD sensors in asymmetric manner to provide irregular sensor array.
    - It should be noted that a minimum of three sensors is required to localise the events accurately.
4. Inducing artificial AE events at each node, five times for averaging later to minimise error. Therefore, DTOA data can be obtained with less error.
5. Computing the DTOA for each pair of sensors with the aid of Akaike Information Criterion (AIC) [25], [26], [41] to ensure that the effective signal.
    - Therefore, Delta-T maps can be constructed.
6. These maps are used to compare measured events data to locate an actual AE event.

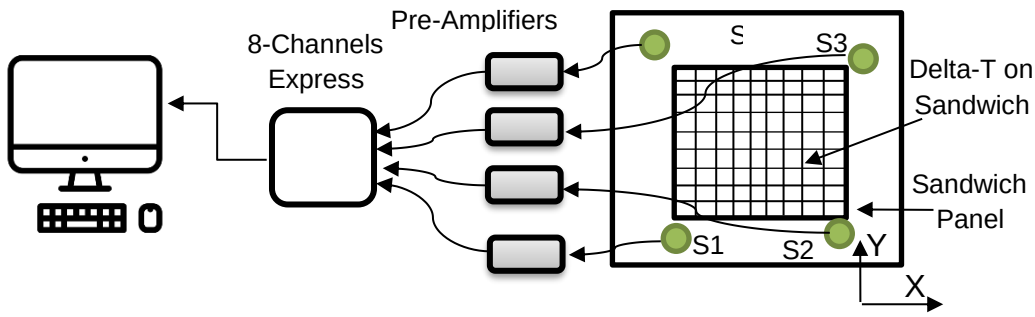

Figure 4- 2. Schematic drawing of test setup of AE source localisation using Delta-T mapping.

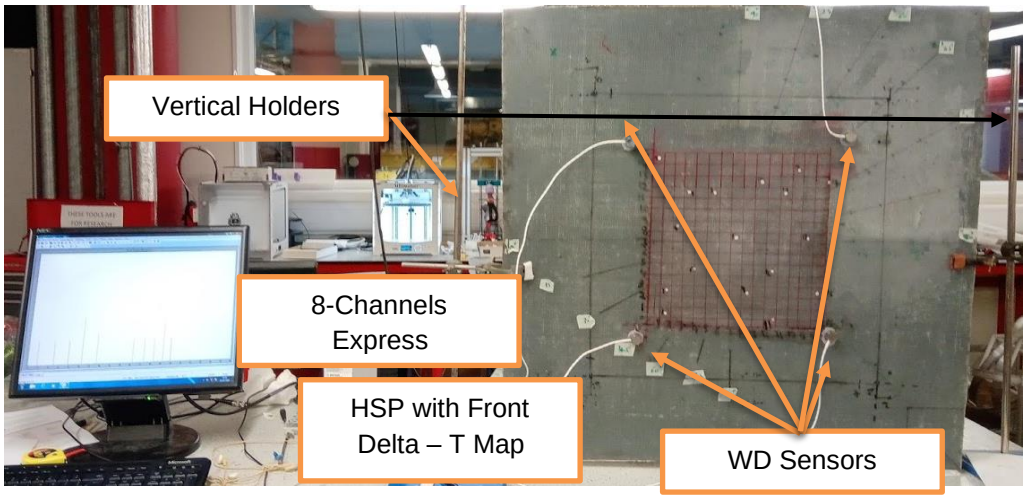

Figure 4- 3. Experimental setup of AE source localisation using Delta-T mapping on front plate.

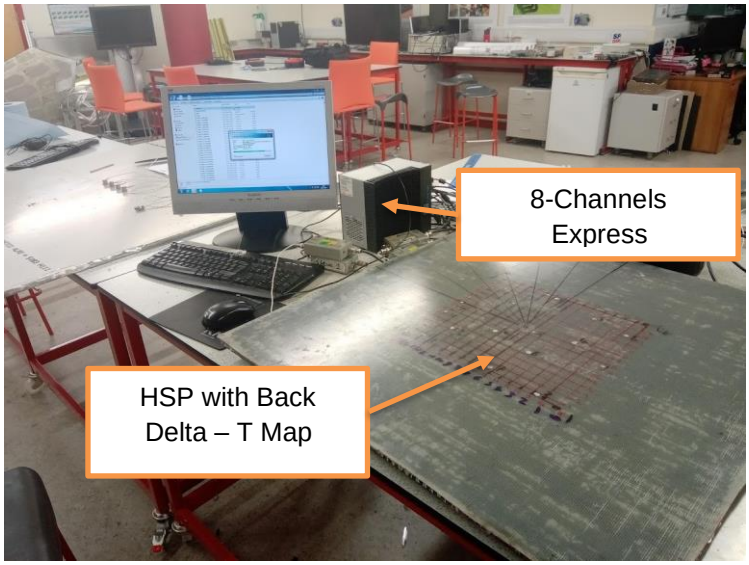

Figure 4- 4. Experimental setup of AE source localisation using Delta-T mapping on back plate.

The maps are created on the front plate and on the back plate, identically. To assure that both maps are identical, two elastic wires are used perpendicularly on each other, and their intersection represents the corner position of each map. This has been done to obtain the four corners of the back Delta-T map. Figure 4-5(a-b) shows time grid on the front and back plates between sensors 1 and 3.

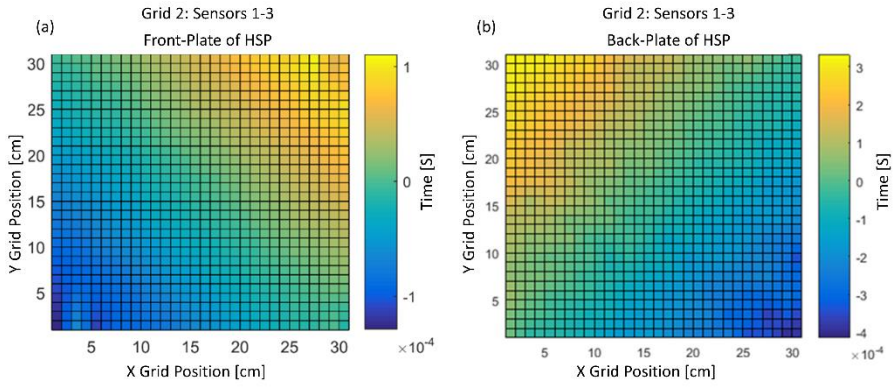

Figure 4- 5. Example of Time Grid between sensor 1 and sensor 3 on, a) front plate, and b) back plate.

4.3. Location Study Results

4.3.1. Difference in Time of Arrival Method

The average velocity is 3736.25 m/s for the AE wave on the front plate and 1261 m/s for the transmitted wave from front plate to back plate. Figure 4-6(a) shows the actual locations of sources as black stars, and the measured sources by the DTOA method as blue on the front plate. For each actual location, a circle has been drawn to include the actual source location and the measured artificial sources. The red circles represent large deviation between them. Figure 4-6(b) shows the measured sources for the back plate using DTOA technique. It is notable that the error becomes higher for the AE sources in the back plate. The total average Euclidean location error (AELE) is 20.2 mm for defect on front plate and 42.8 mm for the defect on the back plate.

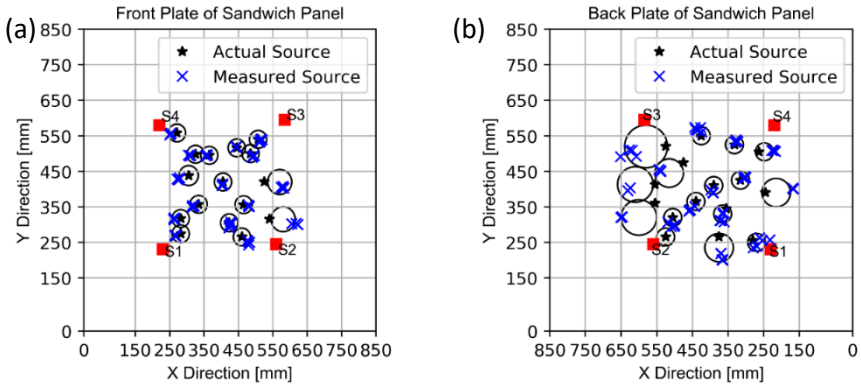

Figure 4- 6. AE source's locations and detected locations using DTOA (a) front plate, and (b) back plate.

4.3.2. Delta-T Mapping Method

Figure 4-7(a) and Figure 4-7(b) show the Delta-T mapping results in blue and the defects' actual locations in black in front and back plates, respectively. The total AELE is 11.1 mm for defect on front plate and 20.78 mm for the defect on the back plate.

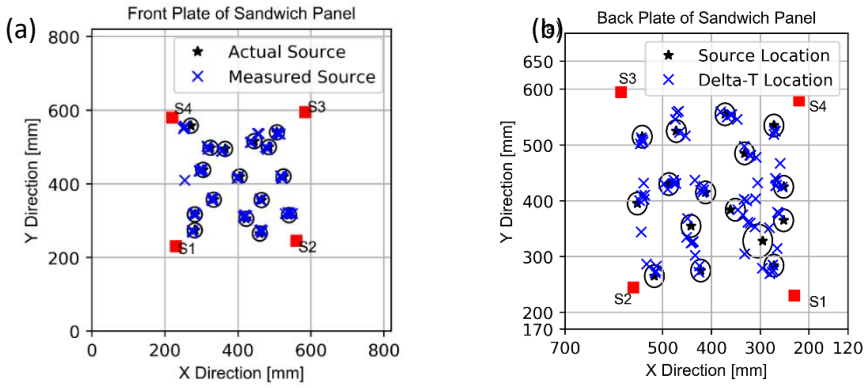

Figure 4- 7. H-N sources locations and detected locations using Delta- T Mapping (a) front plate, and (b) back plate.

Figure 4-8(a-b) present the bar charts of the AELE of each AE source on front and back plates using DTOA and Delta- T mapping methods. Overall, AELE is higher in case of DTOA.

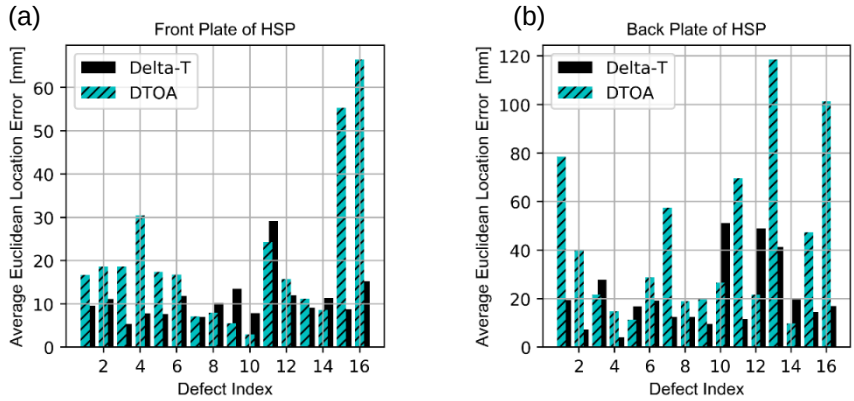

Figure 4- 8. Average error comparison between DTOA and Delta-T mapping for (a) Front plate and (b) Back plate.

For the front plate case, the highest AELE is 66.5 mm using DTOA method while the highest AELE using Delta- T mapping is 29.1 mm which is approximately half than that of DTOA method. In case of AE on the back plate, the highest AELE is 118 mm for DTOA method and 51 mm in case of Delta- T mapping.

4.4. Summary

This chapter provides a comprehensive investigation of using two different AE source locating methods, DTOA and Delta-T Mapping on the HSP.

- Delta-T Mapping location technique is demonstrated to be significantly more accurate at locating sources on the complex honeycomb sandwich structures compared to DTOA technique.
- Overall, the AE source location error by Delta-T Mapping is half that of the difference in time of arrival.
- Delta-T Mapping is extended to detect the out-of-plane sources while the sensors are kept mounted on the opposite plane. It is demonstrated the credibility of using the Delta-T Mapping not only to detect the planer sources but also the out-of-plane one.

Chapter 5: HSP specimen Testing

5.1. Introduction

This chapter presents the damage assessment on the HSP specimen under 3 point-bending test using AE technique.

The specimen size is 200 x 150 x 20 mm. It is designed and tested according to ASTM C365/C365M – 16. The Delta-T Mapping is utilised

5.2. Bending test

5.2.1. Delta- T Map Preparation

The first step is collecting and computing the training data for the Delta-T map drawn on the top plate of the HSP. The AE setup consists of four wideband, MISTRAS Group, Ltd (MGL), WD sensors (100 – 1000 kHz) which are bonded on the top plate of the HSP using silicone to provide a good acoustic coupling and then left for curing at room temperature. The acquisition system is MGL's eight channels Express. The AE timing parameters are selected by trial and error to find out the suitable values. They are 100, 200, and 400 µs for the PDT, HDT and HLT, respectively. The sensors are connected to MGL's Preamplifiers with a gain selected to 40 dB and frequency range 20 KHz to 1200 KHz. The threshold level is 40 dB to eliminate the electrical and background noise coming from the bending machine and the sampling rate is 5 MHz. The overall dimensions of the Delta-T map are 110 × 110 mm with 10 mm interval. At each node in this training map, the artificial AE sources using pencil lead breakage concept are generated five times to obtain the average in the post-processing to minimise the errors. After recording the AE signals, the time of arrival of these signals are obtained and the difference of time of arrival for each pair of sensors is calculated. The experimental setup is presented in Figure 5-1.

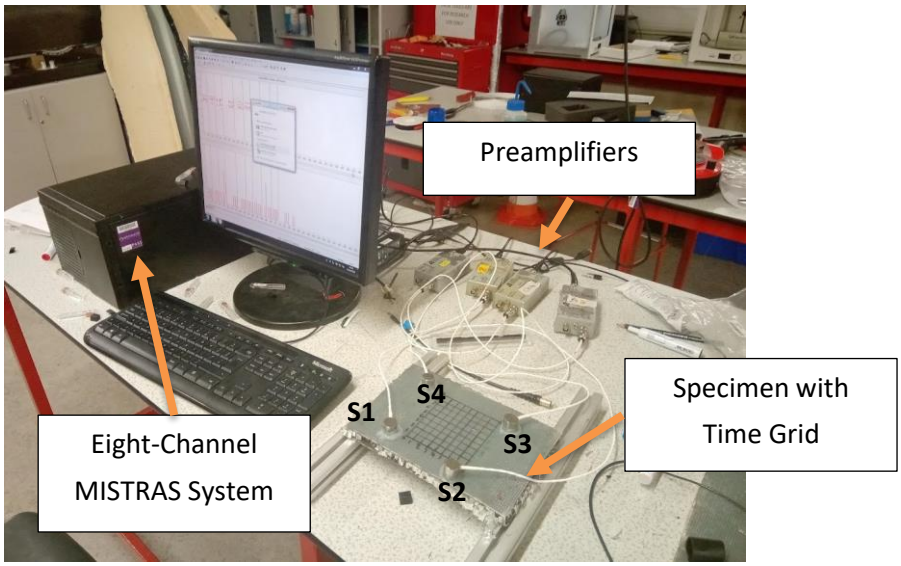

Figure 5- 1. Delta-T map construction and generation.

Figure 5-2 shows an example of a time grid showing the difference in the time of arrival between sensors 1 and 3 for a signal originating from any point in the map.

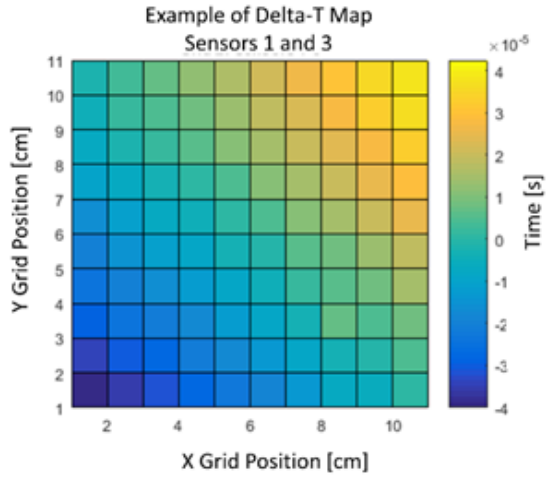

Figure 5- 2. Example of Delta-T map between sensor 1 and sensor 3.

It is worth mentioning that the Delta-T map is drawn on the top plate only since the significant damage level has appeared on that plate during

the initial tests of the HSP specimens. Inevitably, these time maps cannot locate the AE sources originating from the bottom plate of the HSP, because there is a considerable timing difference for these sources and significant large attenuation for the AE hits as concluded before.

5.3. Three-Point Bending Test

In order to assess the bending stiffness of the proposed honeycomb sandwich structure, a three-point bending test (3PBT) is carried out in accordance to ASTM C393/C393M-06 standard [70]. As mentioned, the specimen size is 200×150×15 mm, and the testing machine is Servocon, Ltd., with capacity of 100 KN. Figure 5-3 shows a photo of the 3PBT setup.

The AE acquisition setup is same as implemented during the Delta-T Mapping preparation; the only addition is recording the parametric data of the load cell of the machine, to correlate the AE sources with test load.

Figure 5- 3. The three-point bending testing with acoustic emission.

Loading is conducted in three phases. Phase 1 consisted of displacement between 0 mm to 2.5 mm and represents the elastic range

of the HSP. Phase 2 consisted of displacement from 2.5 mm to 10.5 mm, and Phase 3 consisted of displacement from 10.5 mm to 33 mm. Between each phase, loading is paused, and the specimen is inspected visually for any significant macro damage.

5.4. Results and Discussion

5.4.1. Scanning Electron Microscope SEM

After the 3PB test, the Specimen is analysed using a scanning electron microscope to identify the damage mechanisms. The specimen is sectioned at the defective region. The section is taken then finished by grinding with wet silicon carbide paper, cleaning by acetone, and finally coated by gold coating to obtain high quality micrographs. The SEM type is (FEI/Philips XL30 FEG ESEM). The Micrographs are taken under high vacuum using a 7 µm aperture with a working distance of 10.1 mm between the specimen and the aperture. The examination of the defects on the top plate revealed that the effect of local crushing is causing fibre breakage, pull-out and matrix cracking as shown in Figure 5-4.

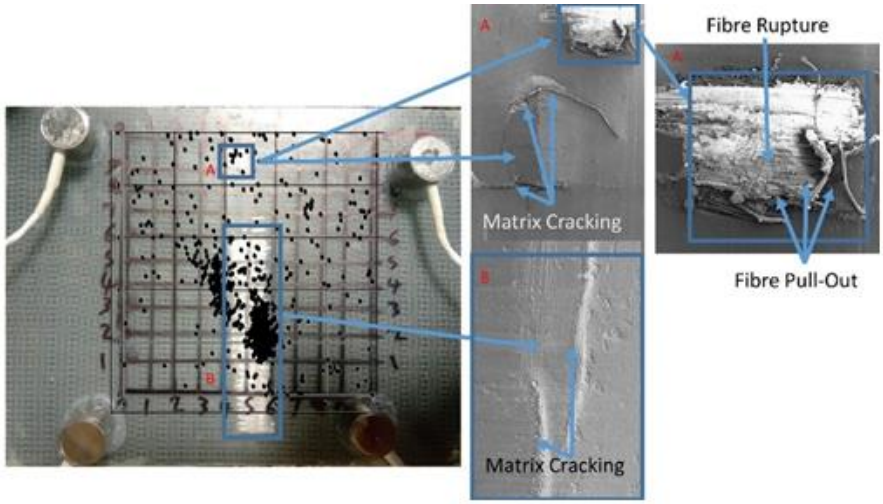

Figure 5- 4. SEM results of the locally crushed regions.

5.4.2. AE Located Sources and Energy

A preliminary location trial is conducted by generating H-N sources at three pseudo random locations in the grid. These are processed using the Delta-T maps created, and the position is located with error of ±5 mm.

This can be deemed to be the maximum accuracy achievable within this experiment and would appear to be sufficient to locate damage within the specimen. Although the Delta-T is commonly implemented on thin uniform plate, it is proved to be useful in locating the defects on a complex plate-like sandwich panel. Figure 5-5 shows the AE damage sources mapped on the HSP surface on the left-hand side and the AE sources with its energy on the right colour bar. The fibre rupture and pull-out in region A in Figure 5-4 on the SEM micrographs are in line with the high energy events shown in the same region in the right side of Figure 5-5. Epoxy matrix cracking is dominant as found by SEM micrographs in regions A and B of Figure 5-4 as its stiffness is quite lower than the fibre; this is supported by the abundance of lower energy events, as it is believed that fibre breakage is capable of generating higher energy AE because of its high stiffness compared to the polymer matrix [77].

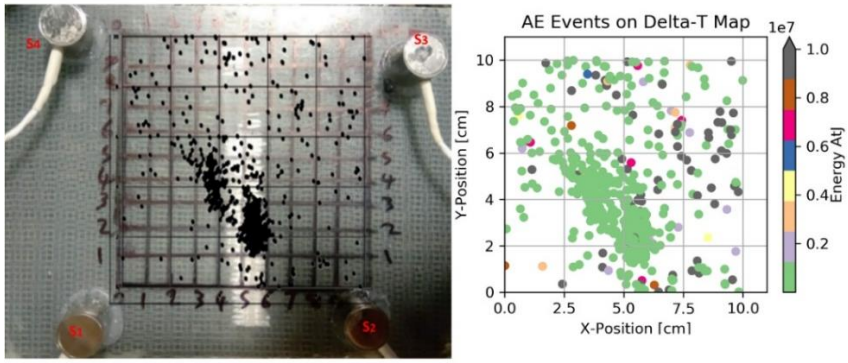

Figure 5- 5. Damage sources as detected by the Delta-T mapping; left: on the specimen and right: the energy associated with each source.

Figure 5-6 shows the located AE sources within each phase of the three testing phases. In phase 1, five, seemingly insignificant, AE sources are detected; in phase 2, 63 AE sources are located; and in phase 3, 655 AE sources are located. The AE located in phase 3 predominantly originated from the regions of visible damage on the top plate of the HSP.

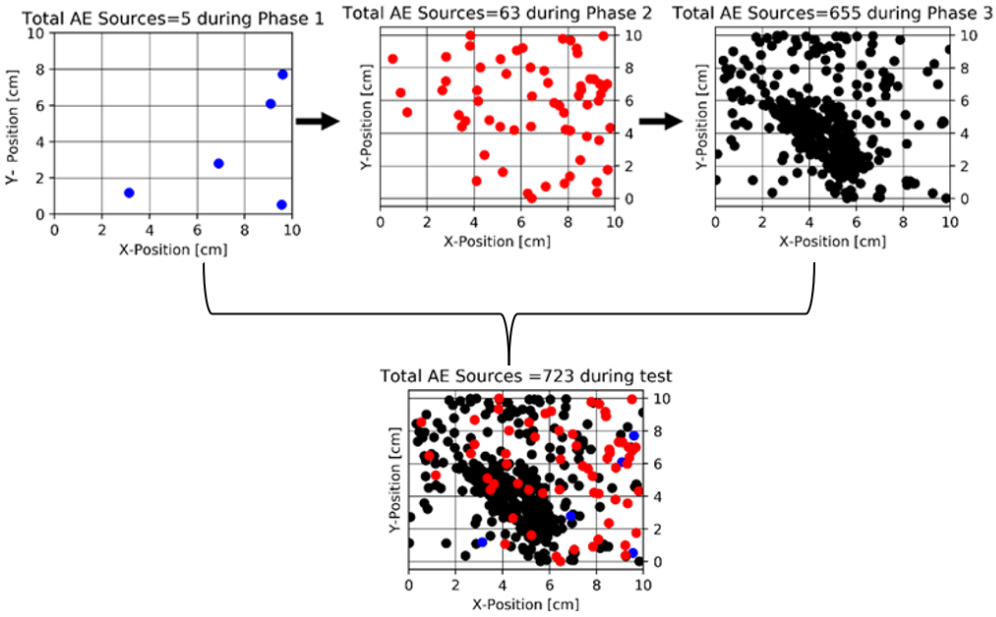

Figure 5- 6. Sequence of AE sources detected per each testing phase.

Figure 5-7 presents the load-displacement line graph along side the cumulative energy of the located AE hits, for each testing phase, detected by channel 1 (e.g. sensor 1). It is worth mentioning that the other 3 sensors provide similar patterns. As aforementioned, sensor 1 is positioned at the lower left corner of the time grid as shown before in Figure 5-5.

The specimen is mounted on steel cylinders of 30 mm diameter. As a result of applying force at the mid-point, the specimen slipped very slightly, generating some AE sources and causing a sudden fall in the load-displacement curve, as pointed out in the green rectangle in Figure 5-7.

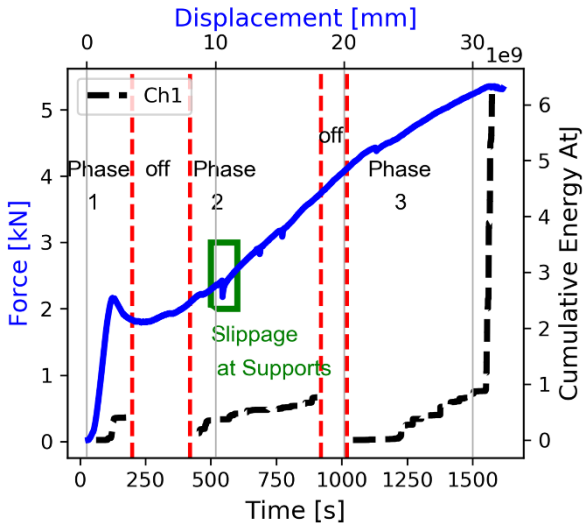

Figure 5- 7. Curves of specific cumulative energy in black and load-displacement in blue.

The cumulative energy in phase 3 is quite greater than the other two phases which is in line with the visible damage progression as the visual inspection revealed that significant damage appeared during phase 3. Figure 5-7 shows that the rise in the cumulative energy is rapid during this phase, more so than in phase 1 and 2; thus, AE is successfully detecting damage accumulation in the specimen.

5.4.3. Frequency Analysis

It is possible for the frequency spectrum of recorded AE to give insight to the nature of the source mechanism. First of all, the waveforms and their corresponding Fast Fourier Transform (FFT) of some pencil lead breakage events generated during the Delta-T Map construction of training data, are examined as shown in Figure 5-8. As established before, AE wave propagates as Lamb waves in the outer skin layers of the HSP. The average symmetric mode S_o frequency is centered at 93 kHz while the average antisymmetric mode A_o is 28 kHz. It is expected that AE sources

arising during testing would propagate in the form of Lamb waves of these distinguished modes, similar to signals of the pencil lead breakage.

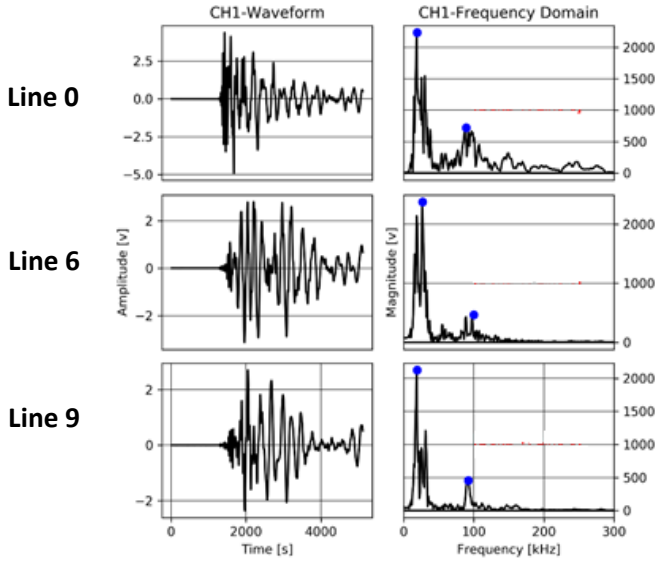

Figure 5- 8. Waveforms and FFTs of H-N events at line 0, 6 and 9.

The AE sources during phase 1 are Lamb waves with frequencies centered at 28 KHz and 90 KHz for A_o and S_o as shown in Figure 5-9. These sources are not corresponding to significant damage progression and can be attributed to the test noise.

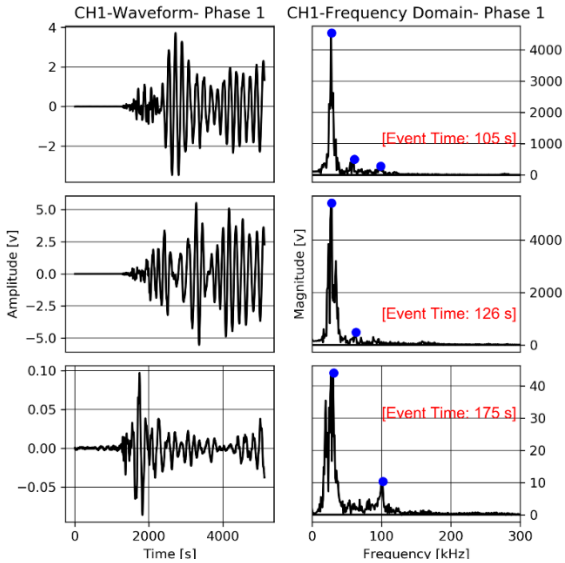

Figure 5- 9. Waveforms and FFTs for some events in phase 1.

In phase 2, some higher frequencies started to propagate, especially near 3 KN at time 900 second of the test, as demonstrated in Figure 5-10. However, no significant damage is visible to the eye during the loading stoppage and visual inspection.

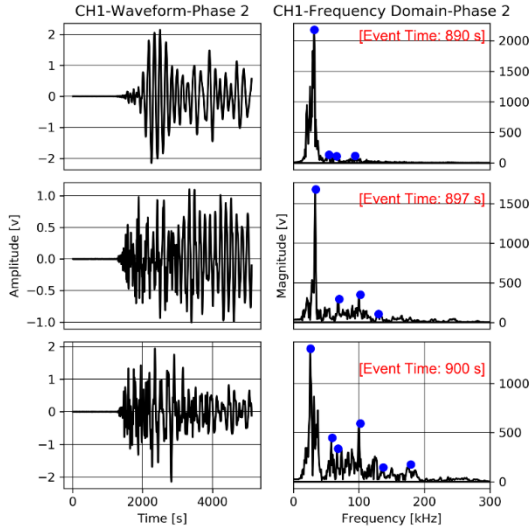

Figure 5- 10. Waveforms and FFTs for some events in phase 2.

In phase 3, more higher frequencies are propagating as in Figure 5-11. Furthermore, the damage becomes superficial and significant.

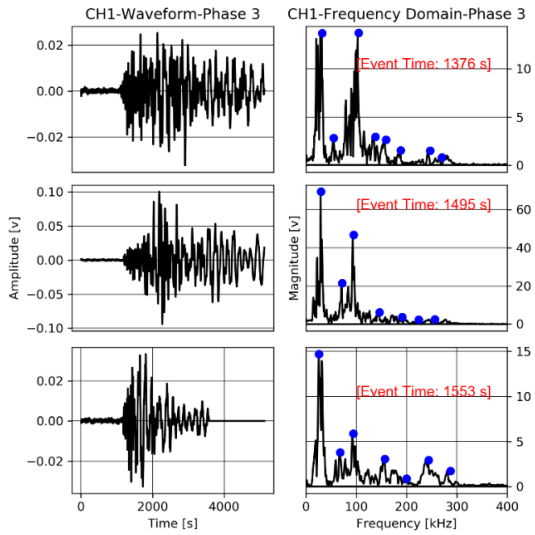

Figure 5- 11. Waveforms and FFTs for some events in phase 3.

Figure 5-12 demonstrates example of the frequencies' progression of the different AE hits as detected in each loading phase. The frequency components are increasing significantly in the third phase.

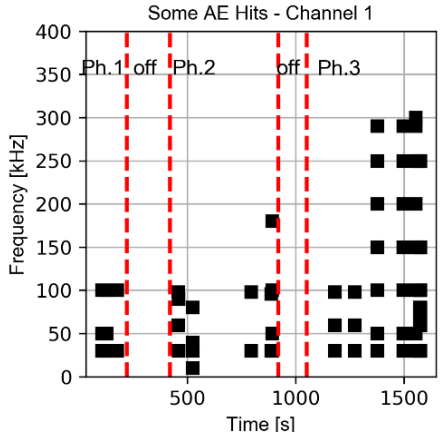

Figure 5- 12. AE frequencies development of some hits during testing time as detected by channel 1 in each loading phase.

In phase 1, the five AE events showed a Lamb wave propagation just similar to the pencil lead breakage signals. These sources are insignificant due to the fact that the load is in the elastic region of the HSP. In phase 2, the low frequency components, less than 100 kHz, are dominant. This indicates that microcracks are developing within the matrix but are not in significant damage level as during the visual damage did not appear superficially. However, by the end of the phase 2 at time 900 second (i.e. 3.7 KN), higher frequency components started to appear in the AE signal. The higher frequency components appeared at phase 3 as the load increased and the damage progression became visible. Comparing these results with the work of [52]–[55],who tested on comparable fibre glass polymeric composites experiencing similar damage mechanisms and based on the SEM micrographs, it is reasonable to make a connection between the different frequency bands and the damage mechanism. The frequency spectra of the AE events in the third phase contain higher frequency components than the first and second phases. The higher frequencies in the range of (157-322) kHz is likely associated with the fibre rupture, pull-out, and fibre-matrix debonding. The low frequency components in the range (30-105) kHz can be considered for the matrix cracking. The stiffness of the specimen is observed to change greatly in the third phase. This reduction in stiffness could be attributed to the evolution of micro cracks in matrix damage to macro cracks, because of the local crushing on the glass fibre plate.

5.5. Summary

- A three-point bending test is performed on a glass fibre aluminium honeycomb sandwich panel, with acoustic monitoring.
- The inspection of the sandwich specimen after disassembling it reveals that the honeycomb core did not affect the interior surface of the glass fibre plates on top and bottom.
- It is expected that the honeycomb core would indent the interior surfaces of these plates at test load that is higher than 7 KN according to the previous preliminary tests.
- On such a complex material structure, the Delta-T Mapping is reliable and capable of detecting damage progression but in 2D.
- The significant damages appeared on the top glass fibre plate of the HSP in phase 3, and the frequency spectra revealed higher frequency components than in phases 1 and 2.
- As compared to the literature and as supported by scanning electron microscope examination of the microstructure of the local crushing damage, the lower frequency range (30-105) kHz is related to matrix cracking whereas the higher frequency range of (157-322) kHz is related to fibre damage modes (e.g. fibre-matrix debonding, fibre pull-out and rupture). Moreover, during this phase, the cumulative energy increased dramatically, indicating significant damage progression.
- Delta-T Mapping has been found to be a promising tool for locating damage on complex sandwich structures.

Chapter 6: Conceptual Blade Manufacturing

6.1. Introduction

This chapter presents the concepts of using the HSP in manufacturing of a Vertical Axis Wind Turbine VAWT blade of asymmetric aerofoil (i.e. NACA 8412) from the studied honeycomb sandwich structure, is investigated. The manufacturing process for the blade is vacuum assisted resin infusion. The first porotype is defective since the epoxy resin is trapped inside the aluminium honeycomb cells, round its right angle edges, and the vacuum pressure is under relief as a result of the counter reaction of the aluminium honeycomb on the top laminates. In the second prototype, the aluminium honeycomb is totally covered with a Nylon film to close all the cells, the edges are chamfered to eliminate epoxy resin blockage at the edges, and finally the vacuum pressure is introduced every hour until the resin started to become gel. The proposed manufacturing technique yields a proper wind turbine blade as the aforementioned problems have been avoided.

However, the infusion spiral tubes caused indentations on the glass fibre laminates as a result of introducing the vacuum pressure every hour. Overall, the vacuum assisted resin infusion of wind turbine blade of sandwich structure could be a promising and inexpensive method as a manufacturing technique. The rest of the chapter includes the following:

- Blade Manufacturing trials
- Manufacturing considerations

6.2. Blade Manufacturing Trials

The VAWT type is Darrieus and the blade's aerofoil is asymmetric of type NACA8412. It has high lift to drag ratio that helps in self-starting operation of the VAWT. The blade size is 900 mm and the maximum chord length 400mm. The blade is manufactured as two halves and after that both halves have been adhered together using (i.e. Permabond-ET538). Figure 6-1 presents the honeycomb placement on the bottom glass fibre laminates.

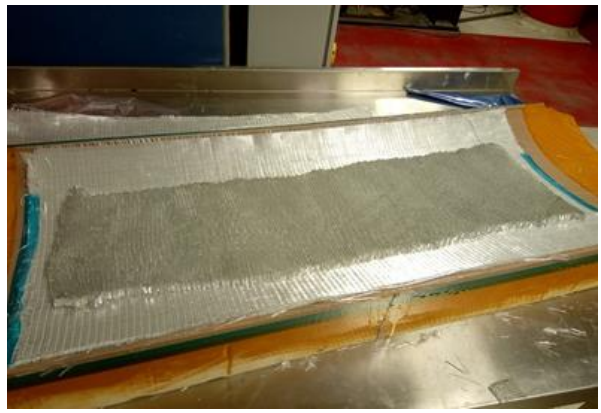

Figure 6- 1. Honeycomb placed on glass fibre laminates.

Figure 6-2 presents the vacuum assisted resin infusion process of the low-pressure side. Eight spiral tubes have been used, seven spiral tubes for the resin infusion tube are used for the vacuum. Each spiral tube has been pre-tensioned and placed on double mesh to obtain better resin flow and evenly distributed in the structure.

Figure 6- 2. Vacuum assisted resin infusion.

The leakage test has been carried out to inspect the quality of the sealing. In this test, the vacuum pressure drop in 5 minutes must be less than -5 mbar. The maximum vacuum pressure is -985 mbar. After epoxy resin infusion, the blade's halves have been left for curing at room temperature (e.g. 20^{o}C) for 48 hours. Figure 6-3 demonstrates the aerofoil after manufacturing

Figure 6- 3. The honeycomb inside the aerofoil surface.

By visual inspection, the following defects have been noticed in the first prototype:

- Epoxy resin ran out from the central region. The easier flow path for the resin is round this central region. Because the vacuum pressure is not equally distributed over the honeycomb core causing the middle

region to be highly under pressure whereas the sides are not under such pressure as shown in Figure 6-4.

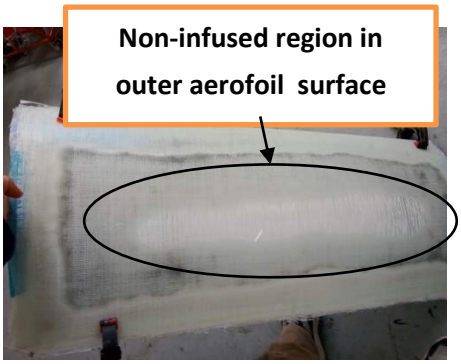

Figure 6- 4. The first defective prototype.

- Some epoxy resin is trapped near corners of the honeycomb because the honeycomb overall circumference is at right hand angle. This is reducing the flowability of the epoxy and inducing a blockage. This bulk region causes overall shortage in the steady infusion and increases the overall mass unnecessary. Also, these regions are local weak ones since there is no fibre reinforcement within. This defect is shown in Figure 6-5.

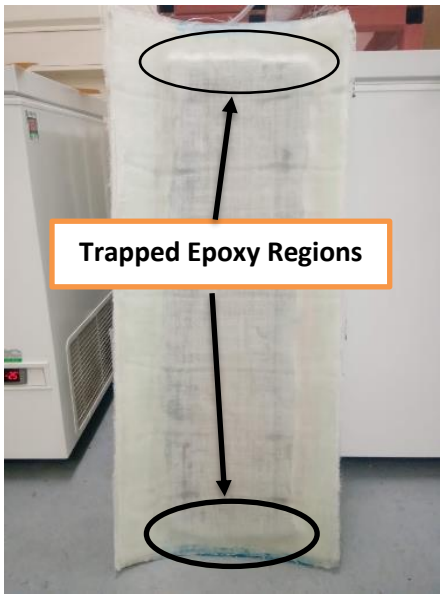

Figure 6- 5. Trapped epoxy regions defect.

These defects have been avoided in the second prototype manufacturing. The edges of the honeycomb are chamfered to allow a better resin flow and is totally covered using Nylon film to avoid resin trapping inside the cells as shown in Figure 6-6. Furthermore, the vacuum pressure is applied regularly every hour to make sure that the top laminates are pressing the honeycomb. This step stopped after 8 hours as the epoxy started to become gel.

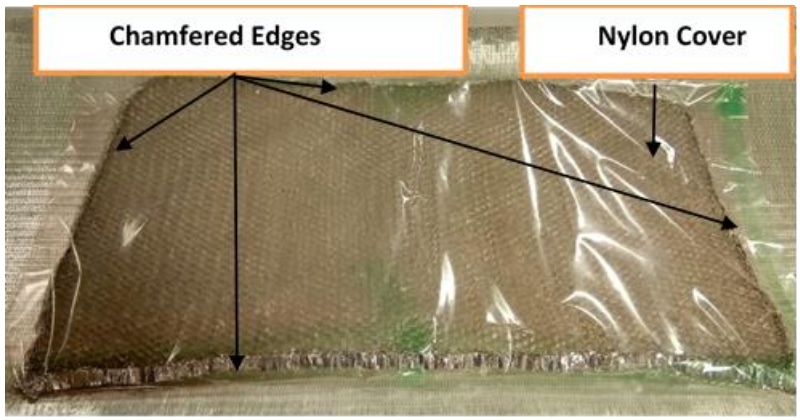

Figure 6- 6. Honeycomb core with chamfered edges inside.

The previous defects have been avoided and a fully resin infused blade is manufactured. However, because of applying the vacuum pressure every hour, the resin infusion spiral tubes traces occurred on the top laminates. To avoid this defect, it is recommended to add double meshes under each spiral tube.

To wrap it up, this chapter introduces the manufacturing process for a 900 mm long VAWT blade with 400 mm chord length by applying vacuum assisted resin infusion and curing in room temperature.

The first prototype is defective, and the main defects are lack of infusion in the resin infusion at the middle, resin blockage at the honeycomb right-hand edges, resin trapping in the honeycomb cells, and the counter-reaction of the honeycomb surface to the vacuum bag.

These defects have been resolved by covering the honeycomb core with sealed Nylon film to prevent resin trapping inside the cells, the vacuum pressure is applied every hour to make sure that the glass fibre laminates on the top of the aluminium honeycomb to hold it down until the epoxy started to become gel, and the honeycomb edges are chamfered to allow better resin flowability.

However, the surface of the low-pressure side of the blade prototype has indentations caused by the spiral resin infusion tubes because of applying the vacuum pressure every hour. This defect can be prevented by placing double meshes under each spiral tube, so they act as cushions and hence prevent the indentations.

Overall, the proposed manufacturing technique with the recommendations can be suitable for developing VAWT blades of cheaper cost since there is no need for using autoclaves or pre-pregs. However, it is recommended to use a bonding film instead of the Nylon film for better bonding.

6.3. Manufacturing Considerations

The successive trials presented in the previous section revealed the importance of some key considerations that are necessary to achieve proper manufacturing of the VAWT blade. These considerations include the following.

1. Covering the honeycomb core with sealed Nylon film to prevent resin trapping inside the cells.
2. Applying vacuum pressure at fixed intervals (every hour) to make sure that fibre glass laminates on top of the aluminium honeycomb have enough time to hold down the epoxy until it starts to become gel.
3. Chamfering the honeycomb edges to allow better resin flowability.

4. Placing double meshes under each spiral tube, so they act as cushions and hence prevent the indentations that may result on the low-pressure side from applying the vacuum pressure every hour.
5. Using a bonding film instead of the Nylon film for better bonding.

The proposed manufacturing technique with the aforementioned considerations can be suitable for developing VAWT blades of inexpensive cost since there is no need for using autoclaves or pre-pregs.

6.4. Summary

This chapter presents the manufacturing of a VAWT blade. Different defects are encountered. Methods and considerations to overcome these defects are proposed and finally the proposed manufacturing technique can be followed to manufacture wind turbine blades with HSP core.

Chapter 7: Conclusions and Future Work

This thesis presents the efforts that have been carried out in investigating the honeycomb composite structure for being implemented in wind turbine blades. It started by designing an optimum honeycomb sandwich structure then analysing the acoustic emission wave propagation in it then proposing a source location study then conducting bending test to assess the damage mechanisms in this material and finally manufacturing the wind turbine blade.

7.1. Conclusive Points

- Sequential quadratic programming is a robust optimisation technique for obtaining the honeycomb size parameters.
- The optimum structure has been tested under bending numerically and experimentally and good agreement for the results are achieved showing the potential of CalculiX program in analysing the behaviour of such complex material with reasonable time.
- The lamb waves are developed in the honeycomb sandwich panel on top and bottom plates but do not act as a unified wave through the whole thickness of the sandwich panel.
- As the number of the honeycomb cells increases as the So mode attenuates rapidly.
- However, the Lamb waves in the bottom plate of the HSP (the receiving side) are heavily A_o mode dominant, with severely attenuated S_o mode. This is thought to be due to the out-of-plane nature of the energy transfer from the honeycomb cells to the bottom surface.
- S_o velocity in the GFLP followed the conventional behaviour relying upon the fibre direction while the A_o velocity is independent of fibre direction.

- Interestingly, despite the addition of the honeycomb layer, which increases the out-of-plane stiffness of the HSP compared to the GFLP on a macro scale, the A_o velocity in the top surface of the HSP is found to be close to that in the GFLP.
- S_o velocity in the top surface of the HSP, on the other hand, displayed starkly different trends than those seen in the GFLP, with maximum velocities of 3927 m/s and 3893 m/s occurring in the 15^o and 75^o directions. It is hypothesised that this departure from the usual, fibre-direction-dependant velocity profile of the S_o mode is affected by the honeycomb layer, and that it is likely no coincidence that the 60^o difference in the directions of the maximum S_o velocities match the 60^o angle between the two ribbon directions in a hexagonal honeycomb lattice, which are the directions in which the honeycomb has its highest stiffness.
- The insertion loss concept is introduced to describe the loss of signal amplitude due to the addition of the honeycomb layer. It is proved to be a useful measure to understand the geometrical and material effects on the AE wave propagation. The S_o attenuation in the top plate of the HSP is influenced by the interaction between the ribbon direction and the fibre direction.
- The frequency response analysis of the HSP in the CalculiX does not generate Lamb waves propagation.
- The source location is investigated using time of arrival and the Delta-T Mapping and found that Delta-T mapping gives lower error than time of arrival method.
- The three-point bending test on the honeycomb sandwich structure coupled with the acoustic emission could reveal and assess the damage mechanisms using frequency analysis and cumulative energy analysis.
- The wind turbine blade has been manufactured, and the manufacturing considerations include chamfering the honeycomb layer to eliminate the resin blockage.

7.2. Future work

- The Lamb wave physics should be implemented in CalculiX by writing the semi-analytic equations to obtain the dispersive behaviour of the propagating Lamb waves.
- The numerical modelling of Lamb wave should be consider the insertion loss effects.
- The principal component analysis should be carried out critically after AE testing with the aid of infrared monitoring camera or digital correlation imaging to correlate damage with the AE sources.
- The measured amplitude ratio with the information entropy function should be investigated altogether for damage assessment.
- Unsupervised clustering using k-means technique as example, could be proposed for clustering the damage modes.
- Optimising the Delta-T Mapping grid to obtain a time map that is able to locate AE sources in-plane (e.g. 2D) and opposite plane (e.g. 3D) of HSP.

Annex A: Acoustic Emission Terminology

The waveform is either burst (e.g. pulse) or continuous signal. A typical transient AE signal is shown in Figure A-1.

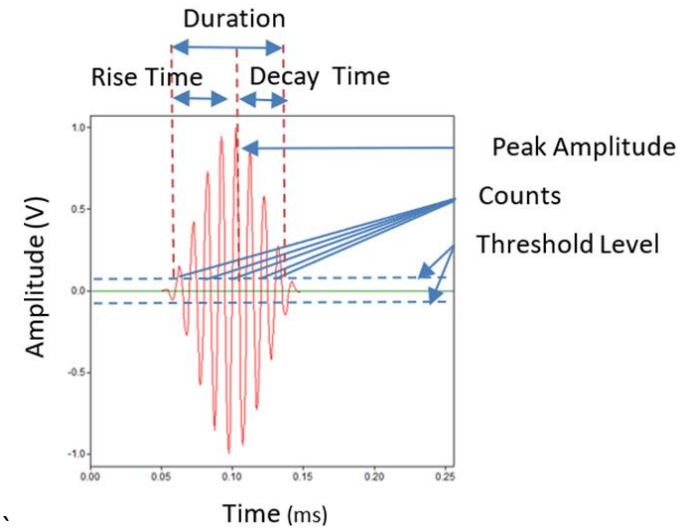

Figure A- 1. A burst AE signal feature

- **Duration:** The interval between the first and last time the threshold is exceeded by the signal.
- **Peak Amplitude:** highest signal amplitude within the duration of the signal.
- **Counts:** Signal amplitude exceeding points to the threshold.
- **Rise Time:** Interval between the first threshold crossing and the highest amplitude of signal.
- **Decay Time:** Interval between the highest amplitude of signal to the last threshold crossing.
- **Acoustic emission count (N):** the number of times the acoustic emission signal exceeds a preset threshold during any selected portion of a test.
- **Acoustic emission count rate:** the time rate at which AE counts occur.
- **Acoustic emission event:** a local material change giving rise to AE. One event would include all AE counts in a single signal envelope.

Annex B: Sensors Data Sheets

MISTRAS A World of NDT Solutions | Products & Systems Division

PHYSICAL ACOUSTICS CORPORATION

PRODUCT DATA SHEET

WD Sensor

Wideband Differential Sensor

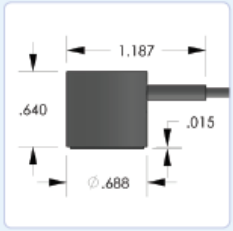

DESCRIPTION AND FEATURES

WD is a true differential wideband sensor with a very high sensitivity and bandwidth. It has a very good frequency response over the range of 100 – 900 kHz. Differential sensors differ from their general purpose counterparts by employing two sensing elements with opposite polarization directions. The two signal leads feed into a differential pre-amplifier which eliminates common-mode noise resulting in a lower noise output from the pre-amplifier. Noise improvements to the tune of 2 dB can be achieved using differential sensors over a single ended sensor. This sensor features a rugged steel construction with an integrated twin axial cable exiting on the side.

APPLICATIONS

This sensor is well suited for structural health monitoring of large structures like storage tanks, pipelines etc. This sensor is an ideal candidate for applications requiring high bandwidth for frequency analysis of the AE signals for noise discrimination and source identification. Wideband sensors are particularly well suited for research applications where a high fidelity AE response is required. It can be easily mounted using epoxy.

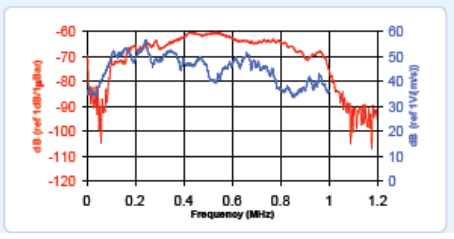

OPERATING SPECIFICATIONS

Dynamic

Peak Sensitivity, Ref V/(m/s)	56 dB
Peak Sensitivity, Ref V/µbar	-61 dB
Operating Frequency Range	125-1000 kHz
Resonant Frequency, Ref V/(m/s)	125 kHz
Resonant Frequency, Ref V/µbar	450 kHz
Directionality	+/-1.5 dB

Environmental

Temperature Range	-65 to 177ºC
Shock Limit	500 g

Completely enclosed crystal for RFI/EMI immunity

Physical

Dimensions	0.7"OD X 0.65"H 17.8 mm OD X 16.5 mm H
Weight	20 grams
Case Material	Stainless Steel
Face Material	Ceramic
Connector	BNC
Connector Locations	Side

ORDERING INFORMATION AND ACCESSORIES

WD	WD
Cable (specify length in '-XX' m at end of PN)	1 m
Magnetic Hold-Down	MHSTD
Pre-Amplifier	0/2/4, 2/4/6
Preamp to System Cable (specify length in 'm')	1234-X
Amplifier Subsystems	AE2A or AE5A

Sensors include

NIST Calibration Certificate & Warranty

MISTRAS
A World of NDT Solutions | Products & Systems Division

PHYSICAL ACOUSTICS CORPORATION

PRODUCT DATA SHEET

R6α Sensor

General Purpose, 60 kHz Resonant Frequency Sensor

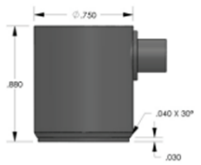

DESCRIPTION AND FEATURES

The R6α is a narrow band resonant sensor with a high sensitivity. The sensor cavity is machined from a solid stainless steel rod, making the sensor extremely rugged and reliable. The ceramic face along with a 30 degree chamfer to cavity electrically isolates the sensor cavity from the structure under test assuring a low noise operation.

The compact size of the sensor makes it readily suitable for deploying in tight spaces for monitoring. The Alpha series family of sensors features an SMA connector versus the Microdot connectors found on MISTRAS' RXX series of sensors. The alpha series includes R3α, R6α, R15α, R30α, R50α, R80α and WSα sensors.

APPLICATIONS

This sensor can be used on metal and FRP structures such as pipelines or storage tanks in petroleum, refineries, chemical plants, and offshore platforms, due to its high sensitivity and low resonance frequency properties.

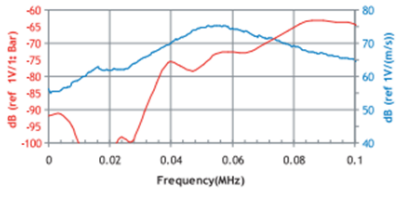

OPERATING SPECIFICATIONS

Dynamic

Peak Sensitivity, Ref V/(m/s)	75 dB
Peak Sensitivity, Ref V/µbar	-64 dB
Operating Frequency Range	35-100 kHz
Resonant Frequency, Ref V/(m/s)	55 kHz
Resonant Frequency, Ref V/µbar	90 kHz
Directionality	+/-1.5 dB

Environmental

Temperature Range	-65 to 175ºC
Shock Limit	500 g
Completely enclosed crystal for RFI/EMI immunity	

Physical

Dimensions	0.75"OD X 0.88"H 19 mm OD X 22.4 mm H
Weight	38 grams
Case Material	Stainless steel
Face Material	Ceramic
Connector	SMA
Connector Locations	Side
Seal	Epoxy

ORDERING INFORMATION AND ACCESSORIES

R6α	R6α or R6a
Magnetic Hold-Down	MHR15A
Sensor to Preamp Cable (1 or 2 meters)	1232-X-SMA
Amplifier subsystems	AE2A, AE5A or standard AE systems
Preamplifier	0/2/4, 2/4/6
Preamp to System Cable (specify length in 'm')	1234 - X

Sensors include

NIST Calibration Certificate & Warranty

AE–Sensor Data Sheet

VS900-M

The VS900-M is a passive piezoelectric AE-sensor that has a broad frequency response. Its response is characterized by two peaks at
190 kHz and 350 kHz with accompanying anti-resonances at 200 kHz and 400 kHz. Benefits of the VS900-M are a high sensitivity over a broad frequency range with compromises regarding the flatness of response. It combines a good response in the standard frequency - and high frequency range.

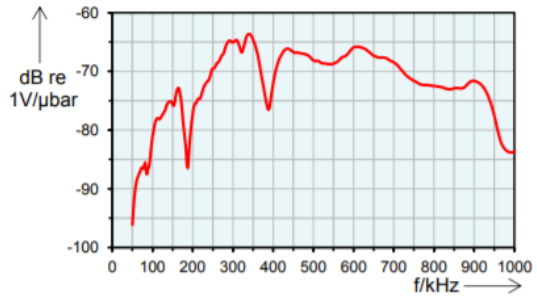

Technical Specification			
Frequency Range (f_{Peak}) [kHz]	100 to 900 (350)	**Size (D x H) [mm]**	20.3 x 14.3
Capacity [pF]	540	**Weight [g]**	22
Integrated Preamplifier	No	**Case Material**	Stainless Steel (1.4571/ 1.4404)
Operating Temperature [°C]	-50 to +100	**Wear Plate**	Ceramics
Vibration – Sinus sweep	2 Oct/Min, 5 to 180 Hz, 40 g	**Connector**	Microdot
Ingress Protection Rating	IP40	**Shield Cross-Talk [dB]**	< -80

Standards and Directives	
EMC Directive	2014/30/EU
EMC Standards	EN61326-1:2013, EN61326-2-3:2013, EN61000-6-2:2006, EN61000-6-4:2011
Shock and Vibration Stand.	EN60068-2-6:2008
AE Standard	EN13477-1:2013, EN13477-2:2013

Accessories			
Preamplifier	AEP5, AEP3N	**Sensor Cable**	CBL-1-1M2-V5
Mounting Holder	MAG4M		

References

[1] G. Clarke, D. Wowk, and C. Marsden, “Characterization of Low Velocity Impact Damage in Metallic Honeycomb Sandwich Aircraft Panels using Finite Element Analysis,” 2017.

[2] Yong Tao, Weiguo Li, Kai Wei, Shenyu Duan, Weibin Wen, Liming Chen, Yongmao Pei, Daining Fang, “Mechanical Properties And Energy Absorption Of 3D Printed Square Hierarchical Honeycombs Under In-Plane Axial Compression”, Journal of Composites. Part B Engineering, p. 107219, 2019.

[3] L. J. Gibson and M. F. Ashby, Cellular Solids: Structure And Properties. Cambridge university press, 1999.

[4] M. F. Ashby and D. R. H. Jones, Engineering Materials 1: An Introduction To Properties, Applications And Design, vol. 1. Elsevier, 2012.

[5] H. Wang, S. Li, Z. Liu, Z. Wang, and Z. Li, “Investigation On The Dynamic Response Of Circular Sandwich Panels With the Bio-Inspired Gradient Core” , Journal of Thin-Walled Structures, vol. 149, p. 106667, 2020.

[6] N. Z. M. Zaid, M. R. M. Rejab, and N. A. N. Mohamed, “Sandwich Structure Based on Corrugated-Core: A Review,” in MATEC Web of Conferences, 2016, vol. 74, p. 29.

[7] G. Sun, E. Wang, J. Zhang, S. Li, Y. Zhang, and Q. Li, “Experimental Study On The Dynamic Responses Of Foam Sandwich Panels With Different Facesheets And Core Gradients Subjected to Blast Impulse” , International Journal Impact Engineering., vol. 135, p. 103327, 2020.

[8] X. Zhang and D. Yang, “Mechanical Properties Of Auxetic Cellular Material Consisting of Re-Entrant Hexagonal Honeycombs,” Journal of Materials (Basel)., vol. 9, no. 11, p. 900, 2016.

[9] G. Sun, X. Huo, D. Chen, and Q. Li, “Experimental and Numerical Study on Honeycomb Sandwich Panels Under Bending and In-Panel Compression”, Journal of Material and Design, vol. 133, p. 154–168, 2017.

[10] M. Sadighi, A. A. Dehkordi, and R. Khodambashi, “A Theoretical and Experimental Study of Failure Maps of Sandwich Beams with Composite Skins and Honeycomb Core,” AUT Journal of Modelling and Simulation, vol. 42, no. 1, p. 37–47, 2010.

[11] A. C. Marshall, “Sandwich Construction,” in Handbook of Composites, S. T. Peters, Ed. Boston, MA: Springer US, 1998, p. 254–290.

[12] J. Hao, X. Wu, G. Oporto, W. Liu, and J. Wang, “Structural Analysis And Strength-To-Weight Optimization of Wood-Based Sandwich Composite With Honeycomb Core Under Three-Point Flexural Test,” European Journal of Wood Products., p. 1–13, 2020.

[13] H. A. Khan, F. H. Vance, A. Israr, and T. U. Rehman, “An Integrated Approach for Optimization of Honeycomb Sandwich Structure under Impact Load,” Journal of Applied Mechanics and Materials, vol. 152, p. 1717–1722, 2012.

[14] L. Santos, A. N. Nordas, B. A. Izzuddin, and L. Macorini, “Structural Design Optimisation of Rectangular Honeycomb Core Sandwich Panels Under Out-Of-Plane Loading”, 12th International Conference on Sandwich Structures, ICSS-12: Proceedings, p. 165–167, 2018.

[15] S. A. Galehdari, M. Kadkhodayan, and S. Hadidi-Moud, “Analytical, experimental and numerical study of a graded honeycomb structure under in-plane impact load with low velocity,” International Journal of crashworthiness, vol. 20, no. 4, p. 387–400, 2015.

[16] Z. Nazarchuk, V. Skalskyi, and O. Serhiyenko, Acoustic Emission: Methodology and Application. Springer, 2017.

[17] C. U. Grosse and M. Ohtsu, Acoustic Emission Testing. Springer Science & Business Media, 2008.

[18] ASTM, “976," Standard Guide for Determining the Reproducibility of Acoustic Emission Sensor Response,” ASTM B. Standard, p. 3, 1993.

[19] B. J. Wright, S. Grigg, A. S. Bergsaker, J. E. Brattgjerd, H. Steen, and R. Pullin, “Real Time Monitoring of Screw Insertion Using Acoustic Emission Can Predict Screw Stripping In Human Cancellous Bone” , Clin Biomech (Bristol, Avon), vol. 76, p. 105026, 2020.

[20] P. Blaikie, “A Smart Surgical Tool For Optimal Dental Implant Fixation”, 96th General Session of the IADR, London, UK, 2018.

[21] S. Das, P. Saha, and S. K. Patro, “Vibration-Based Damage Detection Techniques Used For Health Monitoring of Structures: A Review”, Journal of Civil Structure Health Monitoring, vol. 6, no. 3, p. 477–507, 2016.

[22] F. Bai, D. Gagar, P. Foote, and Y. Zhao, “Comparison Of Alternatives To Amplitude Thresholding For Onset Detection of Acoustic Emission Signals”, Journal of Mechanical System and Signal Processing, vol. 84, p. 717–730, 2017.

[23] H. Akaike, “Information theory and an extension of the maximum likelihood principle,” in Selected papers of hirotugu akaike, Springer, p. 199–213, 1998.

[24] R. Madarshahian, P. Ziehl, and M. D. Todd, “Bayesian Estimation of Acoustic Emission Arrival Times for Source Localization,” in Model Validation and Uncertainty Quantification, Volume 3, Springer, p. 127–133 , 2020.

[25] M. Liu, J. Yang, Y. Cao, W. Fu, and Y. Cao, “A New Method For Arrival Time Determination of Impact Signal Based on HHT And AIC,” Journal of Mechanical System and Signal Processing, vol. 86, p. 177–187, 2017.

[26] Z. Zhou, R. Cheng, Y. Rui, J. Zhou, and H. Wang, “An Improved Automatic Picking Method for Arrival Time of Acoustic Emission Signals,” IEEE Access, vol. 7, p. 75568–75576, 2019.

[27] R. Unnþórsson, “Hit Detection And Determination In AE Bursts”, Journal of Acoustic Emissission, p. 1–20, 2013.

[28] C. Wang, Y. Zhang, and A. Ma, “Investigation Into The Fatigue Damage Process of Rubberized Concrete and Plain Concrete By AE Analysis”, Journal of Materials and Civil Engineering, vol. 23, no. 7, p. 953–960, 2011.

[29] R. Svečko, D. Kusić, T. Kek, A. Sarjaš, A. Hančič, and J. Grum, “Acoustic emission detection of macro-cracks on engraving tool steel inserts during the injection molding cycle using PZT sensors,” Sensors, vol. 13, no. 5, pp. 6365–6379, 2013.

[30] M. Eaton, “Acoustic Emission (AE) Monitoring of Buckling and Failure In Carbon Fibre Composite Structures”, Cardiff University (United Kingdom), 2007.

[31] P. Aryan, A. Kotousov, C. T. Ng, and B. S. Cazzolato, “Lamb Wave Characterisation And Damage Imaging For Isotropic Plate-Like Structures Using 3D Laser Vibrometry,”, Recent Advances in Structural Integrity Analysis - Proceedings of the International Congress (APCF/SIF-2014) 2014.

[32] H. Lamb, “On waves in an Elastic Plate,” Proceeding of Royal Society. A, vol. 93, no. 648, pp. 114–128, 1917.

[33] N. Hsu, J. A. Simmons, and S. C. Hardy, “Approach to acoustic Emission Signal Analysis-Theory and Experiment”, Proceedings of The ARPA/AFML Review of Progress In Quantitative NDE, September 1976–June 1977.

[34] L. Friedrich, A. Colpo, A. Maggi, T. Becker, G. Lacidogna, and I. Iturrioz, “Damage Process In Glass Fiber Reinforced Polymer Specimens Using Acoustic Emission Technique With Low Frequency Acquisition”, Journal of Composite Structures, vol. 256, p. 113105, 2021.

[35] Z. M. Hafizi, J. Epaarachchi, and K. T. Lau, “An Investigation Of Acoustic Emission Signal Attenuation For Monitoring of Progressive Failure In Fiberglass Reinforced Composite Laminates,” International Journal of Automotive and Mechanical Engineering, vol. 8, no. 1, p. 1442–1456, 2013.

[36] Y. Wu, M. Perrin, M.-L. Pastor, P. Casari, and X. Gong, “On The Determination of Acoustic Emission Wave Propagation Velocity In Composite Sandwich Structures”, Journal of Composite Structures, p. 113231, 2020.

[37] S. Sikdar, P. Mirgal, S. Banerjee, and W. Ostachowicz, “Damage-Induced Acoustic Emission Source Monitoring In a Honeycomb Sandwich Composite Structure”, Journal of Composites: Part B Engineering, vol. 158, p. 179–188, 2019.

[38] H. Baid, C. Schaal, H. Samajder, and A. Mal, “Dispersion Of Lamb Waves in a Honeycomb Composite Sandwich Panel”, Journal of Ultrasonics, vol. 56, p. 409–416, 2015.

[39] N. Guo and M. K. Lim, “Lamb Waves Propagation In Aluminum Honeycomb Structures”, Review of Progress in Quantitative Nondestructive Evaluation, Springer, p. 323–330, 1996.

[40] K. M. Holford, Safaa Eljumaili, Rhys Pullin, Matthew Pearson., “A New Methodology For Automating Acoustic Emission Detection of Metallic Fatigue Fractures In Highly Demanding Aerospace Environments: An Overview”, Journal of Progress in Aerospace Science, vol. 90, p. 1–11, 2017.

[41] S. Al-Jumaili, M. Pearson, K. Holford, M. Eaton, and R. Pullin, “Fast and Reliable Acoustic Emission Source Location Technique in Complex Structures” , Journal of Mechanical Systems and Signal Processing, 2016.

[42] R. K. Miller and P. McIntire, “Nondestructive Testing Handbook vol. 5,” P. mcIntire Ed. ASNT, 1987.

[43] V. Arumugam, B. Kumar, C. Santulli, and A. J. Stanley, “Effect of Fiber Orientation in Unidirectional Glass Epoxy Laminate Using Acoustic Emission Monitoring” , Journal of Acta Metallica, vol. 24, no. 5, p. 351–364, 2011.

[44] C. A. Middleton, J. P. McCrory, R. J. Greene, K. Holford, and E. A. Patterson, “Detecting and Monitoring Cracks in Aerospace Materials Using Post-Processing of TSA and AE Data”, Journal of Metals (Basel)., vol. 9, no. 7, p. 748, 2019.

[45] M. G. Baxter, R. Pullin, K. M. Holford, and S. L. Evans, “Delta T source location for acoustic emission”, Journal of Mechanical Systems and Signal Processing, vol. 21, no. 3, pp. 1512–1520, 2007.

[46] R. Pullin, M. Baxter, M. Eaton, K. M. Holford, and S. L. Evans, “Novel Acoustic Emission Source Location”, Journal of Acoustic Emission, vol. 25, p. 215–223, 2007.

[47] S. K. Al-Jumaili, M. R. Pearson, K. M. Holford, M. J. Eaton, and R. Pullin, “Acoustic Emission Source Location In Complex Structures Using Full Automatic Delta T Mapping Technique,” Journal of Mechanical Systems and Signal Processing, vol. 72, pp. 513–524, 2016.

[48] F. A. Leone Jr, D. Ozevin, J. Awerbuch, and T.-M. Tan, “Detecting and Locating Damage Initiation And Progression in Full-Scale Sandwich Composite Fuselage Panels Using Acoustic Emission,” Journal of Composite Materials, vol. 47, no. 13, pp. 1643–1664, 2013.

[49] Society for Non-Destructive and Inspection, Practical Acoustic Emission Testing. Japan: Springer, 2016.

[50] E. K. Miller, K R; Hill, Non-Destructive Testing Handbook. American Society for Non-Destructive Testing, 2005.

[51] W. Harizi, J. Anjoul, V. Santamaría, Z. Aboura, and V. Briand, “Mechanical Behavior Of Carbon-Reinforced Thermoplastic Sandwich Composites With Several Core Types During Three-Point Bending Tests”, Journal of Composite Structures, p. 113590, 2021.

[52] F. Pashmforoush, M. Fotouhi, and M. Ahmadi, “Damage characterization of glass/epoxy composite under three-point bending test using acoustic emission technique,” Journal of Materials Engineering and Performance, vol. 21, no. 7, pp. 1380–1390, 2012.

[53] M. Panek, S. Blazewicz, and K. J. Konsztowicz, “Correlation of Acoustic Emission with Fractography in Bending of Glass–Epoxy Composites,” Journal of Nondestructive Evaluation, vol. 39, no. 3, pp. 1–10, 2020.

[54] N. Beheshtizadeh, A. Mostafapour, and S. Davoodi, “Three Point Bending Test of Glass/Epoxy Composite Health Monitoring By Acoustic Emission,” Alexandria Engineering Journal, vol. 58, no. 2, pp. 567–578, 2019.

[55] C. S. Kumar, V. Arumugam, S. Sajith, H. N. Dhakal, and R. John, “Acoustic Emission Characterisation of Failure Modes In Hemp/Epoxy and Glass/Epoxy Composite Laminates,” Journal of Nondestructive Evaluation, vol. 34, no. 4, p. 1–11, 2015.

[56] M. Pearson, “Development of Lightweight Structural Health Monitoring Systems For Aerospace Applications.”, PhD Thesis Cardiff University, 2013.

[57] S. K. Gopalraj and T. Kärki, “A Review on the Recycling of Waste Carbon Fibre/Glass Fibre-Reinforced Composites: Fibre Recovery, Properties and Life-Cycle Analysis,” Journal of Applied Sciences, vol. 2, no. 3, pp. 1–21, 2020.

[58] A. Raju and M. Shanmugaraja, “Recent Researches In Fiber Reinforced Composite Materials: A Review”, Journal of Materials Today, 2020.

[59] M. A. Shomad and F. R. Hidayat, “Vertical Blade Fiberglass Composite for Wind Turbine Power Plant Application,” Journal of Robotic Control, vol. 2, no. 3, pp. 148–152, 2021.

[60] C. Morăraş, B. Leitoiu, I. Blanari, and L. Andrusca, “Compression Behaviour Study For Glass Fiberglass-Reinforced Plastics Used In The Construction of Wind Turbine Blades”, IOP Conference Series: Materials Science and Engineering, 2020, vol. 997, no. 1, p. 12099.

[61] M. A. Ghafaar, A. A. Mazen, and N. A. El-Mahallawy, “Application of The Rule of Mixtures And Halpin-Tsai Equations To Woven Fabric Reinforced Epoxy Composites,” Journal of Engineering Sciences, Assiut University, vol. 34, no. 1, p. 227–236, 2006.

[62] R. M. Jones, Mechanics Of Composite Materials. CRC Press, 2018.

[63] J. J. Scholey, P. D. Wilcox, C. K. Lee, M. I. Friswell, and M. R. Wisnom, “Acoustic emission in wide composite specimens”, Journal of Advanced Materials Research, 2006, vol. 13, pp. 325–332.

[64] T. N. Bitzer, Honeycomb Technology: Materials, Design, Manufacturing, Applications and Testing. Springer Science & Business Media, 1997.

[65] S. Timoshenko and S. Woinowsky-Krieger, “Theory of plates and shells”, Mcgrew-Hill 1959.

[66] A. Messac, Optimization in Practice With MATLAB®: For Engineering Students and Professionals. Cambridge University Press, 2015.

[67] S. D. Zubowicz, “The Application of Finite Element Method In Engineering Calculations Using Opensource Software”, Instytut Metrologii i Inżynierii Biomedycznej, 2017.

[68] G. Dhondt, “CalculiX CrunchiX User’s Manual Version 2.12,” Munich, accessed Sept, vol. 21, 2017.

[69] S. K. Nammi, H. Shirvani, A. Shirvani, and J. Mauricette, “Verification of finite element analysis code CalculiX CrunchiX (ccx) in accordance with ISO 10211: 2007,” 2014.

[70] A. International, “Standard Test Method For Core Shear Properties of Sandwich Constructions By Beam Flexure. ASTM C393/C393M-06”, ASTM International West Conshohocken, Pennsylvania, 2006.

[71] A. Kumar and R. S. Sharma, “Modal Analysis And Testing Of Honeycomb Sandwich Composites” in Topics in Modal Analysis, Volume 10, Springer, p. 237–241, 2015.

[72] F. Song, G. L. Huang, and K. Hudson, “Guided Wave Propagation In Honeycomb Sandwich Structures Using A Piezoelectric Actuator/Sensor System”, Journal of Smart Material Structure, vol. 18, no. 12, p. 125007, 2009.

[73] U. A. Bakshi, Telecommunication engineering. Technical Publications, 2009.

[74] V. Kappatos and E. Dermatas, “Neural localization of acoustic emission sources in ship hulls,” J. Mar. Sci. Technol., vol. 14, no. 2, pp. 248–255, 2009.

[75] Z. Su and L. Ye, “Identification of Damage Using Lamb Waves”, Springer, pp. 15–58, 2009.

[76] Laboratory for Active Materials and Smart Structures (LAMSS), “LAMSS Products: LAMSS-COMPOSITES Software.” [Online]. Available: me.sc.edu/research/lamss/html/software.html.

[77] E. H. Saidane, D. Scida, M. Assarar, and R. Ayad, “Damage Mechanisms Assessment of Hybrid Flax-Glass Fibre Composites Using Acoustic Emission”, Journal of Composite Structures, vol. 174, pp. 1–11, 2017.

إهداء

أهدي هذه الرسالة لوالديّ ولعائلتي ولأستاذي الراحل الدكتور/ أحمد حسين

بدون صبر وتضحيات زوجتي سما أحمد كان لا يمكن إنجاز عملي البحثي في المملكة المتحدة

الملخص

للحصول على الأداء الديناميكي الهوائي الأمثل في توربينات الرياح ، يجب أن تتمتع هياكل ريش بوزن منخفض لنسبة صلابة الانحناء. يمكن أن تلعب المواد المركبة المصممة من لوح الألومنيوم ذي خلايا سداسية الشكل بين سطحين من الألياف الزجاجية، دورًا مهمًا في إنتاج ريش توربينات الرياح الأطول بتكلفة أقل مقارنة بألياف الكربون.

تتضمن الأطروحة دراسة حول الهياكل المصنوعة من لوح ذي خلايا سداسية الشكل من الألومنيوم داخل سطحين من الألياف الزجاجية والتي يتم تنفيذها في ريش توربينات الرياح. تبدأ الدراسة بإجراء تحسين هيكلي لتقليل الوزن إلى نسبة صلابة الانحناء عقب ذلك تمت دراسة الحركة الموجية الناتجة عن الانبعاث الصوتي على هذا الهيكل المعقد ثم اختبار العينات تحت اختبارات الانحناء وأخيراً بناء ريشة توربينات الرياح صغيرة الحجم باستخدام الهيكل الأمثل.

أجريت دراسة موجة الانبعاث الصوتي على لوح من الألياف الزجاجية ثم على عينات من الألومنيوم ذي عدد محدود من الخلايا السداسية لمعرفة تأثير الخلية الواحدة على انتشار الموجة الصوتيةمن سطح إلى سطح وأخيراً على عينة كبيرة كاملة . لقد وجد أن موجات لامب تتحرك في أسطح الألياف الزجاجية العلوية والسفلية لكن في اللوحة السفلية للعينة الكاملة، وجد أن خلايا الشكل السداسي تعمل كقنوات لانتقال الموجات الصوتية من اللوحة العلوية إلى السفليةوتكون الأشكال الموجية في اللوحة السفلية منحازة إلى وضع الانحناء الاهتزازي A_o لموجة لامب مع وضع التمديد الاهتزازي S_o متناقص للغاية.

تمت دراسة سرعات الموجة في الوضع A_o و S_o في اتجاهات من 0^o إلى 90^o بمعدل زاويّ 15 درجة. لقد وجد أن سرعة A_o لا تتغير مع الاتجاه لأنها تعتمد بشكل أساسي على الكزازة في المستوى العمودي على السطح. من ناحية أخرى، تتغير سرعات S_o مع الاتجاه فيما يتعلق بإتجاه الألياف. علاوة على ذلك، يتم تحليل منحنيات التشتت لانتشار موجات لامب عدديًا وتجريبيًا ويقترح مفهوم الفقد البيني من أجل تحديد تأثيرات الخلايا سداسية الشكل على انتشار وجات لامب.

تم إجراء دراسات موقع مصدر الانبعاث الصوتي على سطحيّ الهيكل ذي لوح خلايا الومنيوم سداسية الشكل باستخدام تقنيتين مشهورتين، طريقة وقت الوصول وطريقة الفارق الزمني. تم إنشاء مصادر الانبعاث الصوتي على كل من سطحيّ الهيكل بينما تم ربط الحساسات بأحدهما فقط.

لقد وجد أن تعيين مصدر الانبعاث الصوتي بواسطة طريقة الفرق الزمني يعطي نصف خطأ متوسط طريقة زمن الوصول. علاوة على ذلك، فإن تعيين Delta-T أكثر قدرة على تحديد موقع المصدر في المستويين الثنائي والثلاثي الأبعاد.

بعد ذلك، تم إجراء اختبارات الانحناء على عينة الهيكل المقترنة بطريقة الفارق الزمني لتقييم الضرر في العينة وموقعها. لقد وجد أن اختبار الانبعاث الصوتي ليس فقط قادرًا على تحديد موقع الضرر على العينة ولكن يمكنه أيضًا وصف آلية الضرر. تم تمييز تطور الضرر في العينة تحت الانحناء باستخدام كل من المجهر الإلكتروني الماسح ثم تم ربطه بترددات إشارة الانبعاث الصوتي والطاقة.

أخيرًا، تم استخدام الهيكل ذي خلايا ألومنيوم سداسية الشكل بين سطحي من الألياف الزجاجية في تصنيع ريش توربينات الرياح ذات المحور الرأسي من النوع NACA8412 ويتم توضيح اعتبارات التصنيع.

تعريف بمقدم الرسالة

الاسم: أحمد هشام عبد العزيز محمد

تاريخ الميلاد: 1988/5/16

محل الميلاد : القاهرة

اخر درجة جامعية : الماجيستير في العلوم الهندسية

الجهة المانحة:جامعة عين شمس

تاريخ المنح:2016/4/6

الوظيفه الحالية:مدرس مساعد-قسم التصميم وهندسة الإنتاج

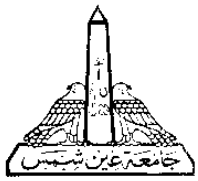

كلية الهندسة

قسم التصميم و هندسة الإنتاج

رسالة الدكتوراه:

اسم الطالب :أحمد هشام عبد العزيز محمد

عنوان الرسالة : **: دراسة استخدام المؤلفات ذات بنية سداسية الشكل لريش توربينات الرياح مع تقييم العيوب بطريقةالإنبعاثات الصوتية**

اسم الدرجة : دكتوراه الفلسفة فى الهندسة

لجنة الاشراف:

أ.د/ عادل محمد منيب الصباغ

أ.د/كارين هولفورد

د/ محمد محمد طه هداية

تاريخ البحث : ...../...../.....

الدراسات العليا:

ختم الإجازة: اجيزت الرسالة بتاريخ : ...../...../.....

موافقة مجلس الكلية : ...../...../.....

موافقة مجلس الجامعة : ...../...../.....

القاهرة-2021

الموافقة على المنح

كلية الهندسة

قسم التصميم و هندسة الإنتاج

دراسة استخدام المؤلفات ذات بنية سداسية الشكل لريش توربينات الرياح مع تقييم العيوب بطريقةالإنبعاثات الصوتية

إعداد

أحمد هشام عبد العزيز محمد البدر هاشم

لجنة الحكم

الاسم	التوقيع
أ.د/ محمد فهمي محمد شحادة عميد كلية الهندسة والتكنولوجيا-الأكاديمية البحرية-فرع الوادي الجديد	.....
أ.د/ تامر محمد عبد الفتاح النادي أستاذ بقسم التصميم وهندسة الإنتاج-كلية الهندسة-جامعة عين شمس	.....
أ.د/ عادل محمد منيب عبد العزيز الصباغ أستاذ بقسم التصميم وهندسة الإنتاج-كلية الهندسة-جامعة عين شمس	.....
أ.د/ كارين هولفورد أستاذ الهندسة الميكانيكية - نائب رئيس جامعة كارديف- بريطانيا	.....

التاريخ...../...../.....

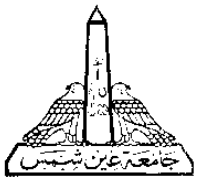

كلية الهندسة

قسم التصميم و هندسة الإنتاج

دراسة استخدام المؤلفات ذات بنية سداسية الشكل لريش توربينات الرياح مع تقييم العيوب بطريقةالإنبعاثات الصوتية

رسالة مقدمة للحصول على درجة دكتوراه الفلسفة

فى الهندسة الميكانيكية

(التصميم و هندسة الإنتاج)

اعداد

أحمد هشام عبد العزيز محمد البدر هاشم

حاصل على ماجستير العلوم

فى الهندسة الميكانيكية

(التصميم و هندسة الإنتاج)

كلية الهندسة، جامعة عين شمس , 2016

المشرفون

أ.د/ عادل محمد منيب الصباغ

أ.د/كارين هولفورد

د/محمد محمد طه هداية